3-14-2014

Integration, Testing, And Analysis Of Multispectral Imager On Small Unmanned Aerial System For Skin Detection

Stephen R. Sweetnich

Follow this and additional works at: https://scholar.afit.edu/etd

INTEGRATION, TESTING, AND ANALYSIS OF MULTISPECTRAL IMAGER ON SMALL UNMANNED AERIAL SYSTEM FOR SKIN DETECTION

THESIS

Stephen R. Sweetnich

AFIT-ENV-14-M-60

DEPARTMENT OF THE AIR FORCE
AIR UNIVERSITY

AIR FORCE INSTITUTE OF TECHNOLOGY

Wright-Patterson Air Force Base, Ohio

AFIT-ENV-14-M-70

INTEGRATION, TESTING, AND ANALYSIS OF SMALL UNMANNED AERIAL SYSTEMS FOR SKIN DETECTION

THESIS

Presented to the Faculty

Department of Systems and Engineering Management

Graduate School of Engineering and Management

Air Force Institute of Technology

Air University

Air Education and Training Command

In Partial Fulfillment of the Requirements for the

Degree of Master of Science in Systems Engineering

Stephen R. Sweetnich, BS

Civilian

March 2014

AFIT-ENV-14-M-70

**INTEGRATION, TESTING, AND ANALYSIS OF SMALL UNMANNED AERIAL
SYSTEMS FOR SKIN DETECTION**

Stephen Sweetnich, BS

Civilian

Approved:

<u>//signed//</u>	<u>March 2014</u>
David R. Jacques, PhD (Chairman)	Date
<u>//signed//</u>	<u>March 2014</u>
Jeffrey D. Clark, Lt Col, PhD USAF (Member)	Date
<u>//signed//</u>	<u>March 2014</u>
Michael E. Miller, PhD (Member)	Date

AFIT-ENV-14-M-70

Abstract

Small Unmanned Aerial Systems (SUAS) have been utilized by the military, geological researchers, and first responders, to provide information about the environment in real time. Hyperspectral Imagery (HSI) provides high resolution data in the spatial and spectral dimension; all objects, including skin have unique spectral signatures. However, little research has been done to integrate HSI into SUAS due to their cost and form factor. Multispectral Imagery (MSI) has proven capable of dismount detection with several distinct wavelengths. This research proposes a spectral imaging system that can detect dismounts on SUAS. Also, factors that pertain to accurate dismount detection with an SUAS are explored. Dismount skin detection from an aerial platform also has an inherent difficulty compared to ground-based platforms. Computer vision registration, stereo camera calibration, and geolocation from autopilot telemetry are utilized to design a dismount detection platform with the Systems Engineering methodology. An average 5.112% difference in ROC AUC values that compared a line scan spectral imager to the prototype area scan imager was recorded. Results indicated that an SUAS-based Spectral Imagers are capable tools in dismount detection protocols. Deficiencies associated with the test expedient prototype are discussed and recommendations for further improvements are provided.

Acknowledgments

      This research was only possible with the great support received from the faculty, staff, and students at AFIT. Lt Col Jeffrey Clark, has given me the opportunity work with the Sensor Exploration Research Group, and provided the guidance to make this research a reality. Dr. David Jacques, provided his expertise, equipment, and support to complete this thesis, and continues to expand the SUAS domain. Rick Patton, who served as my safety pilot and technical advisor, and my colleague Shane Fernandes were key assets throughout. The AFIT ANT center and AFRL was instrumental in providing tools, equipment and space for testing. Also, I have immense gratitude for my classmates, who continually offered their tacit knowledge. However, I dedicate this work to my parents, for their immeasurable support.

Stephen R. Sweetnich

Table of Contents

List of Figures

x

List of Tables

INTEGRATION, TESTING, AND ANALYSIS OF SMALL UNMANNED AERIAL SYSTEMS FOR SKIN DETECTION

1. Introduction

1.1 General Issue

Integrating Multispectral Imaging (MSI) on a Small Unmanned Aerial System (SUAS) may present a valuable tool for dismount detection. SUAS offer versatile platforms for Military, police, or Search and Rescue (SAR) operators. The U.S. Geological Survey, the U.S. Air Force, and others have demonstrated the utility of SUAS in natural disasters such as the Fukushima Daiichi meltdown to take photographs at altitudes that were hazardous to human pilots (U.S. Geological Survey, 2011). SUAS can extend our capacity to perform missions in dangerous environments with limited personnel due to their autonomous operating capability (Aeryon Labs Inc., 2013). Sensors such as MSI and Hyperspectral Imaging (HSI) can expand the capabilities of SUAS. Currently, skin detection is achieved with large and resource intensive sensor assets. HSI can remotely identify materials, including skin but it has proven difficult to utilize the data quickly and efficiently. Situational awareness of the mission area may be improved by identification of material and dismounts. SUAS are quickly deployable, versatile sensor platforms, which can provide invaluable information in many domains. Designing a sensor system to detect skin onboard a SUAS is the main focus of this research.

1.2 Background

Data from aerial platforms demonstrated significant utility in countless reconnaissance, surveying, and search and rescue operations. Recently, unmanned aerial

1

systems (UAS) have proven their worth in these domains by providing precise and timely information. Currently, sensor data are compiled on the Ground Control Station (GCS) or the headquarters from imagery provided over satellite or radio communications. When sensor data are processed, they usually involve humans making decisions based on imagery. For SUAS, the use of multiple sensors may enhance the utility of the images, but may result in integration complexity and/or high operator workload as the operator views data for each sensor. MSI collects many signatures throughout the electromagnetic spectrum; it provides the opportunity to conduct efficient Intelligence Surveillance and Reconnaissance (ISR), or SAR (Beisley, 2012). However, the additional sensor dimensionality increases the need for filters, and processing time from computers and humans. There are limitations with the current approach for sensor fusion due to available communications bandwidth, computational power, and human responsiveness. By using more sensors than necessary to interpret a target, excessive bandwidth is taken. Furthermore, computational power for processing large data sets may not be possible on small GCS units. Finally, the ability of a human to make decisions is impaired by cluttered imagery (Donahue, 1991).

The metrics used to measure the performance of the skin detection systems are explored, and are used to compare a ground based HSI, with the proposed aerial skin detection system. Time and cost are key resources in systems applications; the overarching goal of the SUAS skin detection system is to obtain accurate dismount detection, and minimize system cost. Incorporating a systems approach to sensor fusion may lower costs for operations, decrease the time needed to process data on the ground, and decrease the time of decision making for operators in the field (Muller & Narayanan,

2009). This research aims to measure system performance and effectiveness of a SUAS skin detection system for dismount detection.

1.3 Problem Statement

Natural and manmade disasters jeopardize the safety of local inhabitants, and sometimes cause people to go missing or astray; first responders are tasked with finding those in danger. SUAS are mobile platforms that have proven effective in many domains, and can combine multiple sensors in a small, cost effective, and readily deployable platform. Unique spectral signatures exist for all materials and they provide another method to distinguish between objects. HSI and MSI sensors add a new dimension to images by increasing the number of wavelengths collected in a scene. However, current MSI and HSI platforms have been too large and costly to deploy. If detection of a dismount or their skin can be accomplished with a cost effective system employing MSI sensors on a SUAS, this system may allow an efficient means for locating rescue personnel, survivors, or threats. However, an SUAS presents many challenges to imagery that can make dismount detection difficult. A multispectral system on an SUAS platform requires a systematic design to consider any factors that may impact dismount detection.

1.4 Research Objectives and Questions

The utility of the MSI system for dismount detection onboard a SUAS is the main focus of this research. To measure the utility of a system, subjective and objective metrics will be used. By using standardized metrics, the detection system can be compared against a wide range of detection systems. Camera vibration, registration accuracy, and

detection accuracy all objectively measure system performance. In terms of systems engineering, metrics serve as Measures of Performance (MOP). Nevertheless, the use of these metrics cannot encapsulate every aspect of the system effectiveness. A Measure of Effectiveness (MOE) evaluates the system for the overall mission goal.

Metrics will be determined that accurately reflect the utility of imagery data. Image Quality (IQ) is largely subjective, but aspects of it can be measured objectively with metrics identified in the literature (Gundlach, 2012). Subjective scales such as the NIIRS and Johnson criteria can be measured with mathematical relationships to compare different multispectral sensor arrangements. A research objective is to determine if these metrics sufficiently characterize dismount detection. Finally, the overall research goal is to determine the feasibility of skin detection on an SUAS platform, this objective requires assessment of all camera, airframe, and communications subsystems. The investigative questions of this research are listed:

1. Is MSI effective for dismount detection on an SUAS?
2. What type of MSI system is needed for an aerial platform?
3. Which camera parameters are most critical for aerial dismount detection?
4. What metrics are best to compare dismount detection ability?

1.5 Research Focus

This thesis demonstrates the ability to detect skin on an SUAS through the design, construction, and evaluation of a MSI skin detection platform. The research utilized known detection algorithms, Commercial of the Shelf (COTS) and Government off the Shelf (GOTS) equipment, and aerial flight testing of the algorithms and equipment. To

measure image detection effectiveness of the proposed system, objective measurements

of camera pixel values for IQ and fusion are compared against the more costly SpecTIR

HSI and Monocular skin detection systems.   A Receiver Operating curve (ROC) was

utilized as one metric to characterize the quality of the detection system, and it can judge

the effectiveness of the system in detecting skin for automated dismount detection

(Beisley, 2012). Other objective image processing metrics were used for system

comparison, including the General Image Quality Equation (GIQE), and the Cumulative

Probability of Blur Detection (CPBD) (Narvekar & Karam, 2011; Thurman & Fienup,

2010). These objective metrics can prove useful for measuring the sensor platform utility

when compared with subjective quality metrics. Each of these metrics measures different

qualities and reacts to unique imagery fusion methods. For example, one metric may be

affected most by image focus, while another may measure edge continuity. In this

research, the goal is to determine imagery platform utility with quantifiable metrics and

to propose a system that meets system requirements.

1.6 Assumptions/Limitations

- The system for skin detection was limited to the sensors available at AFIT, including the MSI imager, VIS imager, and bandpass filters.

- The SUAS used for the skin detection was limited to the airframes available at the AFIT Advanced Navigational Technology (ANT) Center.

- For the time available for flight test, a specific loiter pattern was utilized, which was optimized to the camera parameters (i.e. resolution, focal length)

- Due to the cost and size of a digital video acquisition and transmission system, onboard storage of imagery was performed in flight test.

- Weather conditions (sunlight, rain, wind …) were unalterable and affected flight duration, autopilot waypoint tracking, and sensor parameters.

- The research assumed that each dismount had skin which was visible from the air.

- A flat earth model was used for processing flight data.

Sensors available for ISR and SAR constantly evolve and require reevaluation of system parameters such as slant range, airspeed, and focal arrangement. Some scenarios may require sensor systems to operate at extreme altitudes, temperatures, or winds. Sensor system requirements are coupled with airworthiness requirements. These requirements may govern placement of sensors and equipment onboard the airframe. Airworthiness is characterized by many factors, including proper center of gravity (CG) placement, acceptable modifications to the airframe, adequate power availability, and suitable mission flight time. Size and weight of the sensor payload, batteries, powertrain, autopilot, servos, and electronics impact equipment placement and CG. Weight placed outside the CG generates a moment and can cause stability issues for the airframe (FAA, 2007). Due to payload capacity requirements, and vibration requirements, an electric version of the Sig Rascal 110 was selected for the skin detection system design.

Due to cost, schedule, and availability, certain sensors were utilized despite unfavorable specifications such as size and weight. For example, a filter wheel was chosen that added considerable weight to the sensor package, so a lightweight housing was constructed to lighten the sensor payload. Range availability limited the choice of weather conditions, and this was a corollary of schedule conflict. The airframe, microcontrollers, telemetry, and communications equipment were configured to meet the research objectives and so extraneous variables were eliminated where appropriate. For

example, a frame-grabber and processor to perform band math onboard was outside the price range and a flight ready configuration of this equipment would prohibit flight test. The wireless data links available for video lacked the bandwidth to transmit data at an acceptable rate, and they were used primarily for location estimation. On-board data loggers were used to capture flight video and telemetry to minimize transmission errors. A flat earth Six Degree of Freedom (6DOF) model was used to process flight telemetry, and this is accurate for the range capabilities of SUAS. Despite limitations, the data were suitable for a posteriori modeling of the mission environment.

1.7 Materials and Equipment

Multiple components were utilized for the SUAS, including an airframe, communications, video, and GCS subsystems. Each of these components was selected to meet the requirements specified in the literature, and experimentation. The major airframe components were COTS hardware that included an electric modified Sig Rascal 110, a programmable autopilot, and sufficient batteries for test flights. The communications components included 900 MHz wireless telemetry modems, and 5.8 GHz wireless video transmitters. The video subsystem components included a filter wheel, bandpass filters, a programmable stepper motor driver and microcontroller, along with separate batteries to power the sensor components. The GCS included video and telemetry receivers, mission planning software, MATLAB and ENVI for image processing software, and frame grabbing hardware. The entire system was flight tested at Camp Atterbury, IN with U.S. Army, U.S. Air Force, and Co-Operative Engineering Services Inc (CESI).

1.8 Preview

Chapter II explores the background literature for skin detection, SUAS, methods for vision processing, and metrics for imagery analysis. Chapter III presents a methodology for data collection and refers to the fusion techniques described in the literature review. Chapter IV presents the results and discussion of metrics that were applied to experimental data; a comparison of objective and subjective metrics is presented. Chapter V presents a summary of findings, critical analysis of metrics, and suggestion for future research.

2. Literature Review

2.1 Chapter Overview

This literature review explores background information needed for target detection with multiple sensors. First, a background of UAS operation is presented, to explain the nuances associated with aerial imagery. Second, spectral and spatial image processing methods and techniques are discussed. Third, metrics that can be applied to judge the quality of dismount detection data are explained.

2.2 Data Fusion

An apparatus that can autonomously survey, make judgment of elements in a scene, and command the best course of action can have tremendous impacts; data fusion can be effective for these tasks. Steinberg and Bowman (2010), explore data fusion and a model used by the DoD to depict fusion. The Joint Directorate of Laboratories (JDL) established a model that is organized into five levels of fusion. A SAR SUAS may serve as the basis for all levels of fusion. Level 0 is the lowest level of fusion, and it includes preconditioning of data. On the SAR system, Level 0 fusion may involve radiometric calibration to convert pixel values to reflectance values. Level 1 is object refinement; it may involve fusing feature detectors to classify objects for Automatic Target Recognition (ATR). Fusing aircraft attitude measurements, GPS locations, and visual ground features to geolocate an image on an SUAS is also considered Level 1 fusion. Level 2 fusion is Situation Refinement. This fusion may involve relating objects or events to situations; for example, knowing where a group is located, the status of their health, and their level of movement may indicate their situation. Level 3 is Impact refinement, which matches all

courses of action with their possible impact or cost. Level 3 would combine knowledge of dismount location and weather readings with the impact of launching a rescue mission. Finally, Level 4 is process performance refinement and it measures efficiency of the operational configuration and estimation of MOPs and MOEs; this level is often conducted in the system design and evaluation stage to determine a system's goals. In the SUAS system, system designers may realize the potential issues of size, time, and cost by modeling and measuring a system in an operational setting. For an SUAS Detection system to be useful, it requires all elements of data fusion. Since this research involves finding the overall effectiveness of an SUAS for dismount detection, obtaining the fourth level of data fusion was the goal. The JDL model is depicted in Figure 1. (Steinberg and Bowman, 2010)
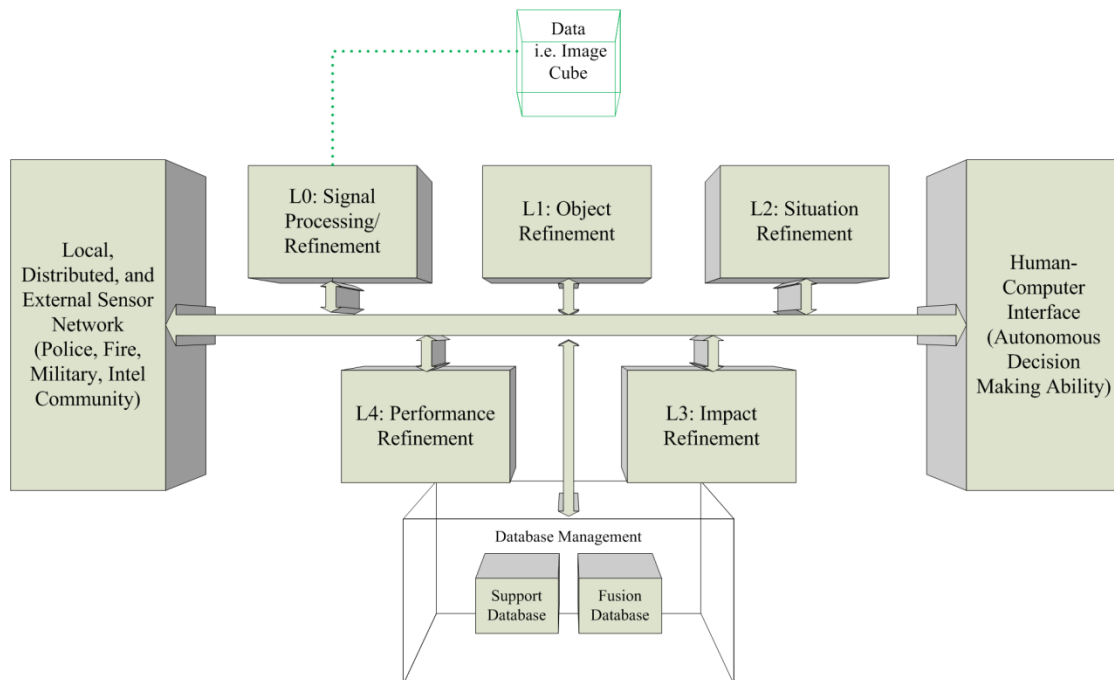
Figure 1: The Joint Directorate of Laboratories (JDL) model for data fusion

2.3 Human System Integration

　　Muller and Narayanan (2009) conducted research of human subjects' responses to fused images. This research focused on subjective data from operators on fused imagery and collected quantitative data for time to identify a target, accuracy of target identification, and confidence in target identification. The study's limitation was the use of still imagery, and inability to adjust target and background display thresholds. Nevertheless, the data suggested that further research was needed due to the disparities in subjective detection confidence and objective decision making accuracy.

　　Object identification with multiple sensors is leading to important research. Subjective metrics and objective metrics are used to fuse information from multiple sources, and these can impact the mission integrity (Liggins, Hall, & Llinas, 2008). There has been an effort to detect and identify objects with high accuracy due to increasing use of adaptive autonomy and unmanned aerial systems (UAS) (Gundlach, 2012). The ability to fuse sensor data, and accurately classify objects in real time is crucial for the operation of ISR. Integration of ATR algorithms with human decision making has been researched. This impact on judgment is directly related to the subjective performance measure proposed by Xydeas & Petrovic (Xydeas & Petrovic, 2000). Subjective quality is used by highly trained imagery analysts on some of the world's best remote sensing equipment, despite automatic feature processing. Yoshida (2006) defines subjective IQ as the level of information transmission and satisfaction with an image for a specific purpose. For an aerial detection system, mission and system effectiveness can be measured by a combination of quality metrics.

11

Image Quality (IQ) can be measured in many ways. Measures include sharpness, false color, noise, shading, tone curve, dynamic range, and artifacts. Measures for image sensor quality include resolution, spectral response, high/low light characteristics, defects, angular response, smear, and lag. Sensor quality is generally more objective than the subjective domain of IQ. Also, due to time and motion, camera shake, motion blur, jitter, and temporal noise must be considered. IQ must be viewed with a systems perspective; all equipment must be allocated for a defined purpose as it is exceedingly expensive to construct equipment which provides high IQ under all conditions.

2.4 SUAS and Aerial Imagery

Small UAS have begun to utilize inexpensive and widely available sensors to conduct ISR, and their utility has been proven (Beard & McLain, 2012; Gundlach, 2012). Classification of objects in a scenario can improve the situational awareness for multiple stakeholders. One operational scenario was explored by (Merino, Fernando, Martinez-de Dios, Ferruz, & Ollero, 2006) who focused on geolocation of forest fires from an unmanned helicopter. This research identified many factors to consider with platform (airship vs. helicopter) onboard processing time, off board processing, communications, and software required for fire detection. However, the research did not consider the specific electromagnetic wavelengths to use for feature extraction or application to dismount detections. Nevertheless, this research demonstrated the capability of SUAS to perform object identification in hazardous environments.

2.4.1 Image Geometry and Projection

Imagery acquired from an aerial platform may require consideration of aircraft attitude and position. The impact of attitude and position of an SUAS is found from many sensors onboard the aircraft. The Inertial Measurement Unit (IMU) measurements are converted to attitude positions with a control system and aircraft equations of motion in the autopilot (Beard & McLain, 2012). The autopilot then determines approximate state and makes corrections to its flight path. A body fixed camera maintains a relatively simple geometric relationship to the body frame and inertial frame, compared with a gimbaled camera. Each coordinate frame is related by a rotation matrix, and they can be defined intuitively using the Euler angle system. Euler angles are useful to define an SUAS attitude, and they are combined with the latitude, longitude, and altitude with respect to time for a Six Degree of Freedom (6DOF) system (Beard & McLain, 2012). Figure 2 shows the directions of motion, and moments, as measured by an IMU.
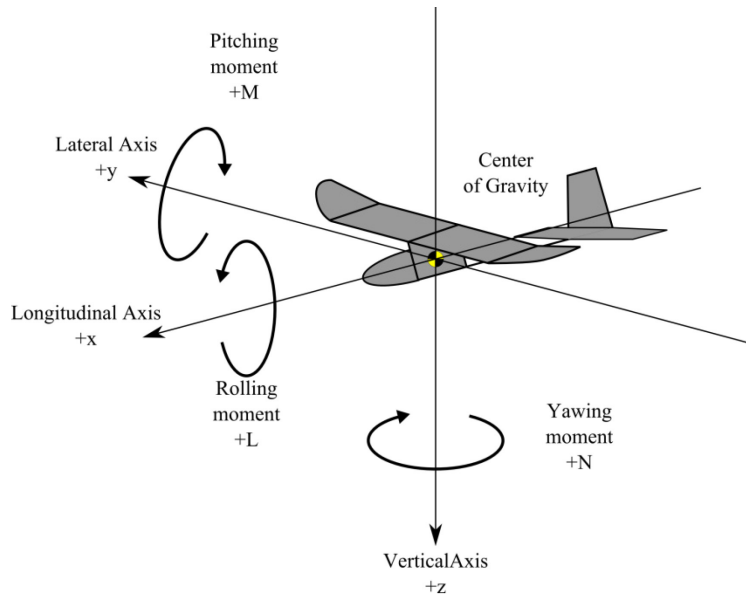
Figure 2: Aircraft body frame axis direction and moments that are measured by an onboard IMU, which

was adapted from Bertin (2002)
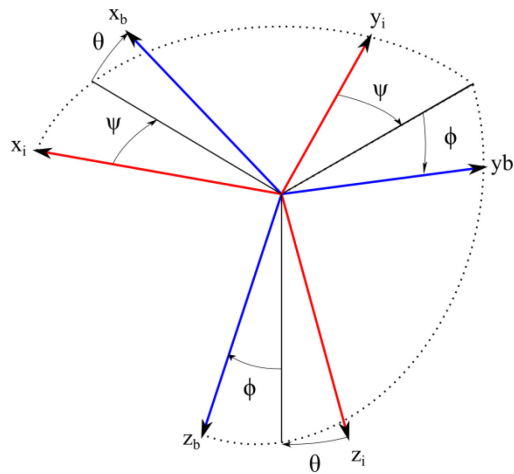
Figure 3: The aircraft Euler angle coordinate system adapted from Premerlani (2009). Euler angle

coordinate systems are expressed for their more intuitive nature compared to Quaternions.

Previous research has used angular relationships to transform imagery. Welborn

(2011) developed an algorithm for determining the location of a sensor with respect to the

14

inertial, or earth frame. His model generated sensor Field of View (FOV) projections to

the ground in a flat earth coordinate system, to determine the length of time that a

stationary object stays in the camera Field of View (FOV). Figure 3 shows the airframe

angular convention. Since telemetry is output from the autopilot in the body frame of the

SUAS, the algorithm used the transformation matrix from the inertial frame to body

frame, and then from body to camera frame. Since the IMU data is given in the body

frame, one can then relate to any frame of reference with a transformation matrix. The

coordinate transformation from the body frame to the inertial frame, is given by (Eq. 1).

The transformation from the body to camera frame is given by (Eq. 2), assuming that the

camera is near the CG (Beard & McLain, 2012). The final aimpoint vector is given by

(Eq. 3). Thus, any sensor aimpoint can be determined approximately from the autopilot

telemetry. It is approximate, because there are inherent errors and drift associated with

autopilot sensors; this makes the data noisy (Beard & McLain, 2012). The sensor

footprint from an SUAS will change over time because the aircraft is moving at each

point in time. Figure 4 shows the camera frame of reference with respect to the inertial

reference frame and the sensor aimpoint.

$$R_b^i = \begin{bmatrix} c_\theta c_\psi & s_\phi s_\theta c_\psi - c_\phi s_\psi & c_\phi s_\theta c_\psi + s_\phi s_\psi \\ c_\theta s_\psi & s_\phi s_\theta s_\psi + c_\phi c_\psi & c_\phi s_\theta s_\psi - s_\phi c_\psi \\ -s_\theta & s_\phi c_\theta & c_\phi c_\theta \end{bmatrix} \qquad \text{(Eq. 1)}$$

$$R_b^c = \begin{bmatrix} -s_{\theta_{sensor}} & c_{\theta_{sensor}} c_{\psi_{sensor}} & c_{\theta_{sensor}} s_{\psi_{sensor}} \\ 0 & -s_{\psi_{sensor}} & c_{\psi_{sensor}} \\ c_{\theta_{sensor}} & s_{\theta_{sensor}} c_{\psi_{sensor}} & s_{\theta_{sensor}} s_{\psi_{sensor}} \end{bmatrix} \qquad \text{(Eq. 2)}$$

$$\vec{A} = \left[R_b^i \right]^T R_b^c = R_i^b R_b^c \qquad\qquad \text{(Eq. 3)}$$

.
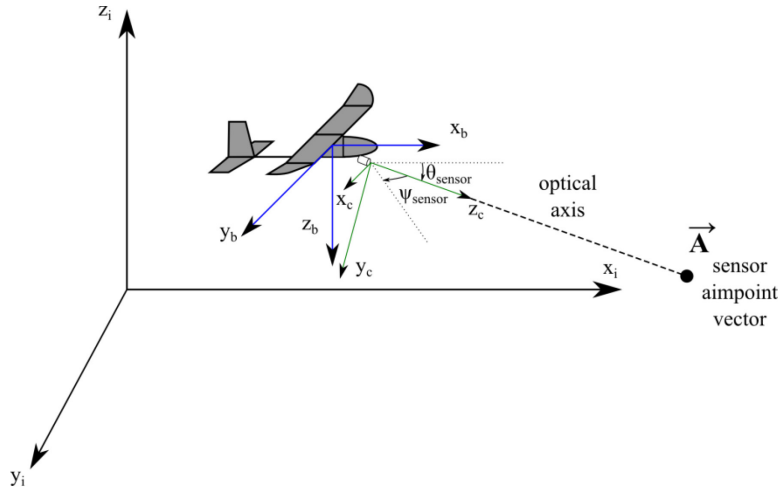
Figure 4: The coordinate system for a camera equipped airframe

Factors such as wind and aircraft vibrations may affect the autopilot pattern, and decrease total time on target. Users leverage the benefits of SUAS as imagery platforms, but they must mitigate the effects of wind on the small airframes. Civera and colleagues (2012) demonstrated the utility of an IMU and GPS for image mosaicking; however, they also used computer vision for feature extraction to increase positioning accuracy. Cho and Snavely (2013) created a ground map from imagery at multiple positions with geometric transformations based on Global Positioning Satellites (GPS) and computer vision algorithms. The applications of aerial imagery with SUAS are limitless.

2.5 Image Registration

Mapping experts have long used registration and rectification to create digital worlds. Registration is the process of aligning or overlaying two images of different

attitude (Rao & Arora, 2004). Rectification is the geolocation of the image to a reference coordinate system (Liggins et al., 2008). Combination of images from multiple sensors is classified as Level 1 of data fusion as described by the JDL model (Kessler, O., White, F., 2009; Steinberg & Bowman, 2010).   When combining images from multiple sensors, it is important to register images for maximum data accuracy; for example, when overlaying a topographical map from HSI, with images from a Visible Spectrum (VIS) camera, the pixels from each sensor's image must map by spatial reference throughout all channels before using most multichannel classification methods. One technique used to determine similar features from two images is Scale Invariant Feature transform (SIFT). SIFT is designed to be unaffected by scaling, orientation, and mostly unaffected by lighting and affine distortion (Lowe, 2004). This makes it ideal for detecting features in moving imagers, and the features can be applied towards image registration.

2.6 Distortion and Camera Calibration

Image distortion is an important topic, because all images have varying levels of distortion or noise that impairs IQ. Recognizing different image distortion types is particularly important for this thesis, because the image fusion methods are subject to distortion. Sambora (Sambora, 2008), described metrics that attempt to measure distortion for multiple aerial sensors including Light Detection and Ranging (LIDAR). He stated that imagery distortion can cause outliers in feature detection and matching algorithms, which can hinder image registration. Feature detection is leveraged for many image registration techniques, and may be impacted by noise. Image distortion is not

17

limited to sensor noise, and can come from atmospheric disturbance, motion blurring, or camera optics.

Aberrations from optics may also account for distorsion. Longitudinal Chromatic Abberration (LoCA), is an occurrence where different wavelengths of light do not converge at the same image point after passing through a lens (Lluis-Gomez & Edirisnghe, 2012). This was discovered when the lens was set to the optimal focus for one wavelength, and then another wavelength was viewed. The image distortion which occurred after the filter change suggested optical properties not accounted for in the optic system. The refraction of light from the glass in the fore optic may vary according to wavelength. Also, using a different glass type in the lens may reduce distortion. Decreasing lens aperture may lessen LoCA, but a higher f-number may decrease light throughput (Lluis-Gomez & Edirisnghe, 2012). Decreased aperture may also limit spherical aberrations, which can account for Airy disks and additional image distortion (Mansurov, 2011).

2.6.1 Single Camera Calibration

Calibration determines a camera's intrinsic and extrinsic parameters. The book by Hartley and Zisserman (2003) explains the importance of a calibrated camera, and also gives a detailed view of formulation of projective geometry. They state that each camera is related to the 3-D world by a camera model. Figure 5 shows the pinhole camera model that relates an image to Euclidian space.
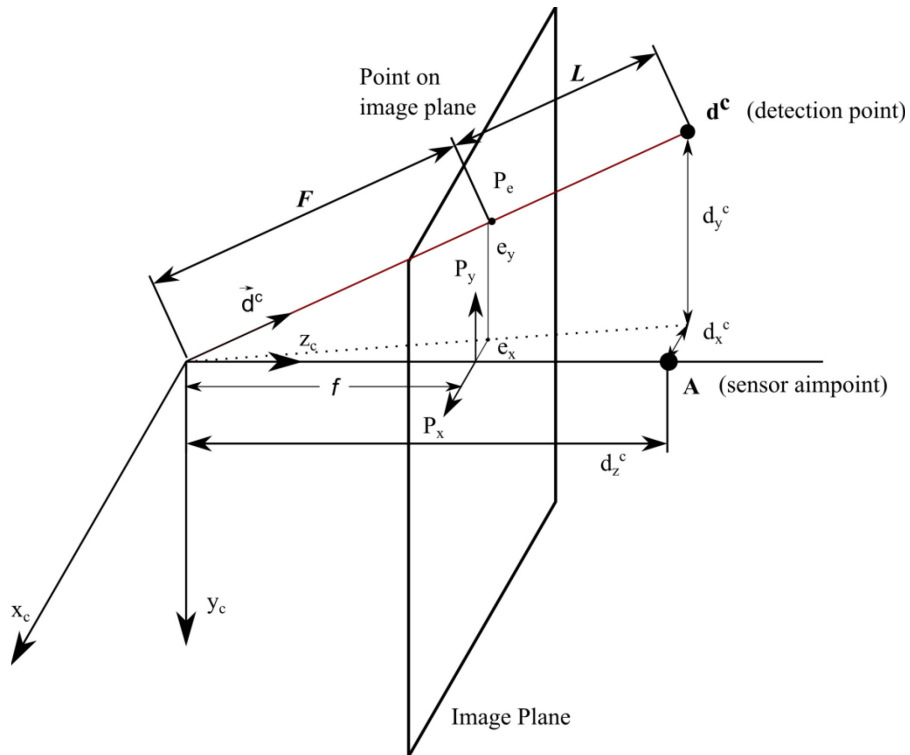
Figure 5: Pinhole camera model for geolocation, adapted from Beard & McLain (2012)

Where:
A = sensor aimpoint
P = image plane
P_e = point on image plane that is a detection.
$e_{x,y}$ = distance on image plane of detection point
F = the distance from the sensor plane to the image plane point P_e.
$d_{x,y}$ = distance in space from sensor aimpoint to detection point.
$\mathbf{D}^c$ = 3-D location of point in space

The importance of a calibrated camera is underscored in aerial imagery because

mapping a pixel location on the aircraft sensor to a location on the ground requires an

image plane that is geometrically similar to the 3-D world.

Finding the intrinsic parameters for one camera is accomplished by utilizing point

matching between multiple images taken by the camera. The images typically consist of

checkerboard patterns, and points between checker squares are extracted by using corner detection. Equation 4 is the camera matrix K, and this characterizes the results of the camera calibration assuming that all points lie on a plane. The camera matrix is used to characterize distortion from sensor so that images can be related to the actual objects.

$$K = \begin{bmatrix} f_x & \alpha_c \cdot f_x & p_x \\ 0 & f_y & p_y \\ 0 & 0 & 1 \end{bmatrix} \qquad \text{(Eq. 4)}$$

Where:
p_x, p_y = Principle point, or center point of image plane
f_x = Horizontal focal length
f_y = Vertical focal length
α_c = Skew coefficient, or scaling between x and y pixel axis (> 0 for nonsquare pixels)

2.6.2 Stereo Camera Calibration

Stereo cameras require further calibration techniques to characterize the relationship between image planes. Two cameras are related by a fundamental matrix, a 3x3 matrix of rank 2, that can relate any point, x_R, on one camera image to a point on another camera image, x_L (Hartley & Zisserman, 2003). The fundamental matrix can be approximated between two non-calibrated cameras (Bouguet, 2013). Knowing the fundamental matrix allows one to determine the location of a point in one camera to the point in another. This case is simplified for two parallel cameras, as shown in Figure 6.

20
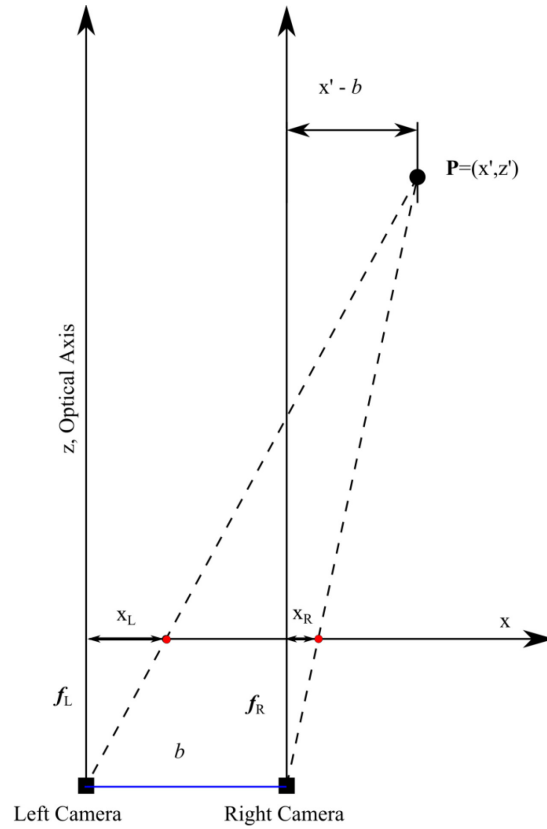
Figure 6: Parallel plane stereo cameras

Where:
(x, z) = Coordinate frame for camera
P = Point on the image plane of both cameras
b = Distance between both cameras in the x axis.
f_L, f_R = Focal length of the left and right cameras respectively

Stereo triangulation can be used to determine the proper registration offset from two cameras. This is possible because of the geometric relationship:

$$\frac{z'}{f} = \frac{(x'-b)}{x_R} \qquad \text{(Eq. 5)}$$

$$\frac{z'}{f} = \frac{x'}{x_L} \qquad \text{(Eq. 6)}$$

21

$$z' = \frac{f \cdot b}{(x_L - x_R)} = \frac{f \cdot b}{d}$$

(Eq. 7)

Where:

x', z' = Image point coordinates in 2-D space

b = Distance between two cameras

x_L, x_R = Points on left and right image planes

f = Focal length, assuming focal lengths for the right and left are approximately equal.

d = Disparity

Therefore, assuming that the focal length of the right and left are similar, we can derive the distance of the point from the camera frames by using(Eq. 7). The value for disparity can also be used to generate a 3-D point cloud from stereo cameras. However, if we know the distance to the point, z, then we can also back calculate d. This disparity becomes the image plane relationship between the two cameras, or homography.

Stereo camera calibration finds the precise homography of the cameras by using a checkerboard pattern held at different angles and distances from the camera. Multiple images are taken from both cameras on the same target checkerboard. Each image pair can be stereo rectified according to the projective transform. The projective transform can be found from the stereo camera calibration, and it consists of two vectors: rotation vector and translation vector. There is a relationship between the position and angle of the two cameras, and it can be determined from a rigid body rotation. Knowing the angle vector, $\vec{r}$, and the translation vector, $\vec{T}$, where

Rotation vector:

22

$$\vec{r} = \begin{bmatrix} \omega_x & \omega_y & \omega_z \end{bmatrix} \tag{Eq. 8}$$

Translation vector

$$\vec{T} = \begin{bmatrix} T_x & T_y & T_z \end{bmatrix}^T \tag{Eq. 9}$$

The rotation matrix for the camera can be related to the rotation vector by the Rodrigues rotation algorithm (Pietro Perona, 1993). The Rodrigues function outputs the rotation matrix R, with $\vec{r}$ as an input. For converting from the rotation vector to a rotation matrix, the parameters defined by (Eq. 10) through (Eq. 13) are used. The Rodrigues rotation algorithm is summarized by (Eq. 14).

$$\theta = \|\vec{r}\| = \sqrt{\omega_x^2 + \omega_y^2 + \omega_z^2} \tag{Eq. 10}$$

$$\vec{\omega} = \frac{\vec{r}}{\theta} \tag{Eq. 11}$$

$$\tilde{\omega} = \begin{bmatrix} 0 & -\omega_z & \omega_y \\ \omega_z & 0 & -\omega_x \\ -\omega_y & \omega_x & 0 \end{bmatrix} \tag{Eq. 12}$$

$$R = e^{\tilde{\omega}\theta} \tag{Eq. 13}$$

$$R = I\cos(\theta) + \tilde{\omega}\sin(\theta) + \left(\tilde{\omega}^2\right)\left(1 - \cos(\theta)\right) \tag{Eq. 14}$$

Where:
θ = Euclidian distance between the rotation vector
$\vec{\omega}$ = Normalized rotation vector
$\tilde{\omega}$ = Antisymmetric matrix
I = Identity matrix (3x3)

A rigid motion transformation for the right camera to the epipolar line of the left camera then gives the coordinates for the right image; this relationship is given by (Eq. 15).

$$X_R = RX_L + \vec{T}$$
(Eq. 15)

Where:
X_R, X_L = matrix of pixel coordinates on right and left images

The projective matrix can be constructed with the geometry given. Therefore, a projective transform can be created to relate the images of the two cameras at any slant distance.

2.7 Imaging across the Electromagnetic Spectrum

Multiple sensors are used in ISR and target detection; cameras can operate at different wavelengths in the electromagnetic spectrum. Although most cameras capture light in the Visible Spectrum (VIS), it is because humans can more easily detect features in this spectrum. Light at different frequencies, for example, in the near infrared (NIR), short wave infrared (SWIR), or far infrared (FLIR), is more difficult to utilize. Many cameras and sensors are equipped to capture these types of light, but to detect and identify different types of objects, classification algorithms are often needed. Figure 4 presents the electromagnetic spectrum, and where IR and VIS sensors are located with respect to their detection wavelength. One can locate the different categories of wavelengths in Figure 7.
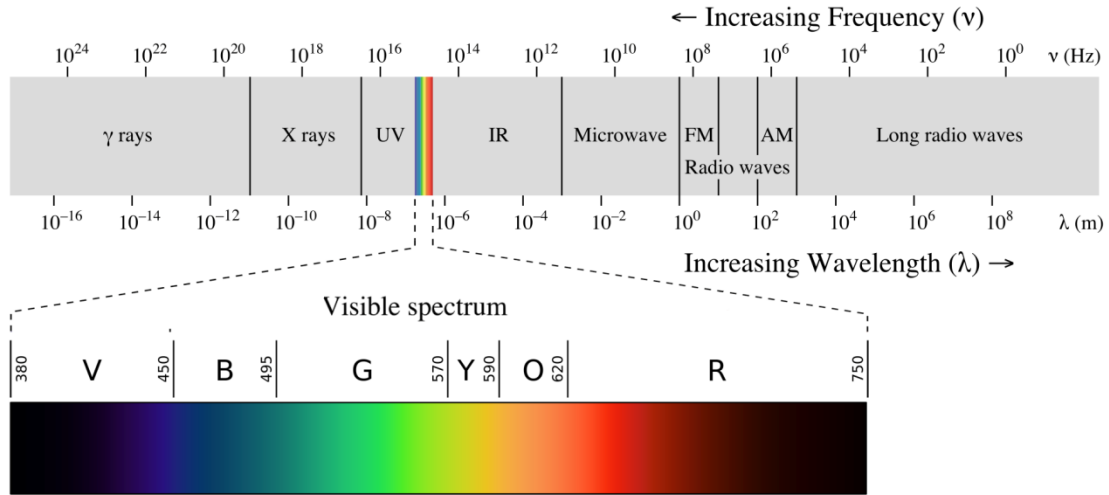
Figure 7: Electromagnetic Spectrum (Ronan, 2013)

2.7.1 VIS Imagers

VIS sensors have been used to conduct ISR and identify targets for decades. Digital Imagery has allowed precise measurements of pixel histograms and color distributions. A typical CMOS EO camera collects data with three channels that are in the VIS. Targets can exhibit unique signatures for the VIS such as matching trees and vegetation with green, and skin or hair with red. Nevertheless, color images may provide irrelevant data for detecting vegetation under different weather conditions or climates; this limits their use in ATR applications (Brand & Mason, 2000). These signatures can still prove useful in combination when combined with other sensors.

2.7.2 Multi-Spectral/Hyperspectral Sensors

Multispectral imagers (MSI) operate at a few broadband wavelengths while hyperspectral imagers (HSI) operate in a few hundred narrow wavelengths on the electromagnetic spectrum from 0.4-2.5μm (Rao & Arora, 2004). These imagers create a

data cube from spectral measurements. Many inexpensive focal plane sensors are responsive up to the near infrared (NIR), but expensive components are needed to segment light at different wavelengths across the sensor plane.

Hsu and Burke (2003) presented the utility of multisensor fusion of HSI and synthetic aperture radar for image classification. They presented a unique Principle Component Analysis (PCA) method to separate HSI bands for multiple target detection, background classification to visually delineate targets, as well as measure target detection and identification performance. HSI can be utilized to detect objects with different physical materials in real time with spectral signatures (Hsu & Burke, 2003). However, they worked with simulated data and perfect image registration, which is far from actual operational conditions.

There are three types of HSI scanning methods: point scanning, line scanning or push broom, and focal plane scanning. A point scanning imager is used to capture one single pixel of data for multiple wavelengths. For example, the ASD FieldSpec 3 can be used to capture highly accurate reflectance data across the spectrum (350-2500nm) but is limited to close range optical fiber or contact probe for data collection (ASD Inc., 2012). The push broom HSI imager utilizes a dispersion device such as a prism or optical fibers to distribute different wavelengths of a single line of pixels. An example of a line scan imager is the SpecTIR LISA built from dual SpecIM imagers (SpecIM, 2013). An image taken from a line scanner is depicted as an image cube in Figure 8.

A focal plane detector, or area scanner, keeps the sensor behind a bandpass filter and objective optic (Grahn, Geladi, & Burger, 2007). In this type of imager, the sensor receives light from a wavelength until the filter is changed. An area scan imager was

constructed in research by Peskosky (2010), but used one entire SWIR camera for each wavelength in a single fore optic or monocular system. Other area scan techniques perform band separation with a patterned filter array in front of a sensor; however, these types of imagers are not widely available (Eichenholz & Dougherty, 2009). Illustrations of each HSI mechanism are shown in the Figure 9 and are adapted from (Grahn, Geladi, & Burger, 2007).

The application of line scan imagers to real time detections may be difficult. Many components are needed for a line scanning HSI, and alignment and calibration of the optomechanics is critical (Grahn, Geladi, & Burger, 2007). A few HSI sensors are included in Table 1 (Beisley, 2012) for comparison. It has long been known that different materials reflect different signatures throughout the electromagnetic spectrum (Morales, 2012). Knowledge of a particular material's spectral reflectance can allow for classification of targets by type. Human skin reflects a unique signature as well; in fact, each person's skin has a unique spectral signature (Nunez, 2009).
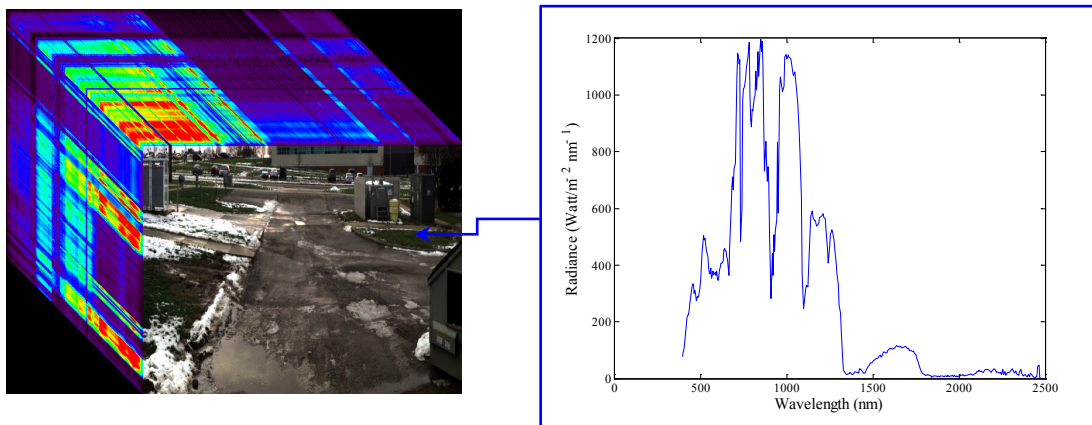
Figure 8: Left, hyperspectral image with 363 bands between 350-2500nm is displayed as a radiance cube, with spectral layers as depth. Right, radiance measurement from a single grass pixel in the scene.
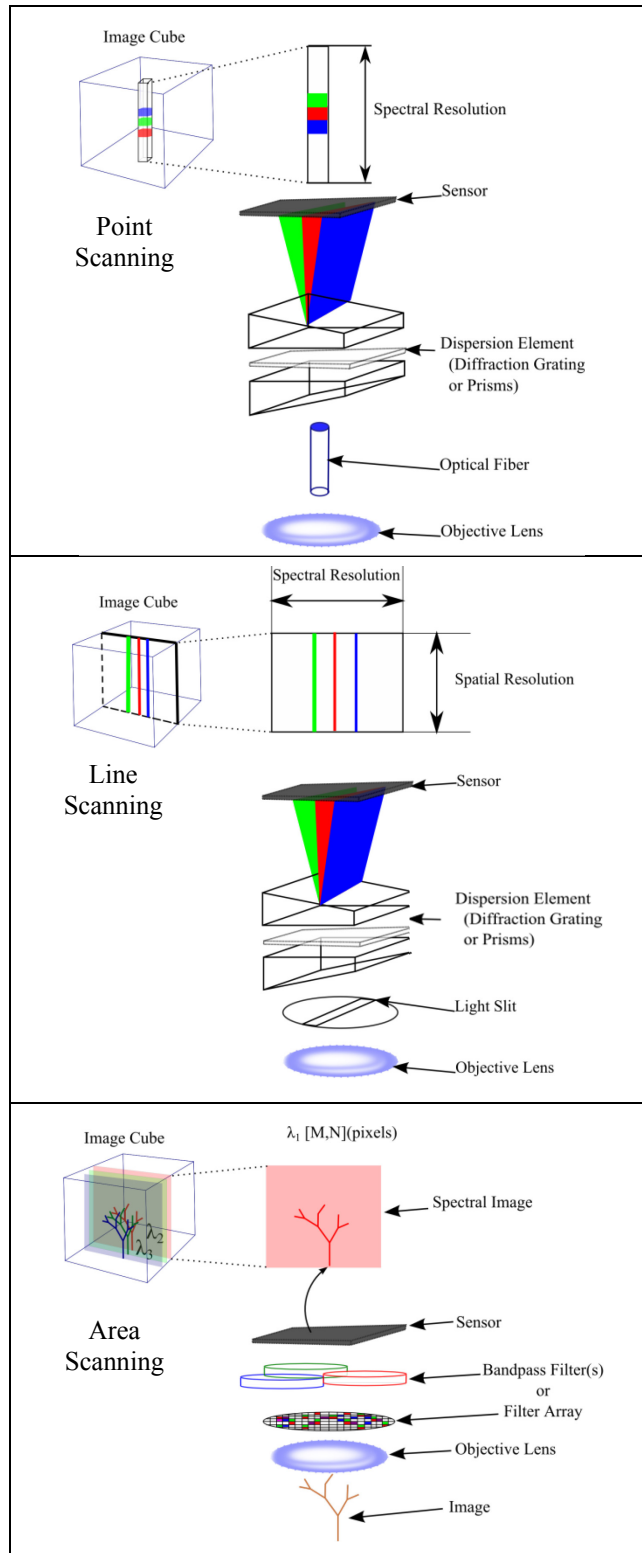
Figure 9: A few types of HSI Imagers and example configurations are shown. Top, portrays a point scan imager. Middle, depicts a line scan imager. Bottom, portrays an area scanning imager arrangement.

2.8 Radiometric Distortion and Calibration

The goal of spectral imaging is converting raw images to unitless values, because this allows a comparison of multiple materials. Properly correcting for imager performance and radiometric distortion is important for imagers under different environmental conditions (Beisley, 2012). Each camera has unique performance parameters for dark current and gain, which need to be accounted for (SpecTIR, 2012). Also, atmospheric conditions change the Sensor Reaching Radiance (SRR) in a multispectral image. The equation for total SRR is given by (Eq. 16). Total SRR is depicted in Figure 10, where each type of sensor reaching light is denoted by an arrow. The literature explains the conversion of digital pixel values to Radiance in greater detail for high altitude remote sensing, and close range imagery (Beisley, 2012; NASA, 2011; SpecTIR, 2012).

$$L_\lambda = L_1 + L_2 + L_3 \qquad \text{(Eq. 16)}$$
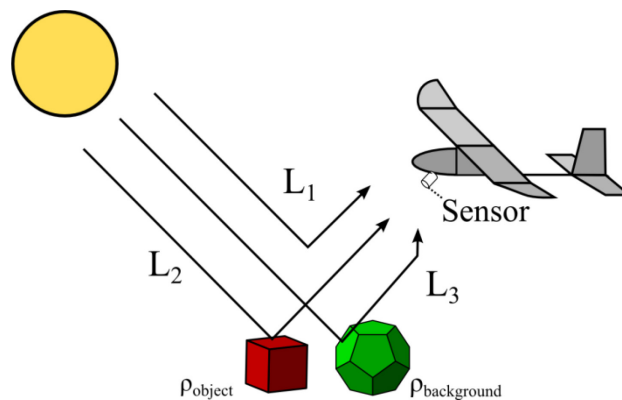
Figure 10: Sensor reaching radiance (SRR) in the visible to near IR spectrum is depicted by arrows emanating from the light source, which is the sun in this case. The sum of all light rays entering the sensor is the total SRR. Adapted from Beisley (2012)

Where:

L_1 = Path radiance, or light scattered directly to sensor FOV
L_2 = Reflected light from object
L_3 = Adjacency radiance, reflected light from neighboring objects
ρ_{object} = Reflectance of object

Radiance is not a comparable spectral measurement for different sensors and environments, and readings are often converted to normalized reflectance. White and Gray calibration panels may be used to determine maximum and minimum radiance, respectively. These are often used to determine the environmental effects (atmospheric vapor interaction, viewing angle, direct reflected sunlight L_2) on electromagnetic energy reflected in an image (Morales, 2012). Most HSI images are transferred from radiance to reflectance by comparing the manufacturer specified values for reflectance on the calibration boards; the boards function as truth measurements (Beisley, 2012). Radiative transfer (RT) codes are also used to convert radiance to reflectance. This relationship provides only an estimate for reflectance and it is specific to high altitude imagers. RT software such as MODTRAN can provide a more accurate estimate for reflectance conversion, and can be used instead of calibration panels. However, poor parameter estimation for sun angles, humidity, CO_2 offset, and other parameters may decrease performance of RT codes (Beisley, 2012). Dismount detection with spectral imagers is little more than measuring light waves reflected from the dismount of interest. Therefore, a detection strategy must account for the location of light, and the atmospheric conditions in the scenario. Reflectance can be modeled as a function of radiance given by (Eq. 17) (NASA, 2011).

$$\rho = \frac{\pi \cdot L_\lambda \cdot d^2}{ESUN_\lambda \cdot \cos\alpha} \qquad \text{(Eq. 17)}$$

Where:

ρ = Unit-less reflectance

L_λ = Sensor reaching radiance $\left[Watts \cdot sr^{-1} m^{-2} nm^{-1} \right]$

d = Distance measure from Earth to Sun in astronomical units

$ESUN_\lambda$ = Mean solar exoatmospheric irradiances $\left[Watts \cdot m^{-2} \cdot nm^{-1} \right]$

α = Sun zenith angle in degrees

2.9 Lighting Effects

The incident angle of light can impact the detection of an object. Koch (2011) denotes the objects' material properties as an independent variable of the apparent reflectance. Skin also has unique reflective properties that make detection with HSI difficult. The relationship between light angle and material property can be modeled by a Bidirectional Reflectance Distribution Function (BRDF), and the reader is referred to the literature for more research on this subject (Comninos, 2011; Koch, 2011). Different angles of reflected light may translate to inconsistencies in the detector's rule based threshold. Models for the BDRF have been derived with empirical and physically-based methods; the models have been used to enhance the realism of 3-D computer graphics (Comninos, 2011). Figure 11 depicts the sun angle and incidence angle of reflection on a dismount with non-orthogonal illumination where α is the sun zenith, θ_i is the angle of incidence, θ_d is the viewing angle from the dismount surface normal. For any light based sensor in changing environmental conditions, an accurate model of illumination is needed to make robust detections.
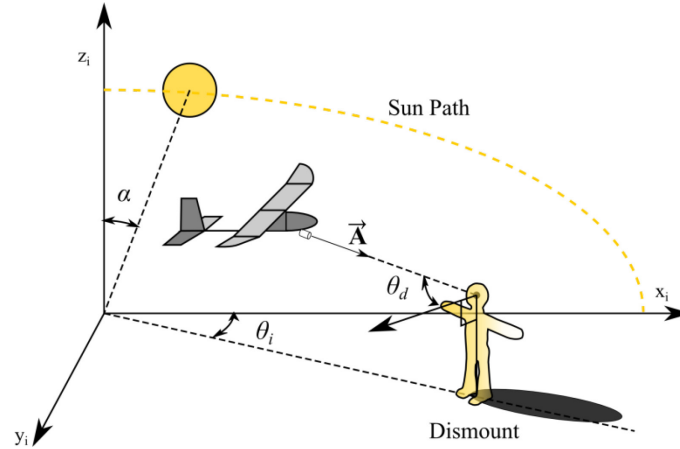
Figure 11: Sun angle affects the measured skin reflectance on a dismount from a sensor

2.10   Object Detection Algorithms

There is a difference between detection and classification (Shaw & Burke, 2003). In a scene that consists of many different objects, a classifier would attempt to code or label each object, while a detector is simply looking for one particular object. This research is concerned with the detection of dismounts. Many object detection methods have been used for HSI imagery, but some require prior, *a priori*, knowledge (Beisley, 2012). Reflectance values for each object material are unique and large libraries of spectral data exist for earthen materials. Software such as ENVI can utilize these spectral libraries to perform classification and detection (Excelis Inc, 2013).

The methods that are exploited for detection of skin on an SUAS are outlined in the next sections.

2.10.1 Normalized Difference Index

A Normalized Difference Index (NDI) for two wavelengths was utilized by numerous researchers (Beisley, 2012; Nebiker, Annen, Scherrer, & Oesch, 2008; Nunez,

32

2009). The Normalized Difference Vegetation Index (NDVI) has been used in

agriculture and forestry to study the water absorption of plants (Nebiker et al., 2008;

Nunez, 2009). The equation for the NDI is given by (Eq. 18), where ρ is the spectral

reflectance for each band, and λ_1, λ_2 are the wavelengths of a spectral image. The NDI

can detect alternate materials by altering the wavelengths λ_1, λ_2 .

$$NDI = \frac{\rho(\lambda_1) - \rho(\lambda_2)}{\rho(\lambda_1) + \rho(\lambda_2)} \qquad \text{(Eq. 18)}$$

2.10.1.1 NDGRI Detection

The basic principle of the NDI classification is comparing ratios of colors to

known ratios for objects. For skin, there is usually a higher ratio of red pixels for higher

levels of skin melanin (Beisley, 2012). For plants, there is usually a higher green ratio.

Using this knowledge of green and red features, the Normalized Difference Green Red

Index (NDGRI) algorithm utilizes reflectance measurements from the red (640nm) and

green (540nm) bands to classify skin (Beisley, 2012). Nevertheless, these two bands

alone proved difficult to differentiate skin or vegetation types (Rao & Arora, 2004). The

ratio for NDGRI is given by (Eq. 19). The NDGRI is a plausible algorithm for skin

detection that can be performed with low cost VIS equipment.

$$NDGRI = \frac{\rho(540nm) - \rho(640nm)}{\rho(540nm) + \rho(640nm)} \qquad \text{(Eq. 19)}$$

2.10.1.2 NDSI Detection

Multispectral imaging can be used in collaboration with VIS to increase detection probability. To overcome the limits of skin detection in VIS cameras, research has investigated the appearance of human skin and background objects in cameras that collect electromagnetic energy outside the range of human vision. While some flesh-colored background objects have the same red, green, and blue components as human skin, they reflect light much differently than skin in the NIR and SWIR ranges of the spectrum. MSI and HSI imagers observe electromagnetic energy across many spectral channels, creating multidimensional clusters of skin and background pixels that are more distinct than in VIS imagery (Beisley, 2012).

This computational combination of VIS and MSI imagery is used to classify objects. The algorithm was effectively validated with prior research from (Beisley, 2012; Koch, 2011; Nunez, 2009; Peskosky, 2010). (Eq. 20) is the Normalized Difference Skin Index (NDSI) algorithm that is applied to the MSI camera data. The skin detection algorithm fuses data in the NDSI and NDGRI domains by setting a threshold. The AFIT monocular and binocular MSI system utilized this algorithm to successfully to detect a wide range of sampled skin types (Nunez, 2009; Peskosky, 2010). These bands identify key features in the spectral signature of that provide a method of segmentation for HSI imagery.

$$NDSI = \frac{\rho(1080nm) - \rho(1580nm)}{\rho(1080nm) + \rho(1580nm)} \qquad \text{(Eq. 20)}$$

2.10.1.3 Combined NDSI-NDGRI Detection

In the Combined Normalized Difference Skin Index (NDSI) algorithm, VIS data are used to lower false detection of vegetation (Beisley, 2012). The reason for using four bands in the electromagnetic spectrum for skin detection is to suppress false alarms. If one used only the SWIR bands in the normalized difference equation, there is a chance that vegetation may be detected as well. However, bands in the VIS spectrum, green and red, show significant differences between vegetation and skin. The VIS band normalized difference can be used to separate vegetation from skin.   The combined score for the NDSI and NDGRI is given by (Eq. 21).

$$d_{NDSI}(x) = NDSI_x - \begin{cases} NDGRI_x > 0 \to 1 \\ NDGRI_x < 0 \to 0 \end{cases} \qquad \text{(Eq. 21)}$$

2.10.2 Matched Filter Detection

Another detection algorithm that has been used with HSI is a Matched Filter(MF). Matched Filters have been commonly used for detections for their robustness and simplicity (Beisley, 2013). The matched filter can provide rapid means of detection compared with other detection algorithms (Excelis, 2013). The matched filter searches for a spectral signature of skin, using a spectral signature as *a priori* knowledge. The score for a MF is defined in (Eq. 22) and a high score indicates a close detection probability.

$$MF(x) = \frac{s^T x}{\|s\|\|x\|} \qquad \text{(Eq. 22)}$$

Where:

x = Pixel vector of all spectral bands
s^T = Spectral signature vector of the desired object such as skin, transpose
$\|x\| = l_2$ Norm of the vector x

Materials exhibit unique spectral signatures over the electromagnetic spectrum. MSI and HSI give us the ability to measure the reflectance of materials in order to classify or detect more accurately than with a VIS or broadband sensor. Figure 12 shows the spectral signature vectors for a few common materials from 350-2500nm that were collected with a point scan HSI in the reflectance domain.
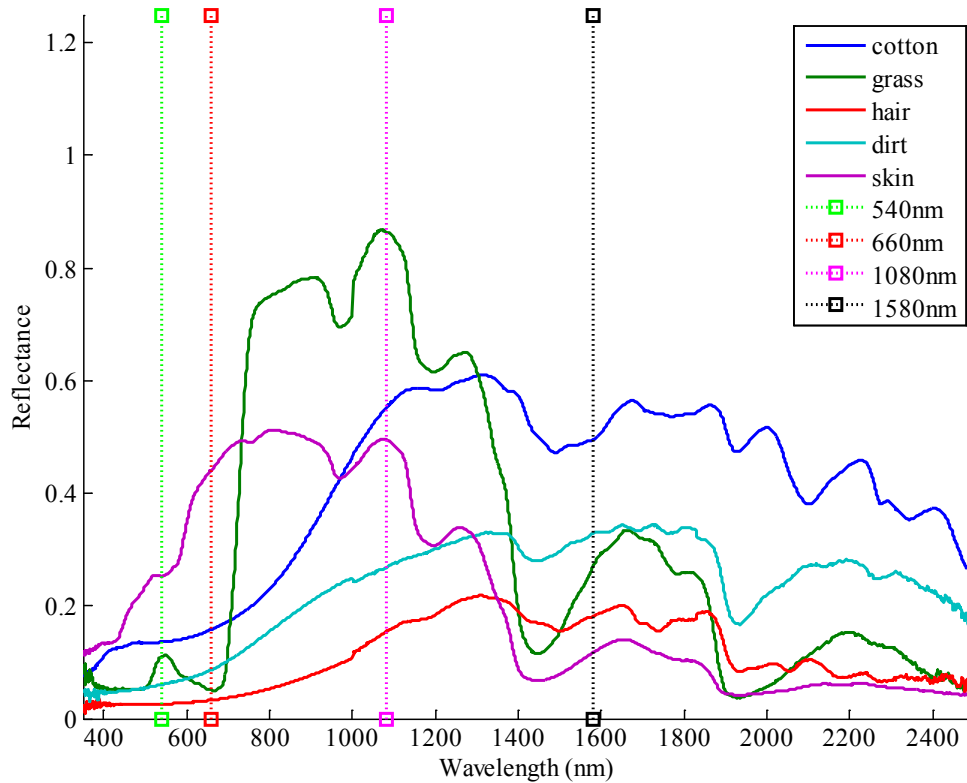
Figure 12: Measurements were taken with an ASD Fieldspec Pro3 spectroradiometer for common materials and their spectral signatures. The vertical lines denote the bands specifically used for the d_{NDSI}.

2.11 Metrics

Metrics are used to make comparison between two systems. The following section describes the measurements used for comparison in this research.

2.11.1 Detection Measurement

Accurate object detection and classification is required for ISR and SAR. Predicting the accuracy of a sensor platform may dictate which platform is required. Furthermore, metrics for measuring the quality of object detection and classification may be subjective or objective. Judging a situation based off these metrics is most aligned with Level 2 of the JDL model (Steinberg and Bowman, 2010). The literature described in this section explores which parameters affect the quality of skin detection, and which factors need to be considered for the environment.

When imaging spectral signatures, each pixel may contain a mix of light reflected from multiple sources. Positively identifying a target is more difficult in the subpixel domain (Morales, 2012). Proper spatial pixel density is essential for a sensor and target detection methods. When targeting spectral signatures, an image must have sufficient full pixels on the target for most algorithms to detect (Donahue, 1991; Morales, 2012). Many metrics have been developed to determine if an image is suitable for its specific purpose. The metrics used in this research are explained below.

2.11.2 ROC Analysis

Each binary classification system has a Receiver Operating Characteristic (ROC). As the classifier lowers its detection threshold, it increases the Probability of true positives (P_{TP}) but also increases the Probability of False Alarms (P_{FA}). A ROC Curve is

37

generated from the Probability of Detection and the Probability False Alarms at different thresholds. Therefore, each point on the ROC curve can be written as a contingency table. Metrics can be measured from the ROC Curve to compare detection systems. Area Under the Curve (AUC) is one measure that can quantify the performance of a ROC Curve.

2.11.3 NIIRS and GIQE

Having the proper pixel density is important for detecting targets. A general metric for judging pixel density requirements is the NIIRS rating. The NIIRS scale stratifies sensor IQ from (1-9) with 9 being the highest level of quality; however, it is largely subjective and only quantifies details down to 5cm (Gundlach, 2012; Kerkes J. P. & Hsu, 2004). An objective metric was developed to predict NIIRS ratings based on objective scales and is called the General Image Quality Equation (GIQE). The NIIRS scale transforms pixel size to Ground Sample Distance (GSD) for an input and GSD is given by (Eq. 23). Relative Edge Response (RER) is the distance it takes to make a clear edge distinction and it is given by (Eq. 24). The final GIQE metric given by (Eq. 25) is useful for conventional imaging systems, but may change when using a sensor for automated target detection, thus the equation has been modified to work with aberrated imagery (Thurman & Fienup, 2010).

$$GSD = pR \, / \, f \qquad\qquad (Eq. \ 23)$$

$$RER = ER(0.5p) - ER(-0.5p) \qquad\qquad (Eq. \ 24)$$

$$NIIRS = c_0 + c_1 \log_{10}(GSD) + c_2 \log_{10}(RER) + \frac{c_3 G}{SNR} + c_4 H \qquad (Eq. \ 25)$$

Where:

p = Sensor pixel pitch
R = Range of object
f = Focal length
ER = Slope of Normalized edge response.
ϖ = 3x3 Sharpening kernel matrix
G = Post processing noise gain, ($\approx$ 1 for raw images)
H = Edge overshoot of an image
SNR = Signal to noise ratio of unprocessed image

2.11.4 Cumulative Probability of Blur Detection (CPBD)

Blur is encountered in moving imagery due to exposure or shutter speed too slow to capture motion. The blur metric measures the image distortion due to motion blur, focus, or other aberrations. It utilizes a digital filter to detect edges in an image, and then applies a threshold window for edges that appear blurred. Another technique to calculate blur may apply a digital filter for recreating blur and then compare the filtered image to the original image. The principal behind the metric is if an image is already blurred, then the difference between the original and distorted will be less significant. The benefits of the blur metric are that it requires no reference image, in comparison to the Mean Square Error, Structural Similarity Index, or Peak Signal to Noise metrics. The algorithm for the CPBD metric is described in detail in the literature (Narvekar & Karam, 2011).

Table 1 shows a summary of the metrics used in this research.

Table 1: Summary of Performance Metrics

Metric	Pros	Cons
NIIRS/ General Image Quality Equation (GIQE)	A widely accepted rating scale for imagery. (1-10), where 10 is the best image quality. Created for standard EO cameras, but expanded to MSI with GIQE	c_i is based off qualitative analysis. The scale doesn't account for spectral dimensionality.
Receiver Operating Curve (ROC) Analysis	Quantify detection accuracy by P_{FA}, P_{TP}. AUC = 1 is a perfect detector. Can be used to select optimum classifier threshold.	Less indicative of quality when the ROC approaches the chance line (from [0,0] to [1,1] in ROC space)
Cumulative Probability of Blur Detection (CPBD)	Image quality metric that does not require a reference image. Objective quantity that compares well to subjective metrics.	Low resolution images or images without defined edges may not be accurately characterized.

2.12 Summary

This chapter explored the concepts and background of target recognition in aerial vehicles. Furthermore, it showed a few basic methods and metrics to fuse imagery data and extract information for data fusion. The next chapter explains the method, experiments, and data used to substantiate the theories reviewed in this chapter.

3. Experimental Design and Construction

3.1 Chapter Overview

The methods for accomplishing the research goals are systematically structured; the Systems Engineering methodology is used for the approach of design, testing, and construction. The steps of the approach are listed:

1. Conceptual Design
2. Preliminary Design
3. Detailed Design
4. Evaluation Metrics

First, the conceptual design originates from the customers or stakeholders in the form of a problem statement or Concept of Operations (CONOPS). Next, system level requirements are derived from the problem statement, and a functional baseline is established. Several requirements are always limited by the research scope, or the available equipment, timeline, and budget, so demonstrational requirements for a prototype system are defined. Then, the preliminary design narrows the design space; an allocated baseline and Technical Performance Measures (TPMs) are then established. From there, detailed design and development leads to definition and construction of subsystems and major elements such as drawings, parts lists, and test plans (Blanchard & Fabrycky, 2010). Finally, the metrics used for validating the requirements are explained. The scope of this study precludes further exploitation of the systems lifecycle, and thus for this research the final level of "utilization" is not considered.

3.2 Conceptual Design

The goal of systems engineering is to execute a process that creates an end product or tool that is useful, efficient, and robust. Using this methodology, the problem was initially defined: *measure the feasibility of a skin detection multispectral sensor on an SUAS for Search and Rescue operations.* The conceptual requirements derived from the problem scenario, include:

- Operation in an austere environment with minimal operators;

- Range and speed that allows SAR operations;

- Sufficient slant distance for extreme environments;

- Adequate pixel density for detecting skin on a dismount;

- Imagery that allows positive identification of dismounts.

3.2.1 System Requirements

System level and technical requirements were then derived. An airframe that could withstand the environmental conditions of a forest fire, or thunderstorm would be ideal for austere operation. Minimal equipment on the GCS would make the system easier to use and require less operators. An airframe power delivery system that provides ample range, speed, and flight time for coverage of large areas helps to achieve the SAR mission. A multispectral imagery system presents a valid method to detect skin and dismounts. For real time dismount detection on an aerial platform, an area scanner system presented the best method of spectral imaging. Area scanning imagers minimize registration processing to create an image cube, and having simultaneous imagery of

42

different spectral bands makes the system viable for near real-time detections. Slant distance requirements are related to the nature of the environment, and sufficient slant distance is required to keep the airframe flight worthy in high radiation or heat conditions. Peskosky (2011) proposed a 215m slant range and 5cm pixel size requirement for SAR. Pixel size was determined from pixels needed on a face or hand for detection, and this is shown on Figure 13. Finally, imagery that meets subjective and objective quality standards is required for operators and ATR; adequate frame rates and high true positive detection rates allow more information to be gathered from a scene such as the size, number, or location of dismounts.
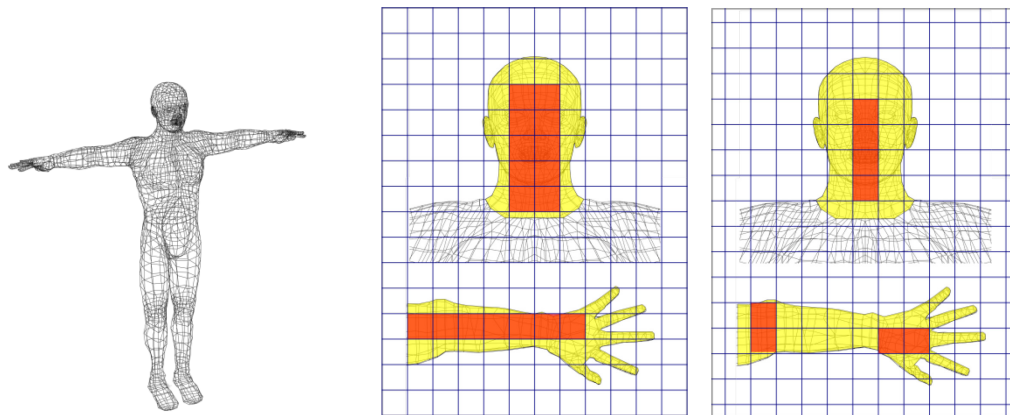
Figure 13: Red area denotes full skin pixels, and yellow area denotes partial skin pixels. Left shows a representative dismount. Middle, shows the most dense pixel distribution on average sized face and hand. Right, shows the least dense pixel distribution on face and hand. A grid size of 5cm was used.

3.2.2 Flight Expedient Prototype Requirements

Due to the scope of this research, the flight expedient prototype system could not satisfy all requirements set forth by the operational requirements. The first difference was the airframe. The available prototype airframe exhibits comparable performance to

43

other SUAS in its size category for speed and altitude; however, the airframe did not meet the requirements for operation in an austere environment. The prototype airframe was limited to 15-20 minutes flight time and constructed with materials that are less than favorable for forest fire SAR. The second difference was the MSI sensor. Due to the cost and availability of area scanners, a high frame rate and fast changing filtering setup replaced a multi-sensor system. For the single sensor system, to vary the bandwidth of light to the sensor a variable Thin Film Transistor (TFT) filter was considered. Also, a patterned filter array was considered. However, due to costs and modification needed for each of these filtering systems, a filter wheel with multiple bandpass filters was chosen for this research. A filter wheel was within budget, and materials were available for construction. Achieving high frame rates with an alternating filter element had new challenges that are discussed in this chapter. The third difference between operational requirements and prototype configuration was the video processing architecture. Real time detection ability was limited due to the wireless transmission requirements, and so data was stored onboard the autopilot and digital video recorders. The fourth difference was operating altitude and slant distance. The slant distance requirement could not be met due to optics availability; therefore, shorter distances were used for testing. Altitude for test flights ranged from 30-60 meters, similar to the operational testing done at Eglin, AFB for small forest fire monitoring (Aeryon Labs Inc., 2013). Pixel size was determined to vary between 5.0 and 8.0 cm with the available optics. This was within the bounds of the system requirements. Flight expedient prototype requirements, which satisfied all achievable operational goals with the budgeted resources, are outlined in .

Table 2.

44

Table 2: Flight expedient prototype requirements for SUAS MSI system

Requirement	Value
Airframe	
Endurance	10-20 min
Speed	10-20 m/s
Propulsion	Battery-Electric
Power/Weight	110-220 watts/kg
Weight	<10kg
Altitude	30-50 m
Payload	< 2 kg
Launch Mechanism	Conventional / Hand launch
Recovery Mechanism	Conventional / Grass
Optical	
Slant Distance	42-100 m
Pixel Size	5.0-8.0 cm
FOV[1]	25° diagonal
Optical Design	Refractive
Frame Rate	1 fps
Sensor pitch	25μm (4/3" sensor)
Spectral	
Wavelength Sensitivity	350-1600 nm
Bands CWL[2]	540, 660, 1050, 1550 ± 8nm
Bandpass FWHM[3]	10 ± 2nm

3.3 Preliminary Design

3.3.1 Sensor considerations

The SWIR camera was chosen based on availability and compatibility. Peskosky

(2010), utilized the Goodrich SWIR cameras to create a 4 sensor skin detection platform.

The Goodrich SWIR camera can detect wavelengths from 600-1700nm; it includes

multiple user adjustable parameters such as gain, exposure, bad pixels, and frame rate.

The camera has the option to output digital and NTSC video as well. The sensor angle,

---

[1] Field of View
[2] Center Wavelength
[3] Full Width Half Max

slant distance, and altitude was then chosen based on airframe considerations. Next, a lens size was chosen based on HSI sensor parameters. This lens must allow adequate pixel density from a safe aerial slant distance; slant distance is measured from the camera lens, to the region of interest. Field of View (FOV) was also attained from lens size. After determining the SWIR camera configuration, VIS camera selection was initiated.

The investment costs of testing and components were considered in this research. The cost of VIS cameras was not nearly as prohibitive as the SWIR. Most VIS cameras surpass the SWIR in resolution, are smaller in size, and require less power. Integration of the VIS camera was not as challenging as the SWIR. Nevertheless, any multimodal imaging system benefits from similar intrinsic and extrinsic properties for image fusion. The VIS camera provided onboard data storage, good IQ, low cost, and a small form factor.

The algorithm available for skin detection was then determined. From the literature, a proven algorithm for skin detection is the NDSI and NDGRI. This approach utilizes 4 bands in the VIS and SWIR light spectrum, 495–570nm, 620–750nm, 1050-1100nm, and 1550-1600 nm. For the first two bands, a VIS camera can be used to collect data. For the second two bands, a SWIR camera can be used to collect data. Several methods have been used to separate and collect these electromagnetic spectrums, and they are described in Section 2. Restricting light to 1050 and 1550 wavelengths with the SWIR required at least two bandpass filters. This detection method thus dictated the optical equipment that would need to be added to the sensor package.

Each optical filter alters the electromagnetic signal (light) transmittance. In a filter wheel, each optic is mounted to a rotating wheel which passes in front of the sensor

plane. Using multiple filters to take images of the same object creates spectral depth, and allows construction of an image cube. However, constructing an image cube with a moving vehicle requires additional processing. This drove technical requirements for the filter wheel. The filter wheel must be capable of switching between bands fast enough to allow similar features to appear in each subsequent image for computer vision registration. After experimentation with different values of video registration overlap, a 50% overlap consistently provided enough common features for images. Proper registration accuracy was highly correlated to detection accuracy. Since sensor payload required for skin detection dictated airframe selection, the sensor integration required careful consideration for use on the parameters of the aerial platform.

3.3.2 Airframe Selection and Modification:

There were a few options for airframes available at the AFIT Advanced Navigation Technology Center and Systems Engineering Departments. The AeroVironment Raven, Bixler Super Sky Surfer, and Sig Rascal 110 were all considered as test beds. All were in the same Group I category, therefore none exceeded 9 kg (20lb) gross weight, exceeded 51 m/s (100 KIAS), or would exceed 365m (1200ft) AGL operating altitude. These categories are defined in the AFI 11-502 (Department of Air Force, 2012) . Among the requirements considered, the most notable were:

1. Capability for holding a sensor platform of known weight and size

2. Environmental robustness of the aerial system to withstand varied conditions

3. Capability of the airframe to sustain flight for takeoff, navigation to a known waypoint, and return flight

First, the smallest capable airframe of holding the sensor payload was considered; this airframe is the Sig Rascal 110. This airframe is capable of carrying a 2.5 kg payload, and was known as a stable platform for performing SUAS research (Jodeh, 2006). However, there are several variations of the Sig Rascal. Gasoline and electric variants have certain tradeoffs for flight time, weight, operator usability, noise, and payload. Since fixed body cameras are sensitive to vibrations, the best airframe for a skin detection sensor system would minimize vibrations. The electric powered Rascal variant had less vibration than the gasoline powered variant, while still allowing adequate flight time and payload capacity (Giacomo, 2012). The one requirement the Rascal could not achieve Considering all tradeoffs, the electric Rascal was chosen as the airframe for research.

A preliminary flight test was done without the MSI sensor, and it was useful for characterizing the airframe speed, stability, and oscillatory performance during flight. Design choices were made with flight data from a representative SAR flight pattern. The airframe's speed dictates how fast objects move through the sensor's FOV. Therefore, the speed of the airframe determined the requirement for frame processing rate; because there was only a short amount of time to capture images of the same object. A flight test was then conducted to measure the cruise speed, and adjust the autopilot control gains for a simulated sensor payload. Tuning the gains for coordinated flight paths in windy conditions was crucial for autopilot navigation. Testing data was then used for deriving other prototype system requirements.
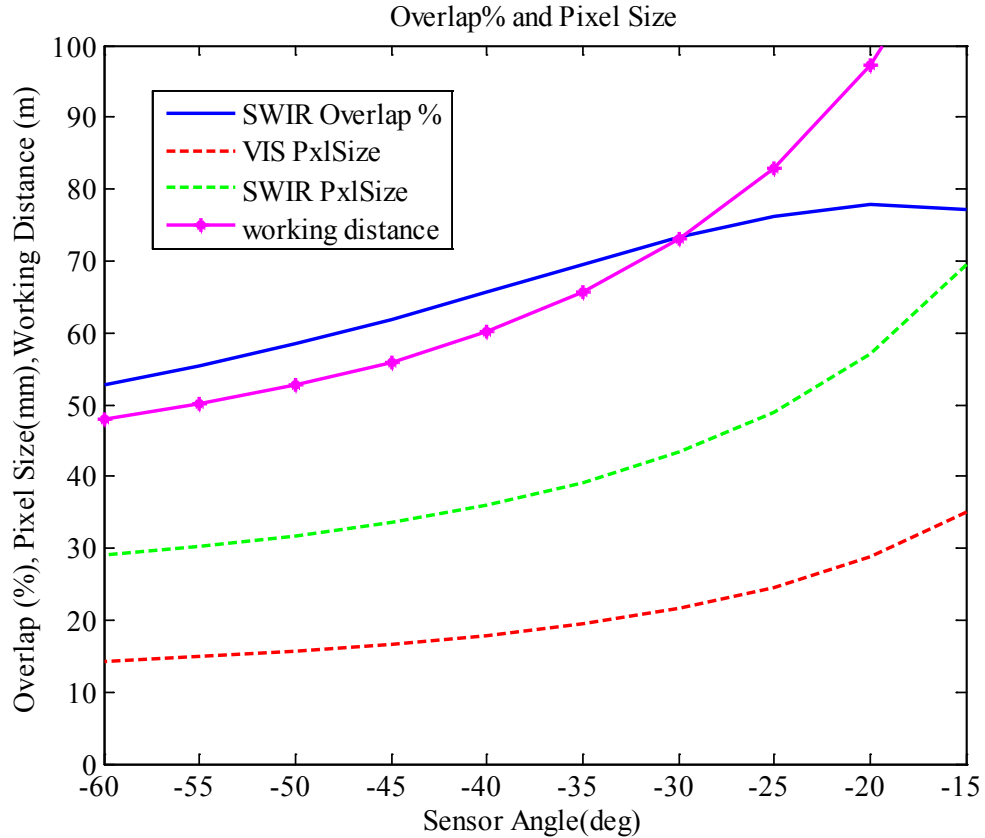
Figure 14: Comparison of different sensor angles using test flight telemetry at 32m AGL. For a filter change rate of 0.5 Hz, the corresponding frame overlap %, working distance in meters, and pixel size for SWIR and VIS sensors in mm is displayed.

Flight telemetry could be used in lieu of further testing to predict camera movement and geometry. A Monte Carlo analysis was applied to straight line passes of the rectangular or "race track" flight pattern to predict sensor FOV across different sensor angles. Figure 14 shows a few parameters changing as a function of sensor declination angle. The green and red lines show camera pixel size in millimeters from the image plane on the ground. It can be seen that the VIS camera pixels are significantly smaller

than the SWIR, and this makes sense, due to the resolutions of each camera. The purple

dotted line shows the working distance, which is the distance from sensor to ground. The

blue line shows the percentage of overlap for the SWIR FOV given 2 frames per second.

The maximum attainable overlap appeared near -15° sensor declination angle. However,

the smaller magnitudes of sensor declination also increased pixel size. The simulation

was used to determine the optimum θ_{sensor}, which was -30° for the 2 fps SWIR image

acquisition rate.

3.4 Detailed Design

Detailed design involved assembling the components to subsystems, and then

testing each separately. Integration testing was then completed with the subsystems

during ground testing. These components all composed the SUAS Multispectral

Detection Platform as shown in Figure 15. This allowed key components and settings to

be changed before operational testing.
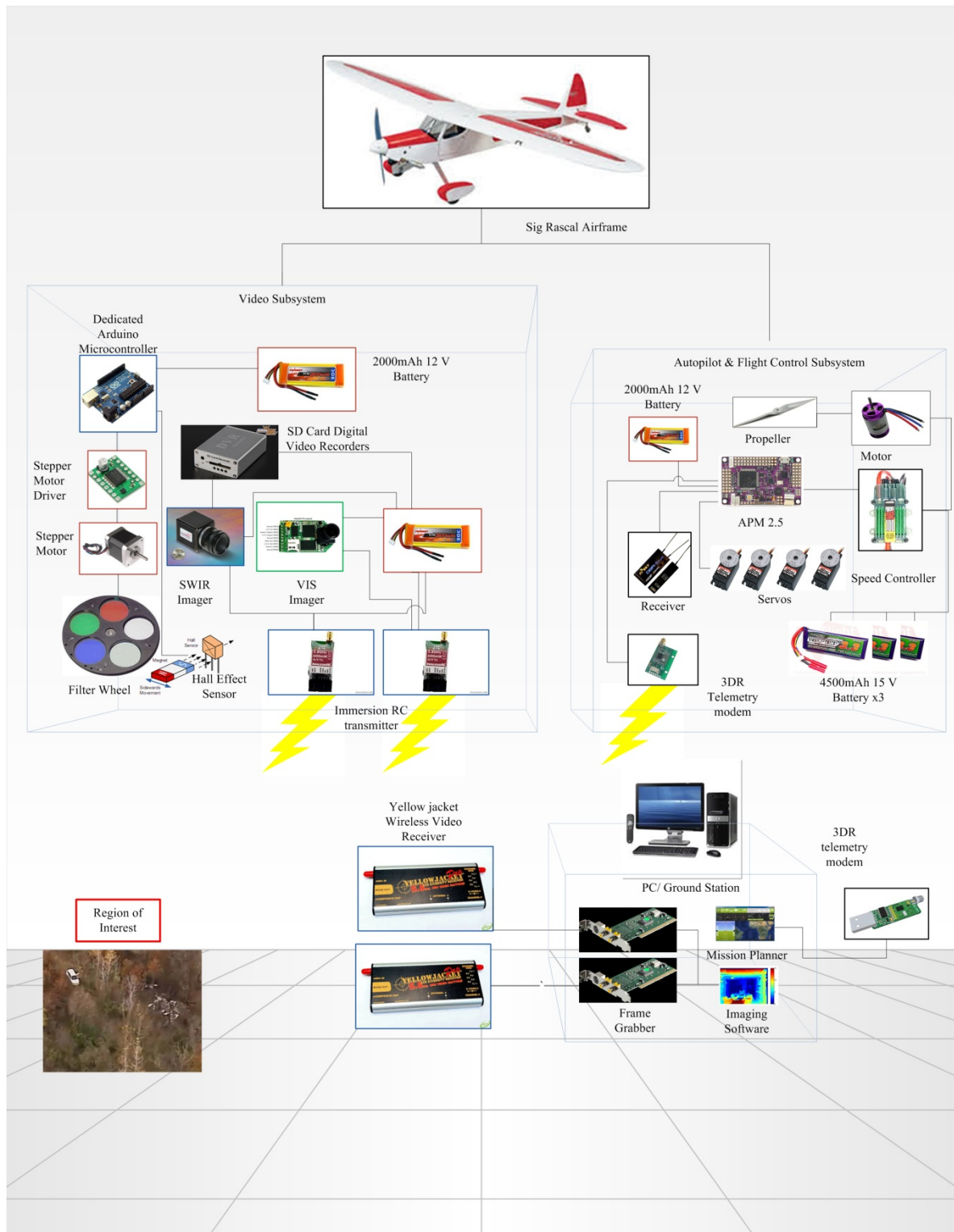
Figure 15: Physical system architecture for SUAS MSI

3.4.1 MSI Video Subsystem

For the SWIR bands, a Goodrich InGaAs sensor was used. Each setting in the Goodrich SWIR camera needed to be adjusted for use in the video subsystem. Settings that could alter the skin detection ability include: digital gain, look up table (LUT), contrast factor, pixel offset value, bad pixel mapping, and enhancements. As described in Section 2, radiance conversion requires that the SWIR camera's signal processing system first captures light on an InGaAs sensor array. Next, it applies gain, and analog offset video, before processing by the analog to digital convertor. After digital conversion, the video is modified for bad pixel offset/gain/replacement, user enhancement controls (i.e. contrast), Lookup table control, and then it is output to a digital or analog port.

For the VIS bands, a hobbyist camera was used. The camera settings of the VIS were less sensitive than the SWIR because there were no moving components needed to separate wavelengths. The VIS camera segments data to 660nm, 540nm, and 470nm channels with Bayer patterning (Omnivision, 2009). Specifically, the Auto Gain Control, exposure, pixel map, were able to be kept at factory settings without modification. For the particular camera selected, the video signal was output to NTSC in real-time; however, the full sensor resolution was not available with this option. To utilize Full High Definition (FHD) VIS video, onboard storage was used for detections.

3.4.1.1 Lens Selection

For the SWIR sensor, a compact fixed focal length lens was selected. This lens form factor was chosen for its small size and weight on the aerial mounting platform. The lens focal length, which was 35mm, was chosen for proper pixel density and FOV. The fused silica lens type was chosen for its high transmission, which is a measure of

52

light throughput in a material; index of refraction, which is a ratio of the speed of light in a vacuum to light in the material; and dispersion, which is a measure of the change in the index of refraction when wavelength changes (Edmund Optics, 2013).

The sensor format, resolution, and spectral sensitivity of the VIS camera required unique lens consideration. Research indicated that a low pass filter would block IR wavelengths, while transmitting the VIS wavelengths (Peskosky, 2010). IR light can produce inaccurate reflectance conversions from VIS imagery. Therefore, a low pass filter was installed in front of the sensor to increase color response of VIS wavelengths. Due to the sensor resolution, the lens chosen for the RGB camera had a focal length adjustable between 9-22mm. A focal length around 12mm was chosen, and provided double the pixel size of the SWIR camera pixels; this required images to be scaled when registering with SWIR images.

3.4.1.2 Data Logging and transmission

The SWIR imager data logger was an analog input DVR. The native resolution of the SWIR imager is 640x512, and the analog output was NTSC (640x480). The video was stored on Secure Digital (SD) cards, and recorded at a maximum resolution of D1 (704x576). Due to the format conversion to NTSC, the maximum recorded resolution on the SWIR system was 640x480, so scaling corrections were needed on the video during processing. Ideally, a digital frame grabber or transmitter is used to allow high speed triggering and frame acquisition. However, the size, weight, and cost associated with a digital solution restricted use of digital storage for the SWIR channel. An analog video transmitter sent video to the GCS for operators to determine appropriate flight patterns.

3.4.1.3 Filter Wheel Design

The operational requirement of the MSI system is the ability to capture images over multiple wavelengths. For this requirement, a filter wheel with different filters was chosen for cost and availability. Knowing the proper filter position may be important for any configuration with multiple filters. For the feature detection algorithm chosen, using the correct wavelength is essential. The Hall Effect feedback system can be used to sense filter changes, locate the position of the filter wheel, or monitor wheel position while it is moving. Furthermore, the algorithm employed to detect skin in this research is sensitive to the difference between sequential frames that are captured on the SWIR imager. Thus, a derived technical requirement was adequate filter changing speed. The design minimized time between band changes to improve image registration accuracy.

A filter wheel system is constructed of multiple parts. First, there is a filter wheel to hold the bandpass filters. The wheel has six positions for filters, and any type of filter can be inserted; however, bandpass filters were used and each one enabled transmission of light at a specific wavelength. Second, there is the stepper motor, which rotates the filter wheel; the motor must be able to switch filters at an adequate speed, and draw as little current as possible. Third, there is the filter positioning sensor shown in Figure 16. The sensing system is constructed of Hall Effect sensors and magnets that can tune the location and speed of the rotating filters. Fourth, there is the motor driver shown on on Figure 17, left. The driver is built with a transistor array which sends pulses of current to a motor's coils. Increasing the frequency of pulses causes a stepper motor to increase rotation speed. Fifth, is a microcontroller that controls the speed and duration of motor pulses. The microcontroller, which is shown on the right in Figure 17, can be

54

programmed to send a velocity profile to the motor driver, read data from the position sensing, or transmit data to the autopilot with serial communication. Sixth, is the filter wheel housing shown in an exploded view on Figure 18. The filter wheel housing was constructed from lightweight polymer using additive manufacturing techniques in order to save weight and create detailed features that are expensive and time consuming on a conventional milling machine. The motor, filter wheel, and sensing system are mounted on the housing, which provides protection from the environment.
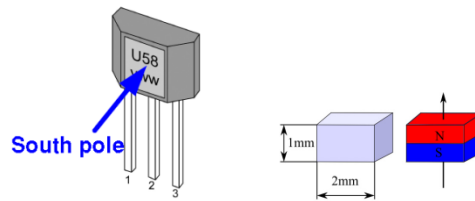
Figure 16: Left, Hall Effect sensor (Melexis, 2006). Right, shows earth magnet and direction of field.
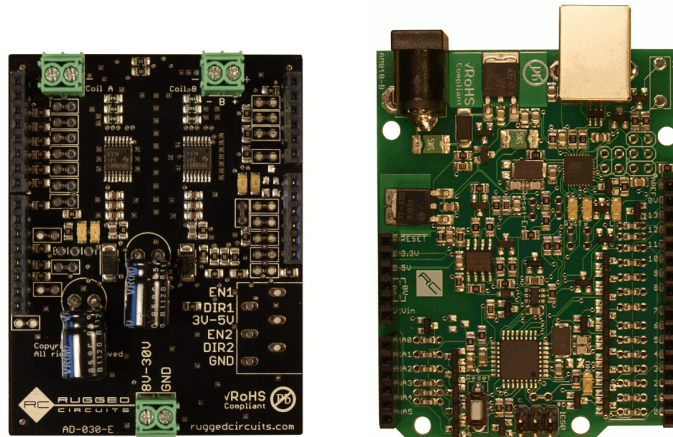
Figure 17: Left, shows Rugged Motor Driver. Right, shows microcontroller (Rugged Circuits, 2013)
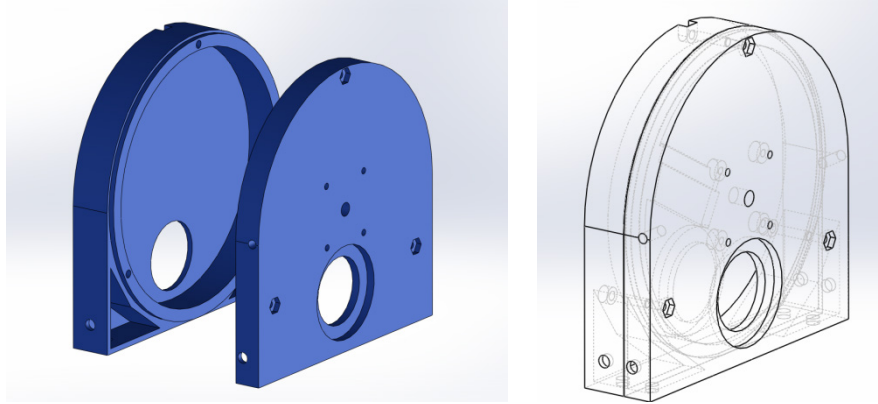
Figure 18: Left, depicts an rendering of the filter wheel housing model. Right, depicts a wireframe model.

There are several technical requirements for the stepper motor and driver; size, weight, and filter location accuracy of the system. A COTS system for switching filters with a filter wheel is the ThorLabs FW-103H filter wheel, and a Thor BSC-101 stepper motor driver. To move the sensor within a prescribed amount of time, the driver must supply sufficient voltage to the stepper motor. The motor driver can deliver a trapezoidal velocity, or constant speed profile to the stepper motor (Thorlabs, 2010). The driver is exceptionally accurate due to the Hall Effect sensors which indicate filter wheel location and speed, however, the system is prohibitively large and heavy for an SUAS application. For this reason, a small stepper motor driver was built.

Stepping the motor to specified velocities and accelerations required calibration to ensure proper filter position. After each step, small inconsistencies in velocity and acceleration can accumulate over multiple steps, and this may cause misalignment. To control the filter wheel in a closed loop system, sensors were used to provide a feedback loop. Hall Effect sensors that measure magnetic flux density were installed, and used to determine filter wheel position and alignment. The sensors communicate with the driver

by sending logical values of LOW or HIGH if there is magnetic flux greater than the threshold amount. The US5881 Hall Effect sensors that were used in construction of the filter assembly have a threshold, B, of 20mT, at 5V operating voltage (Melexis, 2006). The relationship for determining gap is given by (Eq. 26) (Supermagnete, 2013). Parameters from Table 3 are for the chosen magnets and used in(Eq. 26). Using Finite Element Method Magnetics (FEMM), the required distance between the filter wheel and Hall effect sensor *z*, was determined to be 3.5 mm. Figure 17 visualizes the magnetic flux distribution for the Neodymium-Iron-Boron (NeFeB) magnet using visualization model using FEMM (Meeker, 2013).

$$C = \frac{L \cdot W}{2z\sqrt{4z^2 + L^2 + W^2}}$$

$$D = \frac{L \cdot W}{2(D+z)\sqrt{4(D+z)^2 + L^2 + W^2}}$$

(Eq. 26)

$$B = \frac{B_r}{\pi}\left[\arctan\left(C\right) - \arctan\left(D\right)\right]$$

Table 3: Properties and dimensions for NdFeB N42 magnet

B_r	Residual flux density	1.28-1.32 Tesla
L	Length	2.0 mm
W	Width	2.0 mm
D	Height	1.0 mm
z	Distance from pole face on symmetry axis	3.5 mm
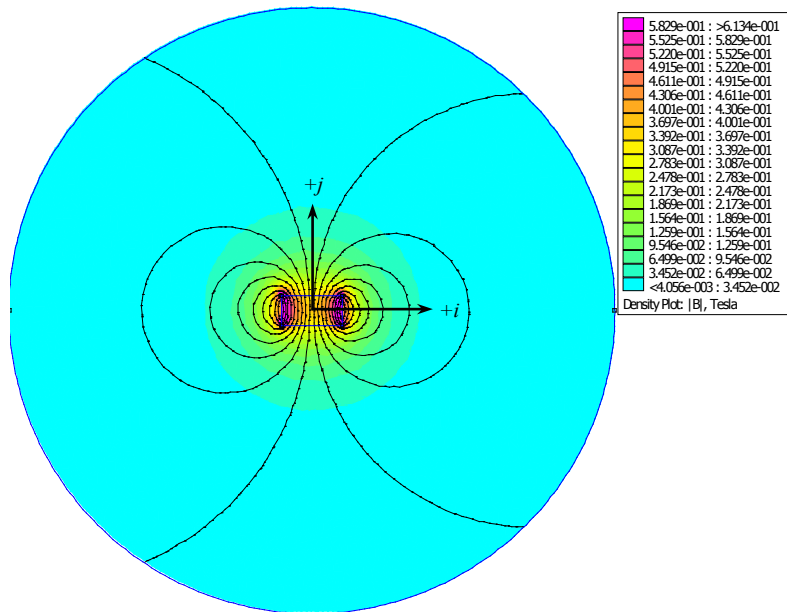
Figure 19: Left, The magnetic flux distribution for filter wheel position indicator magnets is visualized.
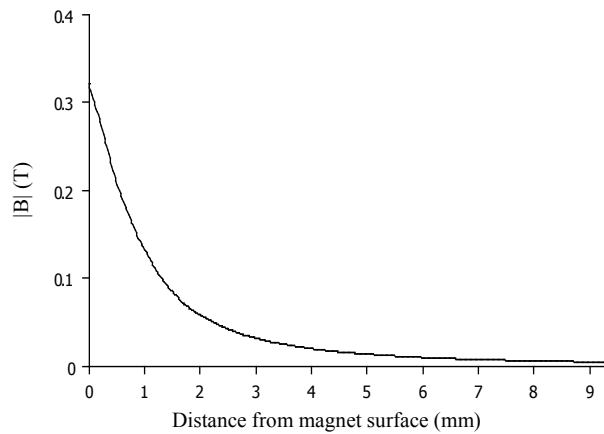
Figure 20: The magnitude of magnetic field is displayed as a function of distance from magnet surface on the magnet vertical (+j) axis. The proper distance between the magnet and sensor was required for the US5881 to activate.

The stepper driver supplied by Rugged Circuits was integrated to the microcontroller, which is based off the Arduino interface. The driver was programmed to operate in constant speed, and the AccelStepper library allowed for custom velocity

58

profiles (McCauley, 2013). Thorlabs utilized a trapezoidal velocity profile to achieve

consistent steps (2010); however, experiments showed trapezoidal velocity profiles were

less predictable as battery charge decreased. The effect of battery life on both velocity

profiles is illustrated in Figure 21. The trapezoidal stepper pattern was applied and tested

on the Arduino stepper driver; however, accuracy of steps was not consistent. For this

reason, the filter wheel was programmed to operate at a constant speed. Hall Effect

sensors were programmed to report filter wheel position.

The stepper driver was programmed to first output a signal when the zero position

was reached, and then output a signal when any filter was directly in front of the camera

optic. This allowed for filter position to be known for real time processing of SWIR

footage. Without the proper filter location sensing equipment, the triggered image may

inherit multiple types of aberrations (Edmund Optics, 2013).
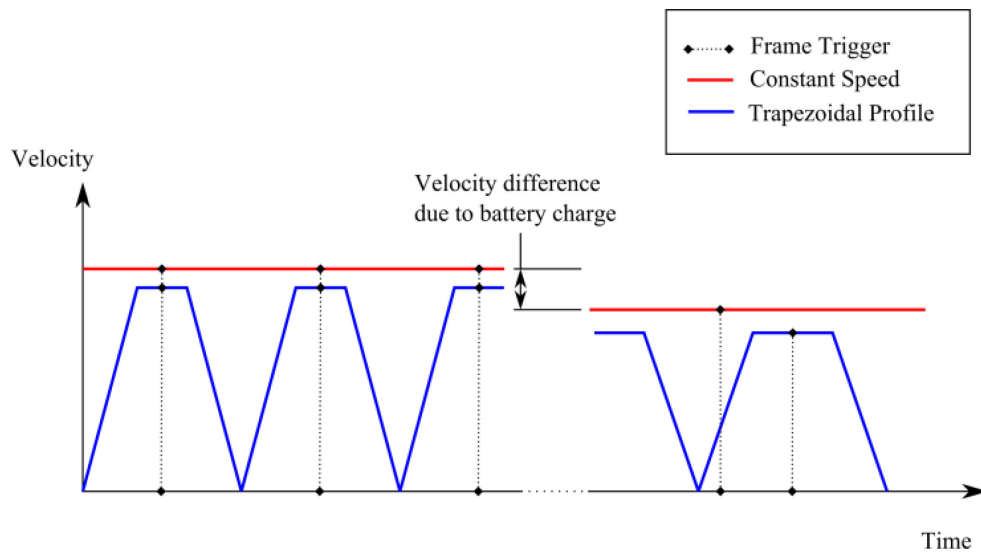
Figure 21: Left: Trapezoidal velocity profile compared with constant speed for stepper motor actuation.

59

3.4.1.4 Mounting Design

The camera mount was constructed from lightweight materials. The baseplate and aircraft mounting assemblies were machined from aluminum and allowed for 30 - 45 degree sensor angle, θ_{sensor} adjustment. The camera and filter wheel components were mounted with vibration damping material in compression. The baseplate was affixed to the airframe under the CG and the APM autopilot. The mount was first constructed as 3-D solid models to determine placement, weight balance, and where additional reinforcement was required on the airframe. The Sig Rascal 110 3-D model was the same one used for Hardware in the Loop (HIL) simulations in FlightGear (2013). The CG on this airframe was calculated from research on the gas-powered Rascal 110 by (Jodeh, 2006). Figure 22 depicts the location of the CG on the Sig Rascal 110, and the components that were added to the model with respect to the thrust line, shown as a blue line, and the center of lift, shown as the red line. A fixed body camera allowed for easier modeling of the sensor aim point, because the camera frame is subject to similar rotations and translations as the autopilot, which outputs telemetry data. The models were produced during the Detailed Design Phase to accurately predict weight and size of the payload, and to plan reinforcements to the Rascal 110 fuselage. Figure 23 shows the detailed model of the MSI assembly. Figure 24 shows the model of the entire airframe with sensor range of adjustment.

60
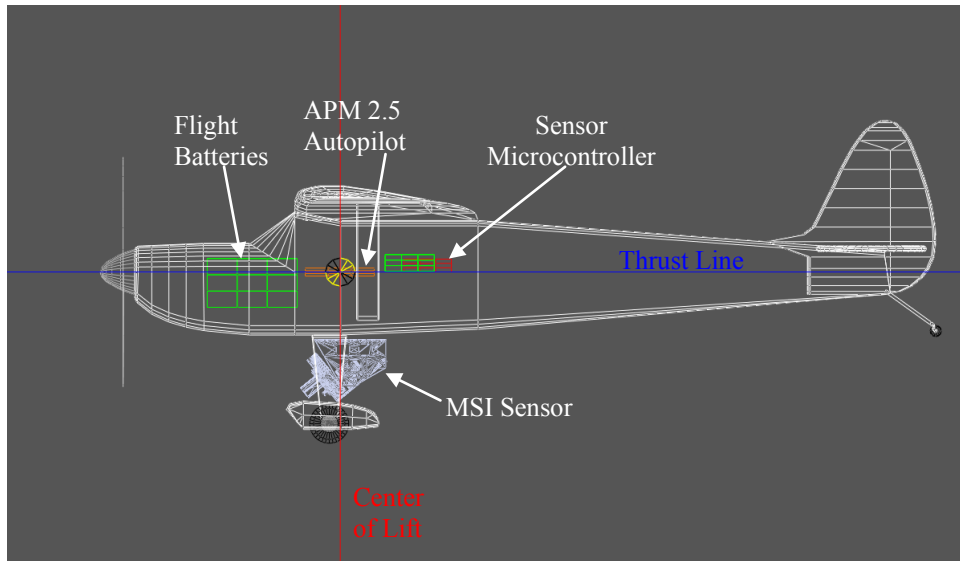
Figure 22: Location of MSI sensor components relative to the CG, which is located near the intersection of

the thrust-line and Center of Lift of the Sig Rascal 110.
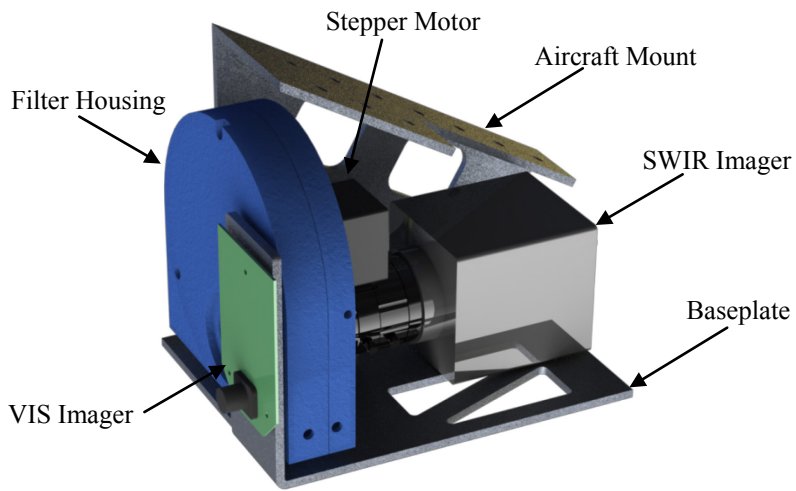
Figure 23: MSI Sensor assembly
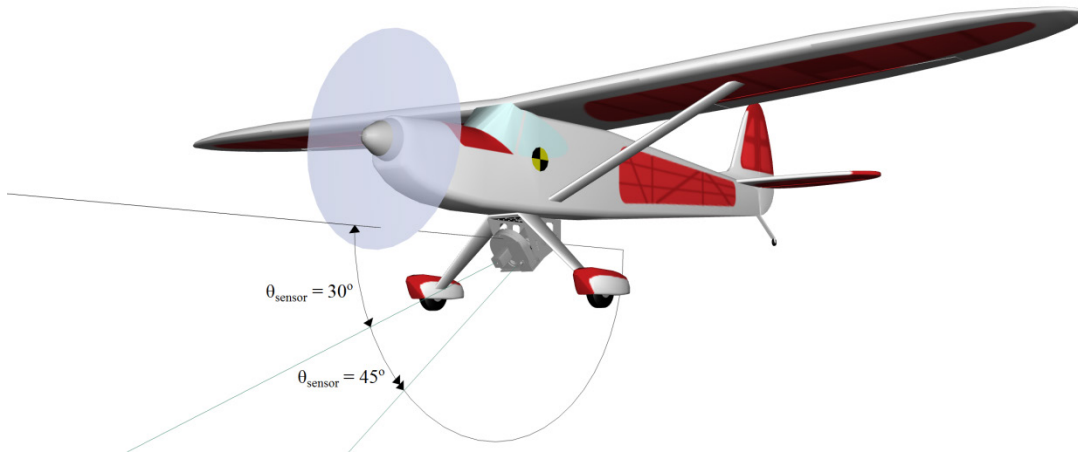
Figure 24: 3-D Model of camera assembly onboard Sig Rascal 110 a ray depicts the sensor angle degrees of movement. The mount is adjustable from 30-45 degrees of declination.
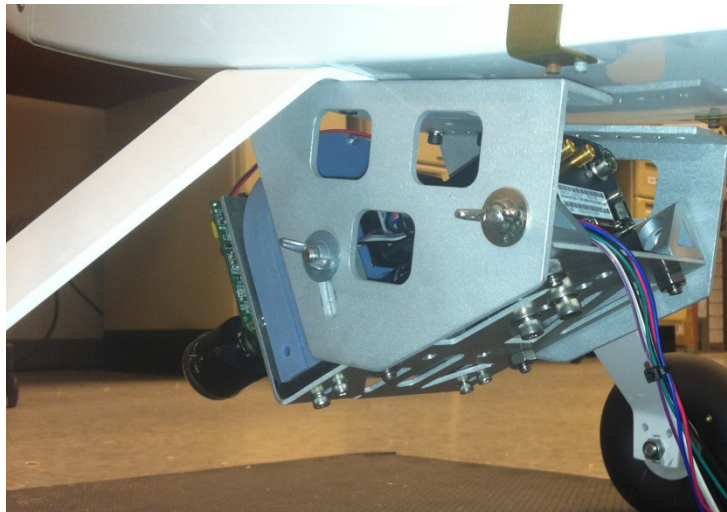
Figure 25: MSI sensor mounted to the airframe.

Figure 26: Test Sig Rascal 110 airframe and sensor payload

3.4.2 Stereo calibration

Before detections from both cameras could be fused, the cameras both required calibration, to compute the intrinsic and extrinsic parameters. A camera calibration toolbox from (Bouguet, 2013) was used to solve for the camera matrices K_L, K_R, the rotation vector, R, and Translation vector, T. Corner detection was used to estimate the fundamental matrix. By taking video with both cameras running at once, the spatial relationship between them was determined. Figure 27 displays the extrinsic parameters of the cameras, and how they spatially relate to the calibration checkerboard grids 1-10. The left and right cameras existed on different planes in all axes, and registration of their images required knowledge of a projective transformation matrix. The camera calibration outputted the rotation matrix, R, and translation vector, T, which are factors of the projective geometry between the two cameras.
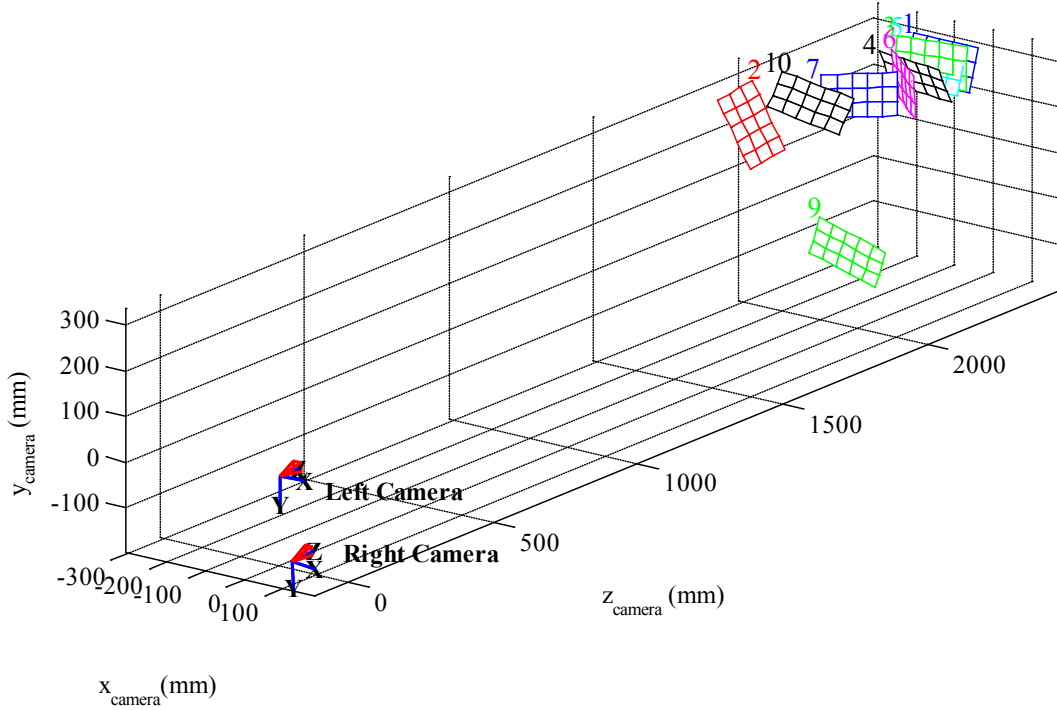
Figure 27: The extrinsic parameters of the two camera setup is shown. The checkerboards that were used for calibration depicted by the colored grids numbered 1-10. Note that they are not coplanar in any axis.

3.4.3 Image Transformation and Registration

If the point in space is known approximately, the projective transformation can be obtained to register images from stereo cameras. First, the points in relation to the right camera and the target image plane, x_i, y_i, z_i are needed. These points are output from the function `footprint()`by (Welborn, 2013). Next, these points are output with an algorithm from (Mariottini & Prattichizzo, 2005) shown by (Eq. 28) .

$$U_R = \begin{bmatrix} x_i & y_i & z_i & 1 \end{bmatrix}^T \qquad\qquad (\text{Eq. 27})$$

$$\begin{bmatrix} u_i \\ v_i \end{bmatrix} = K \begin{bmatrix} R^T \| T \end{bmatrix} U_R \qquad\qquad (\text{Eq. 28})$$

64

Where:

x_i, y_i, z_i = Spatial location of image corners and (i=1,2,3,4) with respect to the right camera frame.

After the points corresponding to the projective transform are found, a transform was created with the MATLAB function, `Tform=fitGeoTransform(U, X,` `'Projective')`. Where `X` is a 4x2 matrix from the new corners u_i, and v_i with i=[1,2,3,4] and `U` is the 4x2 matrix of untransformed corners on the left camera. Next, the transform is applied to an image with the MATLAB function

`imageTform=imwarp(Image,Tform,Rref)`.

Figure 28: Results of projective transform registration using SIFT and RANSAC. Shows the stereo disparity of the two cameras. RGB is red image, and SWIR is represented by green image. Note that disparity is only minimal at one location, the dismount, whereas disparity increases with greater distance.

Since the cameras were not perfectly aligned in 3-D space, the distortion changes for different target ranges. This fact can be accounted for, given the distance to the

65

dismount is known. Solving for slant distance, z, by geometry of camera position using

(Eq. 3), the projective transformation matrix for the left camera can be determined.

3.4.4 Epipolar Geometry

Since the rotation vector is not zero, and the translation vector is greater than zero

in more than one plane, the epipolar geometry resembled a model more similar to the

non-parallel stereo model. This model is still valid for determining registration offset

with two cameras, however the epipolar lines may no longer be orthogonal to the y axis.

The results of this are shown by the stereo rectified images from camera calibration in

Figure 29.
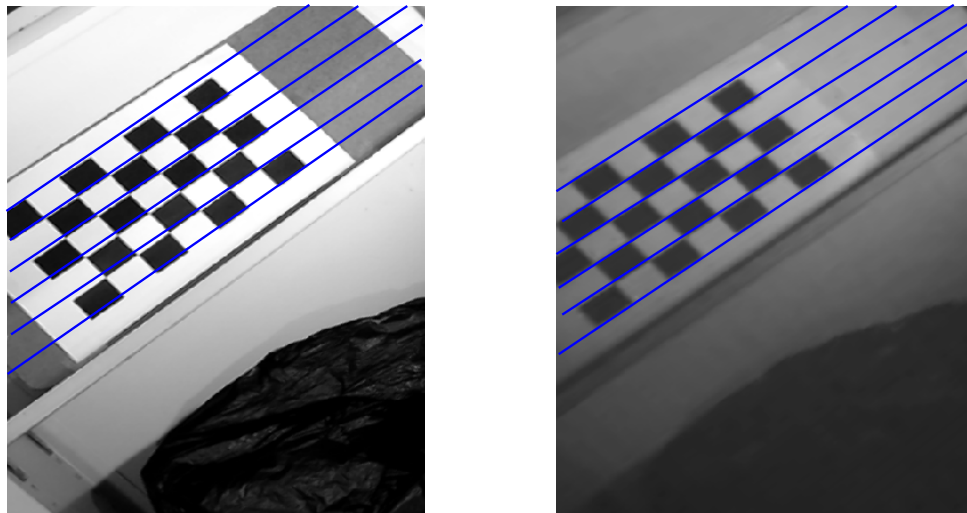
Figure 29: Left, VIS camera calibration image. Right, SWIR Camera calibration image. Epipolar lines
depicted in blue, show the geometric relationship between the two cameras after stereo rectification.

3.4.5 Reflectance Conversion

Before applying the dismount detection algorithm, raw pixel values were

converted to reflectance. Multiple radiometric correction methods were experimented

with, and trial and error was used to determine the best method. Flat field correction just

66

required one spectrally non-reflecting material, such as a black calibration panel or asphalt. ELM corrections perform best with two or more reference materials (which reflectance is known for), and then applying a linear gain to the raw data. However, the ELM method was less desirable for reasons mentioned in Section 2. In test scenes, white and dark panels were available, and their signatures are shown in Figure 30. During test flights, a few objects with contrasting reflectance were in most frames; concrete, asphalt, runway markings, and clothing all had unique spectral signatures. Their reflectance values were found with a spectral library or the ASD FieldSpecPro 3. Thus, ELM or flat field correction could then be used to account for environmental illumination. ENVI 5.0 was used to apply correction to imagery (Excelis Inc, 2013).
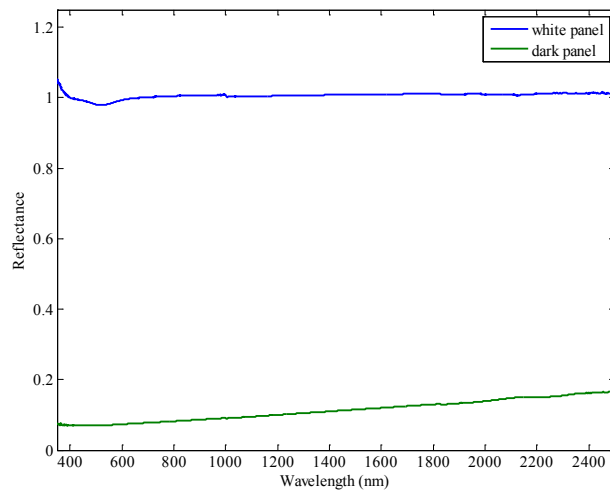
Figure 30: Reflectance values for white and dark Labsphere calibration panels

3.4.6 Video Processing

The algorithm for processing video was unique to the SUAS MSI that was constructed. Since the filter wheel was spinning while the aircraft was moving, the images had to be overlaid to create an image cube. The process is as follows: A frame

67

was captured with the filter in the first position, λ_1. Next, the filter wheel rotates to the

second position, λ_2, and another frame is captured. It was necessary to achieve proper

overlap between the first frame, F_1, and the second frame, F_2, for $i = 1,2...n$. To

spatially align pixels in F_1 and F_2, registration was done using SIFT and RANSAC for

point feature extraction and homography transformation. Figure 31 illustrates the

footprint of frames F_1 to F_n for two wavelengths, λ_1, λ_2. Since the VIS camera has no

filter wheel, the frames were captured at 25 fps for the entire sequence.
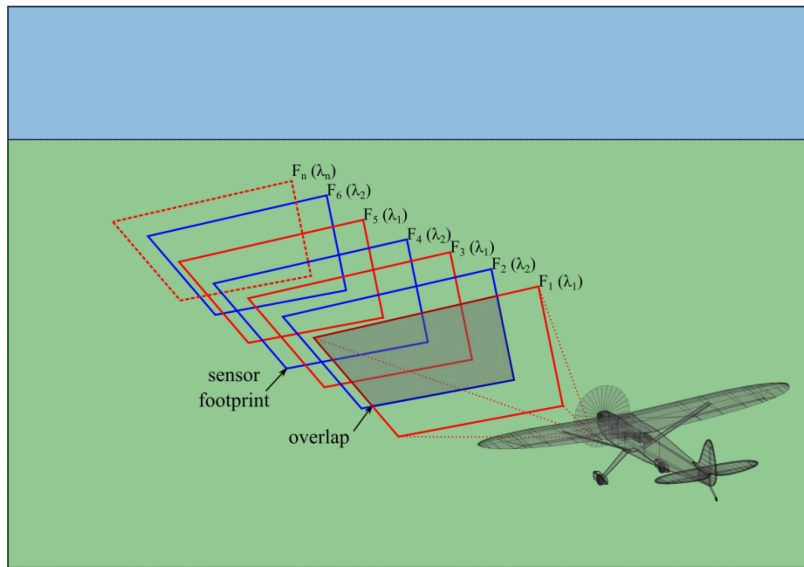
Figure 31: Frame capture sequence for spectral image construction

3.5 Analysis Approach

To measure the effectiveness of the imagery system, qualitative and quantitative

metrics were used.   The ground based HSI was compared to the SUAS MSI, and then

ground data was compared to aerial data. Each metric judged different aspects of the data.

ROC curves for each system quantitatively measure the effectiveness of the detection

algorithm and sensor in detecting skin. IQ metrics judged the amount of distortion and motion blur. Pixel density was calculated for each image to relate each imager despite different lens focal lengths. Airframe effectiveness metrics were used as well, including time on target, gyration rates, and accelerations from a high resolution IMU. Qualitative metrics were used for comparing video quality between test flights, and between imagers. Factors that were qualitatively analyzed included dismount illumination, overall video quality, and visibility.

3.5.1 ROC Comparison Analysis

The detection systems were compared with receiver operating curve (ROC), which displays classification probability over a varying detector threshold. For this analysis, truth labels were generated from the imagery. Next, the detection output, or score, was thresholded for probability of true positive rate versus false positive rate. For the NDSI Algorithm, a single score method was adapted to generate a ROC (Beisley, 2012). Area under the curve (AUC) is a single score that was used to compare each curve. A ROC Curve is an objective metric that compares the sensor, and classification algorithm of two systems.

3.5.2 Dismount Detection Scenario

To recreate an operational environment, the data can be collected from an aerial imager with real time video. To accomplish this task, there must be a synergy of elements. A human will be placed in an outdoor operational environment. The plane will launch from a remote location, and an operator will view data from a ground station. The approximate coordinates of the human were given to the operator, and the operator was

69

tasked with identifying the dismount. After a racetrack pattern was established, fine adjustments were made to the routing path to view the dismount.

3.5.3 Flight Path Planning

A challenge of object detection is collecting enough light off the object with the sensor. This is where planning can be done to consider all aspects of lighting, camera exposure, gain, and pixel density. A unique challenge arises when detecting objects that are small and concealed, given that there is little natural light that arrives from an awkward angle, and the sensor is at a large slant range. Autonomous flight for the research utilized straight and level routes; however wind, lighting, and flight restrictions dictated the autopilot waypoints. Sun angle was especially important for the chosen skin detection algorithm; patterns were flown to maximize flight time with the sun behind the sensor. Test flight telemetry was converted to a Flat Earth Model coordinate system in order to produce 6 DOF data. MATLAB code for extracting the flat earth model from the autopilot is shown in the Appendix. This allowed the flight trajectory, and relative position of the airframe to the ground aim point to be computed. Test flights recorded high resolution attitude and IMU data. Gyrometers measured angular rates, and accelerometers measured acceleration in the three aircraft body frame axes up to 50Hz sampling frequency. The airframe accelerations and rotations were compared with imagery metrics.

3.5.4 Imagery Metrics Applied

Decision making ability was judged by multiple objective metrics. Metrics were applied to the fused imagery after post processing the data. These objective metrics are foundational for comparing the tradeoffs of the ground based system with the SUAS MSI

system. The metrics in Table 1 are known to measure image and data fusion quality. The metrics were applied with MATLAB software for a single frame of video.

3.6 Summary

This chapter covered the experimental procedure and methodology. It explained the aerial testing platform, sensor type and imaging apparatus, measurements for quantifying sensor effectiveness, and comparison technique to answer the research questions.

4. Analysis and Results

4.1 SUAS MSI Ground Testing and Tuning

There will always exist time, budget, and testing availability constraints that limit the scope of the research. For the SUAS MSI, a few issues could have been avoided.

Ground tests revealed that focus was poor at long range in one wavelength. LoCA, as mentioned in section 2, was most likely the cause for poor focus with one wavelength. LoCA required the camera to utilize a mean focus setting between 1050 and 1550nm bandpass filters. Figure 32 depicts a mean focus setting for both bands to minimize LoCA. Vignette is visible in most scenes, and characterized by low pixel values around the edges of the image center. Diagrams of different aberrations and vignette are located in the Appendix. Light bleeding was another issue that occurred from gaps in the optical system; an example is a gap between the lenses and filters. The plastic filter housing without a proper non-reflective coating also caused light bleed. Nunez (2009) sealed the gap between lens and filter, and this was done on the test system as well to block unwanted light during later tests. The filter arrangement performed well, and a relatively constant rate spin with filter wheel was achieved by using fresh batteries for the motor driver. Digital artifacts were present in the video. Sato (2006), notes that digital artifacts are often created by the Analog to Digital Convertor (ADC) if sampled at too low of a rate, and they can be seen in smooth tonal areas.

Figure 32: Left, 1050nm image, Right, 1550nm image. Focus is at a mean setting. Note the car in background between the filter change (Filtering speed was 0.50 seconds/filter change).

Applying the d_{NDSI} algorithm required scaling and registration of the image planes. Since the cameras were mounted separately, and they were of different resolutions, the registration had to account for the intrinsic and extrinsic camera properties.

4.2 Ground Imager Comparison

4.2.1 Line Scan HSI Ground Test

The SpecTIR HSI uses digital frame grabber to store 12 bit information for each band (SpecIM, 2013). This improves upon the 8 bit compression from the ADC used by the SUAS MSI. The SpecTIR benefits from a simple registration alignment and closer to a parallel stereo arrangement as displayed in Figure 6; the only offset in the x axis is required for registration of the VIS and SWIR bands. Results from the d_{NDSI} and MF in follow in Figure 33 through Figure 35 for the SpecTIR MSI. Figure 36 through Figure 38 show results from the SUAS MSI. The same bands were used for both imagers for a relevant comparison.

73
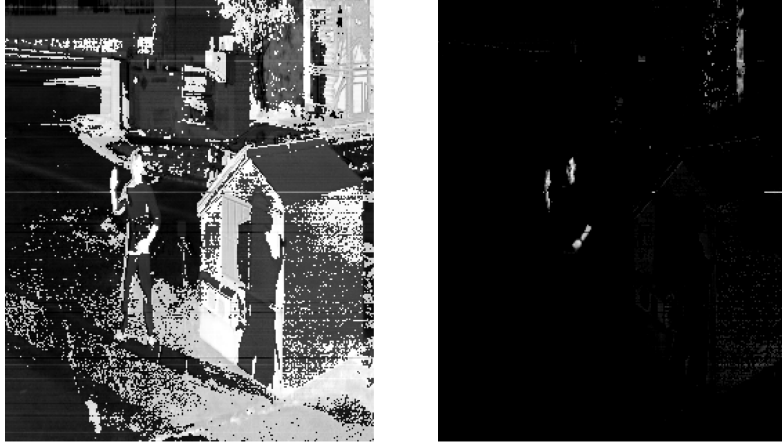
Figure 33: SpecTIR 10m range image. Left, d_{NDSI} detection score. Right, d_{NDSI} with threshold
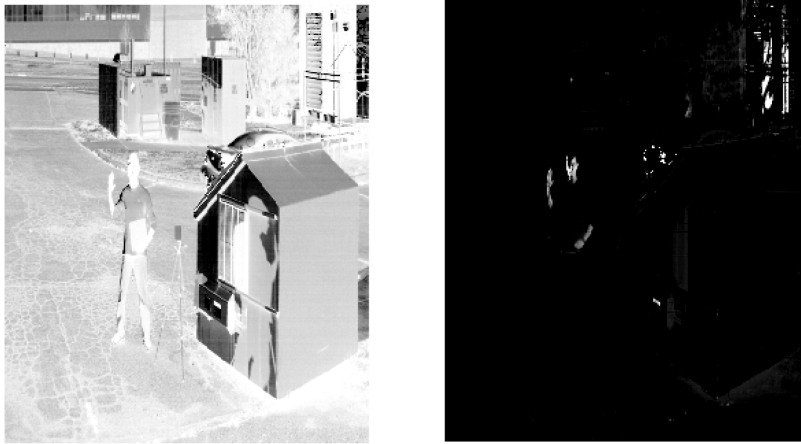
Figure 34: SpecTIR 10m range image. Left, MF detection algorithm score. Right, MF with threshold.
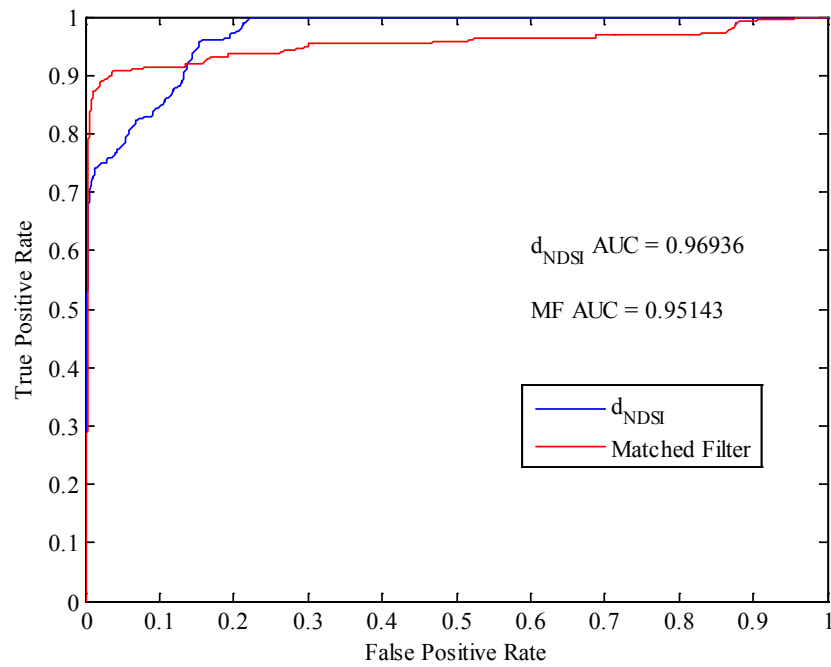
Figure 35: SpecTIR ROC Curves for two skin detection algorithms. ROC for d_{NDSI} is plotted as blue. The matched filter only using 4 out of 363 available bands produced the result in red. These detections produced $AUC_{dNDSI} = 0.9694$, $AUC_{MF} = 0.9478$.
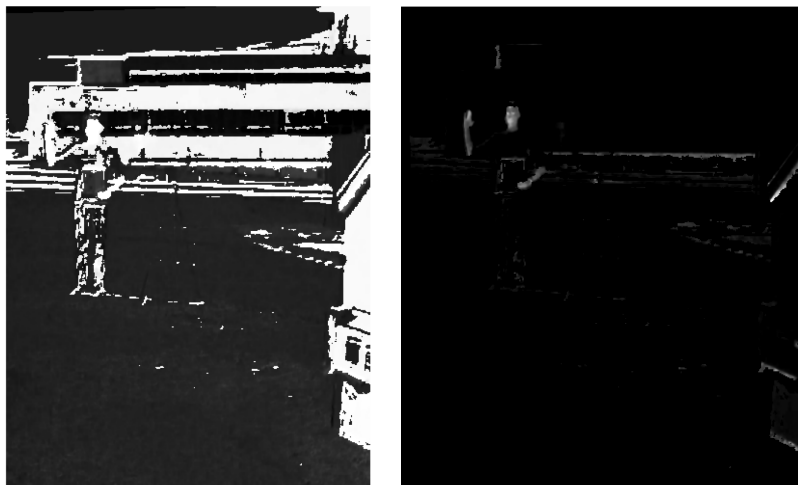
Figure 36: SUAS MSI detections. Left, d_{NDSI} score. d_{NDSI} with threshold.
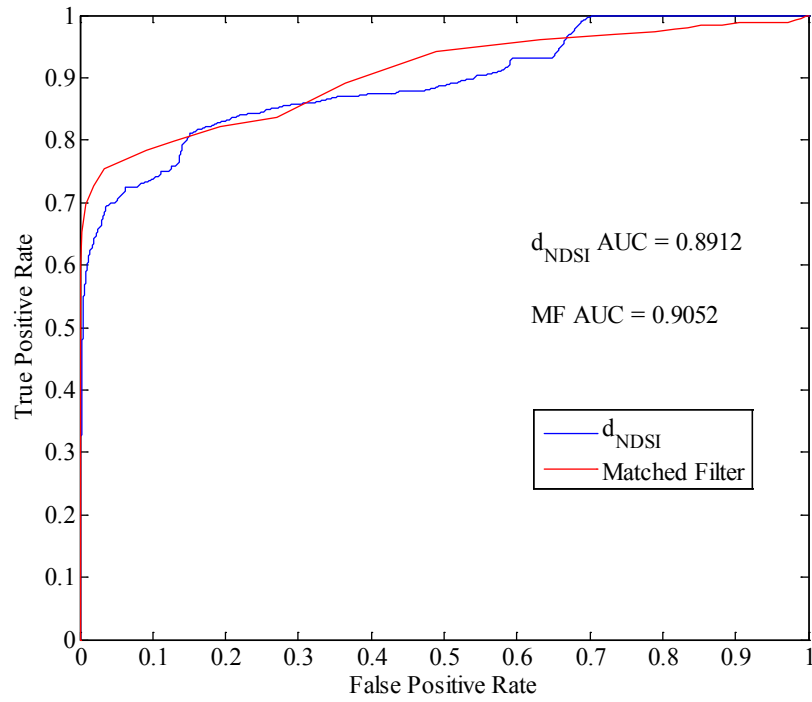
Figure 37: SUAS MSI Camera ROC Curves for two skin detection algorithms. ROC for d_{NDSI} is plotted as

blue. ROC for MF using 4 bands is plotted in red. These detections produced AUC_{dNDSI} =0.8912,

AUC_{MF}=0.9052.

Figure 38: SUAS MSI MF detection with binary threshold applied

The ground test dismount scenario compared the ground based HSI and SUAS MSI at similar GSD. The NIIRS score was calculated using the method described in section 2 and similar values were obtained for each imager due to the large weighting of GSD. The CPBD score was near 1.00 for both which meant that blur was minimal, and this was logically valid for stationary imagers and dismounts. For skin detections, the HSI consistently obtained greater AUC values compared to the SUAS MSI. As mentioned in the research, this may be attributed to registration errors, optical transmission, aberrations, digital resolution, or exposure settings. With all these issues considered, the SUAS MSI performed well given its significantly lower cost. A summary of the skin detection platforms' parameters and results are given in

Table 4.

Table 4: Sensor Comparison

Parameter	Ground Based HSI	SUAS MSI
Specifications		
Focal Length	18.5-22.5 mm	35mm
FOV(vertical)	32°	26°
Spectral Bands	363[4]	4
Design	Line Scanning	Filter Wheel
Range (5.0 cm pixel)	50 m	71 m
Frame Collection Rate	60 Hz	0.5 Hz
Digital Resolution	12-bit	8-bit
Mass	>15kg	1 kg
Performance		
NIIRS / GIQE (60 m)	8.15	8.70 (PD = 6.53%)[5]
CPBD	0.983	0.999 (PD = 1.75%)
d_{NDSI} AUC[6]	0.974	0.912 (PD = 6.55%)*
MF AUC[7]	0.972	0.937 (PD = 3.67%)*

---

[4] Only the same 4 bands as the SUAS MSI were used for detections
[5] PD: Percent (%) Difference, * indicates statistical significance (p-value ≤ 0.05)
[6] Averaged over a sample size of n=3 images, SUAS MSI: σ_{dNDSI} = 0.0200, Ground: σ_{dNDSI} = 0.0143
[7] Averaged over a sample size of n=3 images, SUAS MSI: σ_{MF} = 0.0208, Ground: σ_{MF} = 0.0245
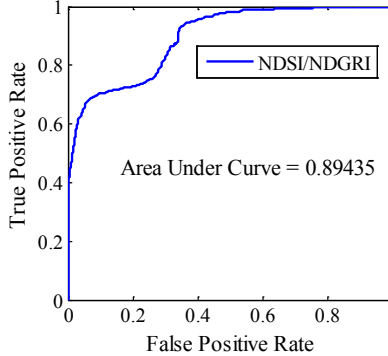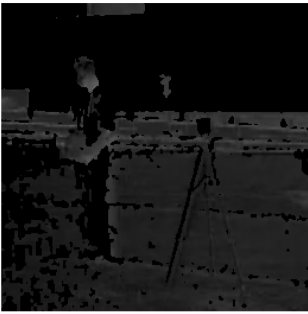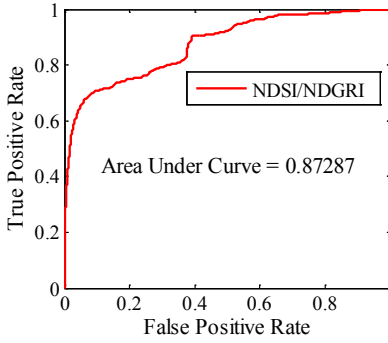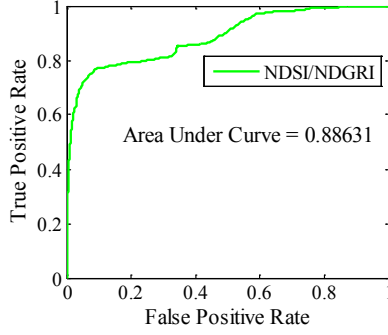
4.2.2 Lighting Angular Effects

Lighting was predicted to play an important role in detection ability. Adequate lighting was maintained in most tests, and camera gain and exposure settings were adjusted to optimize IQ. One can refer to Figure 11, where α was defined as sun zenith, θ_i was defined as incident angle of the dismount, and θ_d was defined as the viewing angle in relation to the dismount surface normal. Different lighting angles, θ_i, θ_d were tested at a constant α to characterize the effect of lighting angle. The d_{NDSI} classification algorithm was used for all detections. Ground testing results from ROC inspection and AUC indicate *no significant impact* due to lighting angles. However, the ground testing environment was subject to less lighting extremes than the aerial environment.

Table 5: Lighting angle effect on detections

Lighting Angle	d_{NDSI} Detection	ROC Curve
$\theta_i = 0°$ $\theta_d = 90°$ $\alpha = -21°$		Area Under Curve = 0.89435
$\theta_i = 0°$ $\theta_d = 45°$ $\alpha = -21°$		Area Under Curve = 0.87287
$\theta_i = 0°$ $\theta_d = 30°$ $\alpha = -21°$		Area Under Curve = 0.88631

4.2.3 SUAS MSI Video Processing

The initial settings were maintained, and the filter was set to change at equal intervals. An image sequence was filmed of a moving dismount, and a Simulink program processed footage and applied the NDSI algorithm. The processing program automatically used the rotation rate of the filter wheel to trigger frames when the filter

wheel was positioned correctly. Figure 39 shows the moving arms of the dismount, and how the algorithm did not update until the next filter exchange. Therefore, the slow filter rate equates to a decrease in viewing rate. Compared to the AFIT monocular system, this SUAS MSI system displays near the same frames per second, however, it performs best with a stationary target. This is because frames from each wavelength are acquired in succession, rather than at the same instant. Another difference with the monocular system, which utilized two cameras, was the amount of aberration. Each camera on the monocular system had separate filters for 1050nm, and 1550nm, could be adjusted separately, and had a fore optic with maximum aperture; this allowed for less vignette, chromatic, and spherical aberration in images. More images of the optics effects are included in the Appendix.

Figure 39: Video Sequence after post processing and NDSI algorithm applied. Filter rate was 1.00 sec/per filter change. Test subject is waving arms and false detection is visible when arms move. Vegetation is visible due to water absorption characteristics shared with skin.

4.2.4 Flight Test Results

Figure 40: Sig Rascal 110 in flying configuration with MSI sensor payload

Flight testing was performed to determine MOEs for the operational configuration. Aerial Imagery collection for the SUAS MSI revealed many challenges with dismount detection, but it also provided an environment to test possible solutions. Camera parameters including auto-gain skewed pixel values could not be used with the SUAS MSI system. For the SWIR camera, the auto-gain recalculated at a maximum 10Hz, and successive filter changes caused auto-gain to change Operational (OPR) settings on the camera. Each OPR setting had a unique gain, exposure, and gamma level that was optimized for a specific level of environment illumination. This resulted in over saturated, or under saturated images when filters were alternated. Therefore, this setting had to be deactivated for proper data acquisition. Longer exposure times were required during the morning, and shorter times were required midday. However, changing these settings without auto-gain was inconvenient during testing.

Setting camera parameters on the SWIR is accomplished with EIA-232 serial port, and testing was done to establish wireless communication with the microcontroller. In flight testing, it also posed a challenged to achieve the proper setting. The image sensor may come in direct line of sight with the sun. The camera had a failsafe to cut power when the scene becomes too saturated, and this protects the camera in direct sunlight. Nevertheless, this would pose a problem for any aerial detection scenario that has varying sky conditions. Testing showed that midday detections were higher quality; the solar zenith angle was smallest, and environment illumination was more uniform. Detections during peak zenith were better with lower OPR settings; however, later in the day, higher OPR settings were used to compensate for uneven ground illumination. Real time imagery collection requires the ability to change camera parameters "on the fly". On the aerial detection system, it was observed that overexposure and underexposure in a moving environment significantly decreased IQ.

Reflectance conversion for flight test video was done using Flat Field correction with good accuracy. If this method cannot be performed, illumination invariant reflectance conversion methods have been the best option for the SUAS MSI. For real time processing of imagery, RT code methods would be optimal and not require calibration panels for Flat Field or ELM (Beisley, 2012). These methods depend on the solar zenith, angle vector of the camera with respect to the sun, time of day, and atmospheric conditions all which are widely available.

Long slant range, and high illumination environments require additional optical considerations. Lens selection resulted in the proper focal distance, but improper sensor format for the SWIR. For aerial application, size and weight was key; for this reason, the

fixed focal length lens was used. This lens was significantly smaller than the OEM Nikon 50mm f/1.4 F-mount lens; moreover, the sensor size supported by the compact lens was not well matched to the Goodrich SWIR. Nevertheless, vignette would still occur due to the bandpass filter diameters that were available. For these reasons, Region of Interest (ROI) windowing of the images was required for video. An auto adjusting aperture, and optics designed for the $25\mu m$ focal plane array would increase sharpness and reduce distortion but they still would not focus images for both bands; this can be attributed to aberrations such as LoCA in the refractive fixed focal length lens. The best solution would utilize a reflecting lens, because a reflecting optic is indifferent to refraction index of the material.

4.2.5 Waypoint Navigation
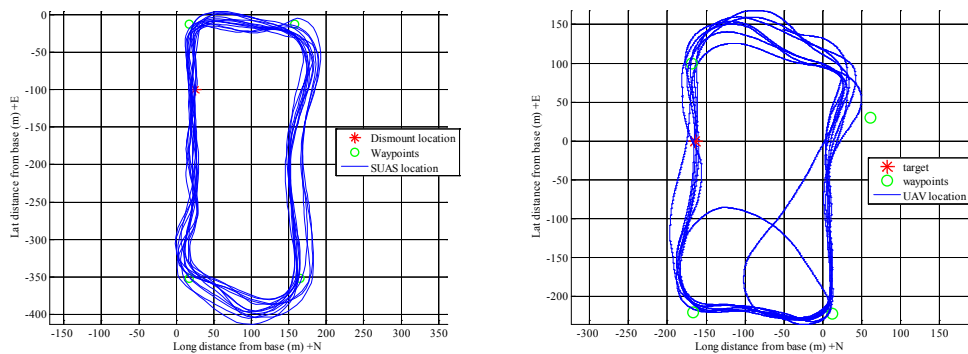
Figure 41: Left, August flight test pattern for initial gain tuning. Right, October Flight Test Pattern for Imagery Collection

Weather conditions affected test results and significantly more wind was encountered during imager collection than gain tuning. These conditions accounted for deviations from the intended waypoint locations. The deviations of the test flight pattern can be compared to the gain tuning test pattern with Figure 41.

Battery power was considered as a limiting factor for flight time. Having sufficient battery power for the operational demo was dependent on wind speed and battery degradation. Flight tests were scheduled for 15 minutes duration, and could be increased by adding larger batteries. These limits are less than the 1 hour flight time proposed in the conceptual system design. This time limitation may impact dismount detection in remote areas that do not have access to chargers, or spare batteries. The flight time limits were likely reached earlier than anticipated due to high winds and required further planning to optimize testing time.

4.2.6 Flight Video Processing

Faster filtering rates were needed to minimize stereoscopic effect of images. Having two images taken from a large distance apart, creates a stereo vision effect on 3-D objects. This effect was noticed with registration of images, and it hindered registration performance of the first test flights with 1.0 fps. The next flight test increased the filtering rate to 2.0 fps, and this decreased the time between images. It improved registration performance, and it also decreased effects of the resultant wind. Figure 42 shows a sample flight pattern used for data collection. Figure 43 shows variations in working distance and pixel size of the MSI imager for a segment of the flight pattern.
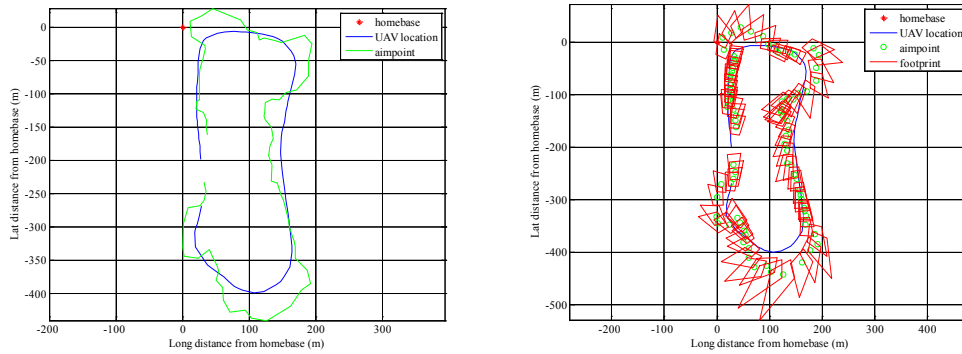
Figure 42: A sample flight pattern is shown in blue on both images. Left, the sensor aimpoint is shown in green. Right, the sensor FOV is projected on the ground is shown in red.
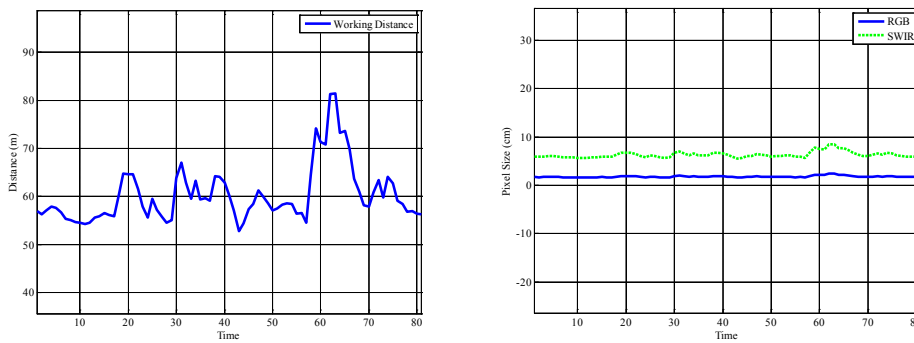
Figure 43: The sample pattern is analyzed. Left, variation in sensor working distance is plotted as a function of time. Right, pixel size is shown as a function of time.

Feature detection with SIFT and RANSAC was applied to the imagery to register frames. Using feature detection technique with SWIR images alone was difficult. This is because each successive frame displayed data from a different wavelength. Furthermore, feature detection with vision based methods alone was difficult for areas such as a runway or forest, with very few intensity based landmarks. Even at the 2 fps filtering

rate, there was usually significant movement between each frame, which caused some projective transforms to stretch to near infinity. Limiting the video data collection window to straight line flight paths reduced most of the invalid transforms. A 3-D view of sensor aim geolocation results using autopilot telemetry is depicted in Figure 44. The resulting projective transform of a video sequence using autopilot telemetry is depicted in Figure 46.
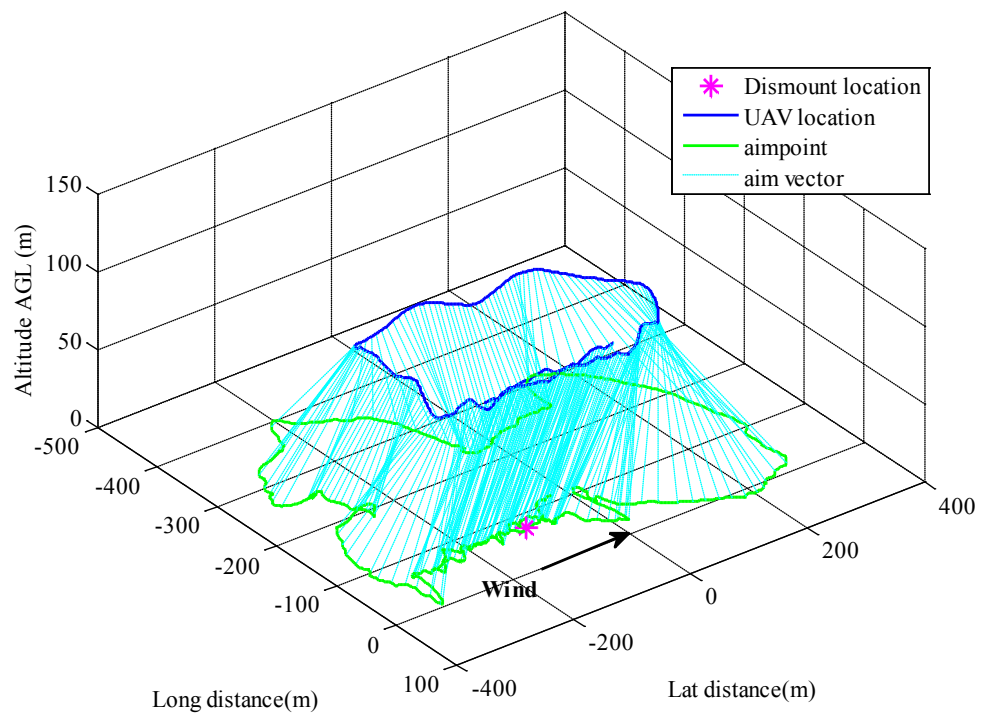
Figure 44: Test Data with sensor aim vector plotted as blue dotted lines
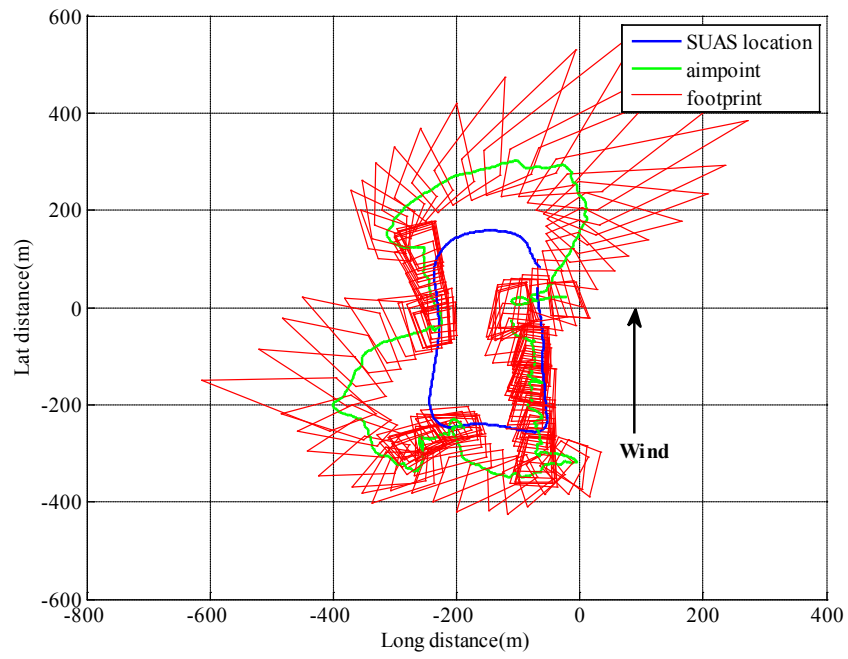
Figure 45: Test Data with projective transform plotted as red lines
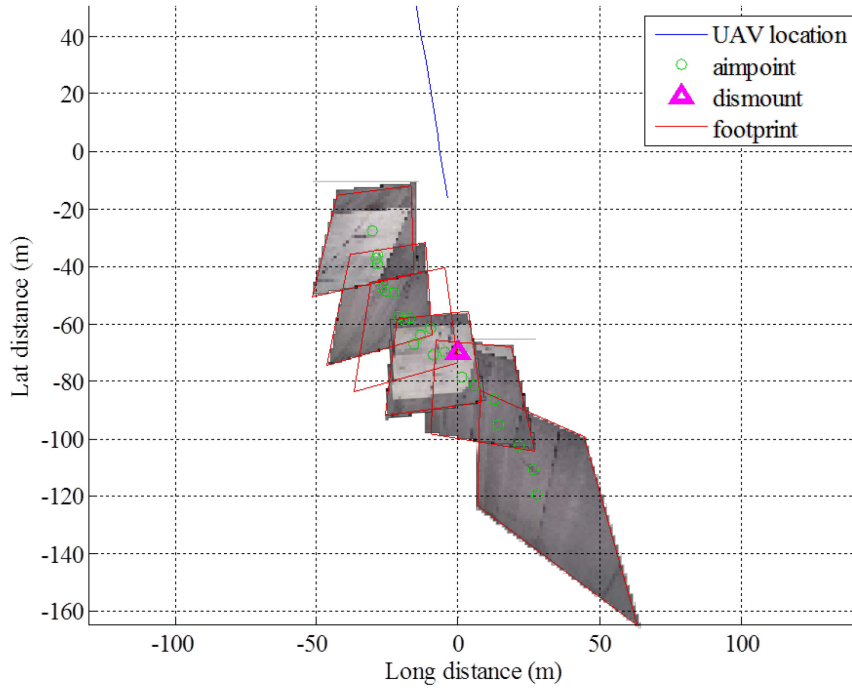
Figure 46: Projective transformation of a video sequence from autopilot telemetry

87

The VIS camera, collecting at 30 fps, showed significant interlacing blur due to motion and vibrations from the motor, and wind in the air. Figure 47 quantifies the motion blur with the CPBD IQ metric for the upwind and downwind portions of flight video. Higher CPBD occurred during the steady upwind portion of the pattern, while entering turn and downwind decreased the CPBD. Turns and downwind flight caused higher movement rates in the longitudinal axis (roll) and normal axis (yaw) relative to the aircraft body frame. Figure 48 shows average angular movement rates for each portion of the flight pattern. Low CPBD was indicated by blur and distortion in the imagery. Blur interfered with image registration for the vision based methods.
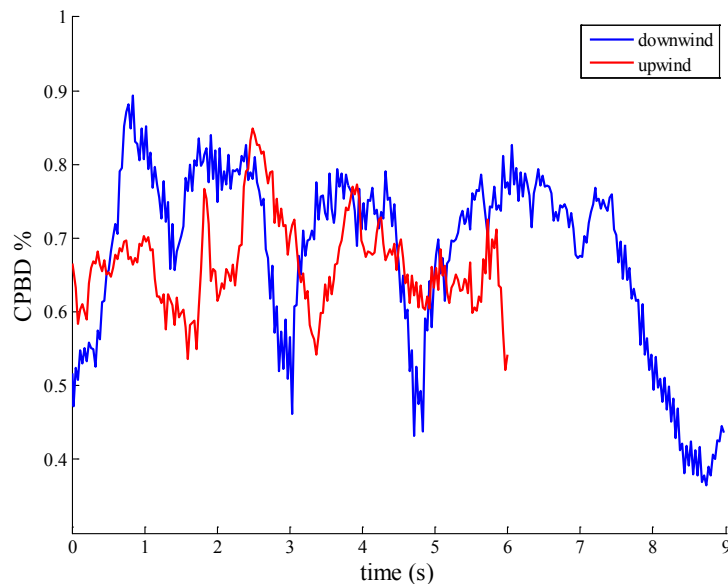
Figure 47: Cumulative Probability of Blur Detection (CPBD) is plotted over time for upwind and downwind portions of the flight pattern. The upwind run had a higher overall CPBD, and averaged 71.6%. Downwind run averaged 66.5% CPBD value. A larger % value of CPBD indicates less blur.
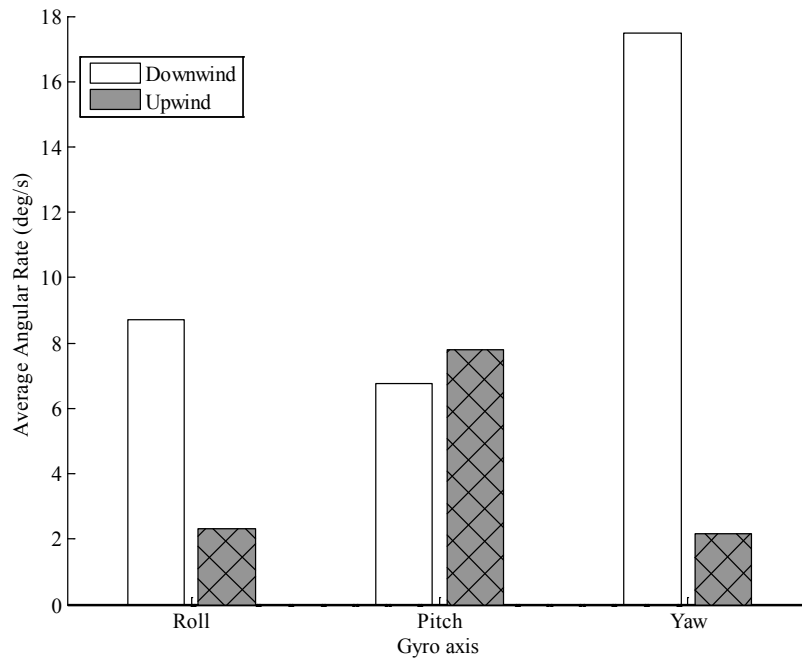
Figure 48: Comparison of the test patterns roll, pitch, and yaw rates averaged for 10 upwind and 10 downwind runs.
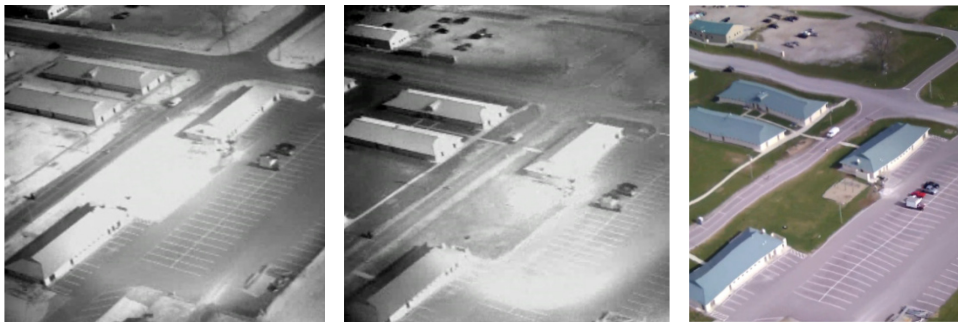
Figure 49: Background images from flight data. Left, 1050nm. Middle, 1550nm. Right, VIS.

Vibrations greatly affected video quality. Video collection from the SUAS proved effective, but faced blur and distortion during wind turbulence and high throttle maneuvers. Figure 49 shows significant blur on SUAS MSI imagery, and this is indicated by waves most visible in the right, colored image. Feature tracking

89

performance was degraded with the blur but the SIFT and RANSAC still proved robust in image registration.

Figure 50: SWIR test flight imagery with feature point matching applied for projective transformations and image registration. Top left, first 1050nm frame with feature matches indicated by the colored points. Top right, original image from next 1050nm frame. Bottom left, first frame with projective transformation applied. Bottom right, second frame with projective transformation applied.

Projective transform calculation with attitude data was possible with methods discussed in section 2, however, application of the algorithms in MATLAB were inefficient. A C++ based platform could utilize attitude and vision feature detection joined by an Extended Kalman Filter (EKF) to estimate a projective transform more efficiently (Beard & McLain, 2012). Feature detection with moving imagery is quick and

90

efficient with the SIFT and RANSAC methods discussed in section 3. Figure 50 shows

results of feature processing for a video sequence in one wavelength. Calculation of the

projective transformations, and registration was done in MATLAB. The process was

repeated for each wavelength to assemble an image cube. Figure 51 through Figure 54

show the step by step process for registering and assembling an image cube.

Figure 51: Left, 1050nm video frame, after projective transformations applied. Right, 1550nm video frames

Figure 52: Point matching between the 1050nm and 1550nm image frames, before final image cube.
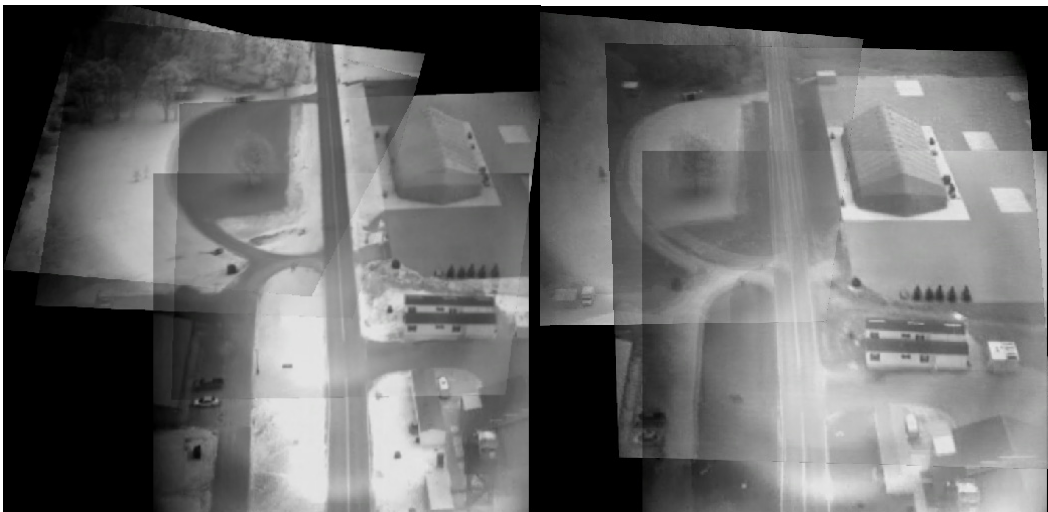
Figure 53: Registered video sequence of 1050nm using SIFT, RANSAC, and homography transformation
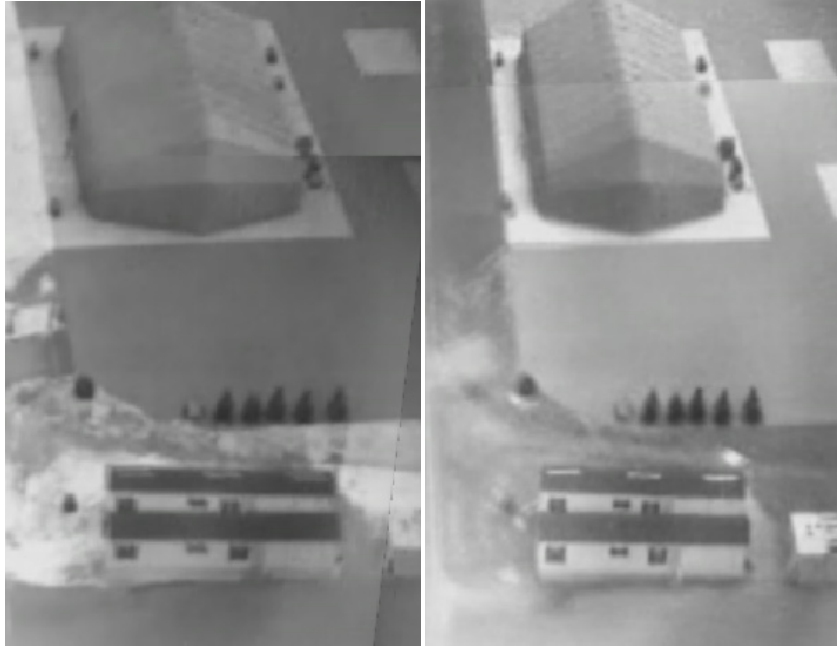
Figure 54: Left, 1050nm image. Right, 1550nm image
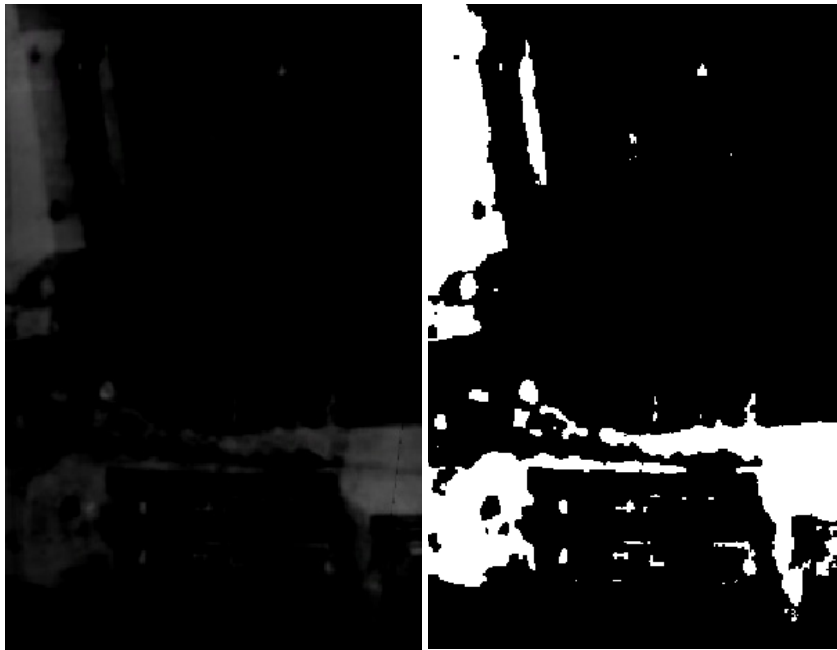
Figure 55: Left, NDSI algorithm applied to the aerial image sequence. Right, threshold image, where white

area denotes vegetation or skin

The NDSI algorithm also is able to detect vegetation. Figure 55 shows an aerial scene with the detection algorithm applied. Using more bands can reduce false alarm on unwanted material. Robust skin detection involves applying a rules based algorithm with the NDSI and NDGRI to achieve detection. However, with these results, we infer that such an algorithm can detect skin with a relatively high probability.

Figure 56: SUAS MSI fight test detection example. Left, MF score from VIS Bands. Middle, MF score thresholded. Right, ROC Curve with resulting AUC = 0.9118

Flight test detections were on average less accurate than the ground test results, due to focus, vibration, and registration error. However, multiple detections gave high AUC values. This may be attributed to the low background noise from an airstrip scene, because there were less buildings and obstructions. Figure 56 shows a detection result with the MF at approximately 20m slant distance. The results prove that aerial dismount detection is feasible with the proposed equipment.

4.3 Chapter Overview

This chapter gave the results from ground testing, flight testing, and analysis of data for this thesis. The flight expedient prototype system was compared to a proven ground based imager, and issues faced for the MSI onboard an SUAS were revealed from

flight testing. Proposed refinements to the prototype requirements were explained for the system.

4.4 Investigative Questions Answered

1. Is MSI effective for dismount detection on an SUAS?

    - The literature and results explain how aerial imagery can improve the ability to distinguish skin from background.

    - It was demonstrated that aerial dismount detection exhibited AUC values as high as 0.91, which indicates a reasonable effectiveness.

2. What type of MSI system is needed for an aerial platform?

    - The original operation requirements outlined a possible solution for dismount detection from an SUAS; however, refinements to the proposed solution were noted including:

        o High frame rate by using faster filter change speeds or a patterned filter array;

        o Refractive optics;

        o Automatic gain and exposure adjustment;

        o Kalman filtering for image registration.

    - Improvements to the design would increase the utility of the system for minimal additional cost.

3. Which camera parameters make aerial dismount detection a challenge?

    - There were problems encountered due to sun angle. This was noted during flight testing, and waypoint planning considered the location at of sunlight in relation to the MSI sensor.

    - Modifying gains in the field was cumbersome, and wireless serial communication to the camera system would improve detection effectiveness.

    - A fixed body sensor was chosen for cost and weight, but a gimbaled sensor, even in one axis, would be useful for improving IQ.

- Frame capture speed affected image blur, feature matching, and registration. Having a slightly higher frame rate, by increasing filtering speed, provide some improvement during testing.

4. What metrics are best to compare dismount detection ability?

- NIIRS values were higher on the SUAS MSI by a percent difference of 6.53 %. However, NIIRS was largely a function of GSD or pixel size rather than spectral properties.

- On the ground, CPBD exhibited a higher performance by the SUAS MSI percent difference of 1.745 % between imagers. The small difference in CPBD on the ground simply validated the assumption that the imagers exhibited negligible blur on the ground. In the air, CPBD varied as high as 33.41 % compared to non-moving imagery for a pattern speed of 12m/s and altitude of 100ft.

- ROC AUC values were higher on the ground based imager by 6.553% for the d_{NDSI} detector, and 3.672% for the MF detector. The difference in detection capability was small using subjective analysis. However, AUC Values were higher for the ground based imager compared to the SUAS MSI with statistical significance ($p \leq 0.05$).

5. Conclusions and Recommendations

5.1 Chapter Overview

This chapter outlines the conclusions of the research. It explains the difficulties associated with skin detection on an SUAS with the proposed MSI platform, and reasons for those difficulties. Also, it recommends avenues for future research.

5.2 Conclusions of Research

The literature and results both show that Spectral imaging with a SUAS is difficult due to cost, computation, communications, and environmental forces on small sized airframes. Nevertheless, the SUAS MSI exhibited dismount detection performance comparable to a larger, more capable sensor with only a 5.112 % difference for ROC AUC values. Refinements to the system can certainly improve its ability to capture, transmit, process data, and yield valuable results for users.

5.2.1 Proposed Modifications

The proposed solution had a few issues that hindered performance, but could have been avoided. The first was using analog output from the SWIR to capture imagery. The NTSC analog to digital conversion process limited video resolution from 512 to 480 vertical pixels, decreased the sampling resolution from 12 bit to 8-bits, and recorded frames between filter changes. Upgrading the system to a digital frame grabber would increase data quality. The second modification addresses communications for video data. Analog transmission did not retain the same level of IQ as the video stored on board because static and noise. Video on the ground station was only usable when the SUAS was line of sight. Digital may enable higher resolution data transmission. The third

97

modification addresses lens selection. The lens selection affected the quality of imagery from both SWIR bands. Due to the separation in wavelength between 1050nm and 1550nm, a non-refractive lens would eliminate longitudinal chromatic aberrations. Also, reflective lenses are more cost effective than refractive lenses made designed for the SWIR bands. The forth modification addresses the filtering system. The current equipment can operate with a filter speed and frame trigger at 30Hz. This would effectively allow more overlap between frames. 3-D spatial transformation from both attitude and vision processing would have also been helpful for accurate registration. Leveraging both highly accurate autopilot capabilities and fast feature detection capabilities of computer vision with Kalman filtering provides opportunity for higher probability of detection. All of these modifications would help improve dismount detections and make an SUAS MSI system practical for deployment.

5.2.2 Flexible Design

The proposed system has the ability to offer SUAS operators a flexible design for dismount detection. A flexible design would allow the system to operate across multiple environments with small modifications. For example, an airframe capable of SAR in austere environments such as thunderstorms forest fires, or high nuclear radiation zones would decrease the likelihood that a failure would occur during SAR operations. A ruggedized platform that can adapt to different environments would increase the capabilities of the system.

Incorporating the spectral imager also adds to the flexible design. For example, the proposed solution can be adapted for any type of object detection. Depending upon which material must be identified, the filters can be exchanged for bandpass filter with

98

different wavelengths or transmission characteristics. Furthermore, more spectral detection algorithms can be applied to the imagery on the ground station to increase the detection accuracy for other materials. The ability to use more spectral bands and detection algorithms can increase the utility of the SUAS MSI for multiple scenarios.

Despite the current setbacks, spectral imaging is still perhaps the best method for identifying dismounts. The ground tests from the SpecTIR LISA demonstrate the accuracy with which a dismount can be accurately detected with only 4 out of 363 available bands. Research by Beisley (2012) has proven that skin detection is augmented by many spectral wavelengths that were not used in this thesis. Different wavelengths or detection algorithms may be required depending on water content in the air or on the dismount, and concurrent research analyzed the performance of skin detection algorithms in an aquatic environment (Chan, 2014). The proposed system presents a flexible design to detect dismounts with relatively inexpensive equipment, and performance comparable to more expensive imagers.

5.3 Significance of Research

SUAS fit a unique niche for HSI platforms that can be useful for object identification. Although dismount detection on an SUAS may be difficult, this research proves that the proper system can make it possible. This research first formed a comprehensive literature review. It discussed the factors related to SUAS and aerial imaging. Next, it explored the factors required in a dismount detection system. Then, processing algorithms and sensor fusion techniques were reviewed. The system was then constructed from bare components, tested, and refined. Furthermore, difficulties of skin

99

detection were documented for future research or exploration. Finally, assessment of the

prototype platform was conducted with objective metrics, and overall system

effectiveness for dismount detection was determined.

5.4 Recommendations for Action

With this research, the reader should identify the three main findings:

- SUAS are valuable sensor platforms and provide valuable information to the user at a reasonable cost. Low cost systems should be pursued for widely available detection platforms.

- SUAS MSI systems should be considered that utilize multiple bands from the electromagnetic spectrums to allow the sensor platform to be used for multiple roles or environments.

- Development of an embedded dismount detection platform should be pursued to decrease processing time. Based on sensor design from this research, using more capable sensors will yield even better results.

5.5 Recommendations for Future Research

This research set the groundwork for aerial skin detection with SUAS; however,

further research can improve the technology readiness level of a detection system.

Specifically, these avenues include:

- Applications of the SUAS dismount detection system to waypoint routing system and autonomous decision making;

- Applying new video technologies to SUAS such as micro-scale HSI that utilize tunable or patterned filter arrays;

- Real time detection processing;

- Pursuing cost effective digital video recording and transmission;

- Onboard SUAS detection processing can be accomplished with embedded microcontrollers.

5.6 Summary

The SUAS Detection System project was conceived with the following objectives:

- Small package form factor;
- Low cost development and deployment;
- Effective and efficient dismount detection.

The project scope covered the entire development process for an airborne dismount detector. The process included researching available airframes, camera and lens technologies, data acquisition and analysis protocols; designing and constructing package components, deploying and operating the system, parsing data and distilling results and recommending system modifications and improvements.

The final mountable package was approximately 15 x 10 x 10cm and less than 1.5 kg to satisfy the size objective. Total cost of the system was more than 1000% less expensive than ground based systems. This fell well within reasonable limits for cost design goals for the system. While highly dependent of environmental conditions, the system was able to achieve reliable and positive dismount detection in each of the tests performed. Ease of use remains a challenge but is easily improved given repetition and refinement of processes. In summary the SUAS Detection System project met all design objectives, and based on suggested improvements and refinements should be considered a candidate for further research, development and use as a valuable tool in visual or ATR dismount detection protocols.

6. Appendix

6.1 Appendix D: Optical Aberrations and Distortion

Optical effects that caused image distortion were encountered, including:

6.1.1 Chromatic Aberration

Chromatic aberration affects an image that includes different wavelengths. It is a result of the differences in refraction through the lens for different wavelengths of light. A diagram of the path of light is shown in Figure 57. While one wavelength may be in focus for a focal distance, another wavelength may require a larger focal distance. This aberration results in one wavelength being out of focus. The effect is depicted on Figure 58 with images collected from different wavelengths, the same focal distance, and the same refractive fore optic constructed from fused silica.
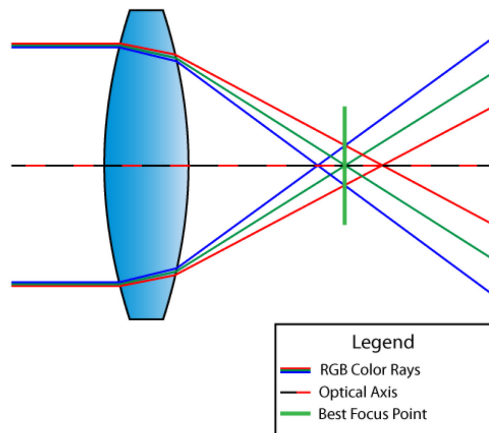
Figure 57: Diagram of chromatic aberration (Mansurov, 2011)

Figure 58: Ground test images. Left is 1050nm in focus, Right is 1550nm out of focus.

6.1.2 Spherical aberration

Spherical aberration affects the light intensity at the focal point. A diagram of this type of aberration is shown on Figure 59. The spherical distortion due to improper lens or too little aperture may be caused from excess light at the image center, or oversaturation. This effect is depicted on imagery in Figure 60.
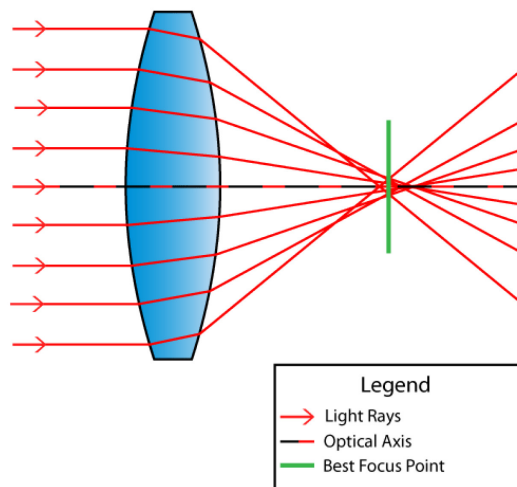
Figure 59: Diagram of spherical aberration (Mansurov, 2011)
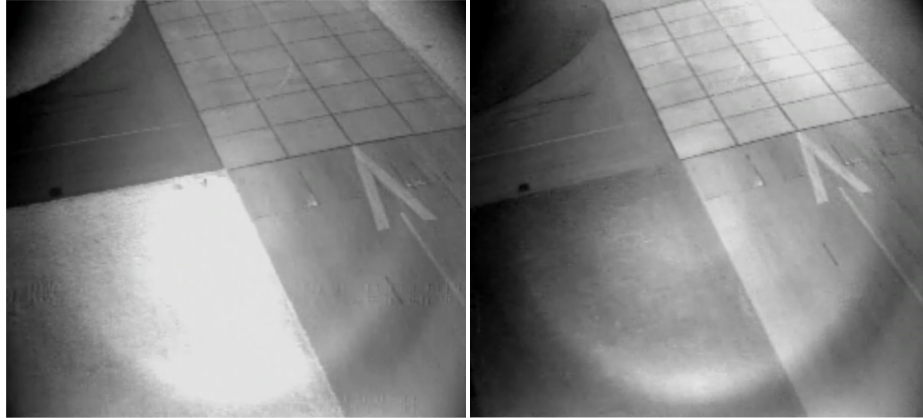
Figure 60: Example of spherical aberration variation. Left: 1050 nm. Right: 1550nm Note less saturation at image center of 1550nm. Light intensity pattern is due to the Airy diffraction for the lens configuration.

6.1.3 Vignette

Vignette affects the outer portions of image plane. Vignette is exhibited by dark regions near image corners. Mechanical vignette is a result of excess distance between the filter and fore optic or undersized filter diameters which limit peripheral light at the image plane. Optical vignette is shown on a diagram in Figure 61, where central light enters at a larger aperture than peripheral light.
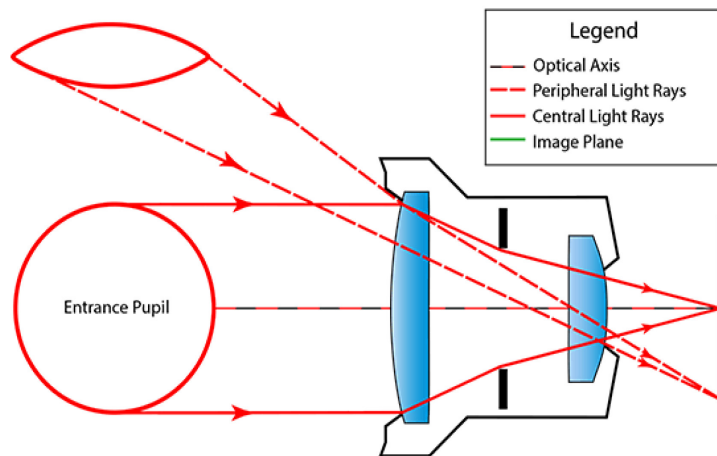
Figure 61: Diagram of optical vignette (Mansurov, 2011)

104

6.2 Appendix B: Sensor Preprocessing Code

6.2.1 flightSensorFovCalc.m

```matlab
function [suasSd, suasVIS, specTir, monoSd]= flightSensorFovCalc(isKnown_wDist)
%flightSensorFovCalc(isKnown_wDist)
%       INPUTS : isKnown_wDist= (0)if wDist is being solved for
%                               (1) if wDist is known and calculations are needed for calibration
%       OUTPUTS :   suasSd = imaging system parameters for SUAS SWIR
%                   suasVIS = imaging system parameters for SUAS VIS
%                   specTir  = imaging system parameters for Ground Based HSI
%                   monoSd   = imaging system parameters from (Peskosky,2010)
%
% Author:  Stephen Sweetnich  AFIT 2013

%% UAS Specific Parameters
velBody = [12 0 0] ; %Velocity, Body Frame [x, y, z] (m/s)
sensorDeg = 30 ; %angle of elevation rel to yz frame(deg)
perInVu = 0.50; %Percentage of horiz FOV to keep
alt = 33; % altitude(AGL)  (m)
wDist = alt/sind(sensorDeg); %Solve for wDist
%alt = sind(sensorDeg).*wDist; %altitude(AGL) %Solve for alt

%% NIIRS coefficients
c0=10.251; c1=-3.16; c2=2.817; c3 = -0.334; c4 = -0.656;

%% SUAS Skin Detection System parameters (SWIR)
suasSd=struct;
suasSd.hSensor =0.0160; %m (Goodrich KTS1.7)
suasSd.vSensor =0.0128; %m
suasSd.hRes = 640; %horiz. resolution pxls
suasSd.vRes = 512; %vert. resolution pxls
suasSd.fLength = 0.035;  %lens focal length (m)

%  For single lens system to find FOV
suasSd.hFOVdeg = atand((suasSd.hSensor/2)./suasSd.fLength).*2;  % horizontal FOV (deg)
suasSd.vFOVdeg = atand((suasSd.vSensor/2)./suasSd.fLength).*2;  % vertical FOV (deg)

if isKnown_wDist == 0    % If solving for working distance
    %pixel size (to solve for working distance)
    suasSd.hSizePxl = 0.05; %Horizonal Size of pixel on target(m)
    suasSd.vSizePxl = 0.05; %Vertical Size of pixel on target(m)
    suasSd.wDist = suasSd.hSizePxl./tand(suasSd.hFOVdeg/suasSd.hRes); % working distance (m)
else  % Else wdist is known
    suasSd.wDist = 60; %m
    suasSd.hSizePxl = tand(suasSd.hFOVdeg/suasSd.hRes).*suasSd.wDist;
    suasSd.vSizePxl = tand(suasSd.vFOVdeg/suasSd.vRes).*suasSd.wDist;
end

suasSd.hFOV = tand(suasSd.hFOVdeg./2).*suasSd.wDist*2; %(m)
suasSd.vFOV = tand(suasSd.vFOVdeg./2).*suasSd.wDist*2; %(m)
suasSd.pArea = suasSd.hFOV.*suasSd.vFOV; %pixel area (m^2)
suasSd.tPxls = suasSd.hRes.*suasSd.vRes; %total pixels
suasSd.pDens = suasSd.tPxls./suasSd.pArea; %pixel density (pxl/m^2)
suasSd.GSDh = 2*tand(suasSd.hFOVdeg/(2*suasSd.hRes))*suasSd.wDist; % meters
suasSd.GSDv = 2*tand(suasSd.vFOVdeg/(2*suasSd.vRes))/cosd(90-sensorDeg)*suasSd.wDist; % meters
suasSd.GSD = (suasSd.GSDh * suasSd.GSDv)^(0.5);
suasSd.SNR = 52; % average SNR for CCD
suasSd.NIIRS = c0 +c1*log10(suasSd.GSDh/.0254) +c2*log10(0.9) +c3*1/suasSd.SNR + c4*1.1;
%% SUAS Skin Detection System parameters (VIS)
suasVIS=struct;
suasVIS.hSensor =0.008195; %m (HHD Omnivision)
suasVIS.vSensor =0.007535; %m
suasVIS.hRes = 1920; %horiz. resolution pxls
suasVIS.vRes = 1080; %vert. resolution pxls
suasVIS.fLength = 0.012;  %lens focal length (m)

suasVIS.hFOVdeg = atand((suasVIS.hSensor/2)./suasVIS.fLength).*2;  % horizontal FOV (deg)
suasVIS.vFOVdeg = atand((suasVIS.vSensor/2)./suasVIS.fLength).*2;  % vertical FOV (deg)

if isKnown_wDist == 0 % If solving for working distance
    %pixel size (to solve for working distance)
    suasVIS.hSizePxl = 0.025; %Horizonal Size of pixel on target(m)
    suasVIS.vSizePxl = 0.025; %Vertical Size of pixel on target(m)
```

```
    %  For single lens system to find FOV
    suasVIS.wDist = suasVIS.hSizePxl./tand(suasVIS.hFOVdeg/suasVIS.hRes); % working distance (m)
else % Else wdist is known
    suasVIS.wDist = 60; %m
    suasVIS.hSizePxl = tand(suasVIS.hFOVdeg/suasVIS.hRes).*suasVIS.wDist;
    suasVIS.vSizePxl = tand(suasVIS.vFOVdeg/suasVIS.vRes).*suasVIS.wDist;
end


suasVIS.hFOV = tand(suasVIS.hFOVdeg./2).*suasVIS.wDist*2; %(m)
suasVIS.vFOV = tand(suasVIS.vFOVdeg./2).*suasVIS.wDist*2; %(m)
suasVIS.pArea = suasVIS.hFOV.*suasVIS.vFOV; %pixel area (m^2)
suasVIS.tPxls = suasVIS.hRes.*suasVIS.vRes; %total pixels
suasVIS.pDens = suasVIS.tPxls./suasVIS.pArea; %pixel density (pxl/m^2)
suasVIS.GSDh = 2*tand(suasVIS.hFOVdeg/(2*suasVIS.hRes))*suasVIS.wDist; % meters
suasVIS.GSDv = 2*tand(suasVIS.vFOVdeg/(2*suasVIS.vRes))/cosd(90-sensorDeg)*suasVIS.wDist; % meters
suasVIS.SNR = 36; %Manufacturer spec sheet =36dB
suasVIS.NIIRS = c0 +c1*log10(suasVIS.GSDh/.0254) +c2*log10(0.9) +c3*1/suasVIS.SNR + c4*1.1;


%% SpecTIR HSI Parameters
specTir=struct;
specTir.hSensor =0.0160; %m
specTir.vSensor =0.0128; %m
specTir.hRes = 640; %horiz. resolution pxls
specTir.vRes = 320; %vert. resolution pxls
specTir.fLength = 0.023;  %lens focal length (m)


%  For single lens system to find FOV
specTir.hFOVdeg = atand((specTir.hSensor/2)./specTir.fLength).*2;  % horizontal FOV (deg)
specTir.vFOVdeg = atand((specTir.vSensor/2)./specTir.fLength).*2;  % vertical FOV (deg)


if isKnown_wDist == 0
    %pixel size (to solve for working distance)
    specTir.hSizePxl = 0.10; %Horizonal Size of pixel on target(m)
    specTir.vSizePxl = 0.10; %Vertical Size of pixel on target(m)
    specTir.wDist = specTir.hSizePxl./tand(specTir.hFOVdeg/specTir.hRes); % working distance (m)
else
    specTir.wDist = 60; %m
    specTir.hSizePxl = tand(specTir.hFOVdeg/specTir.hRes).*specTir.wDist;
    specTir.vSizePxl = tand(specTir.vFOVdeg/specTir.vRes).*specTir.wDist;
end


specTir.hFOV = tand(specTir.hFOVdeg./2).*specTir.wDist*2; %(m)
specTir.vFOV = tand(specTir.vFOVdeg./2).*specTir.wDist*2; %(m)
specTir.pArea = specTir.hFOV.*specTir.vFOV; %pixel area (m^2)
specTir.tPxls = specTir.hRes.*specTir.vRes; %total pixels
specTir.pDens = specTir.tPxls./specTir.pArea; %pixel density (pxl/m^2)

specTir.GSDh = 2*tand(specTir.hFOVdeg/(2*specTir.hRes))*specTir.wDist; % meters
specTir.GSDv = 2*tand(specTir.vFOVdeg/(2*specTir.vRes))/cosd(90-sensorDeg)*specTir.wDist; % meters
specTir.SNR = 66.4; % Manufacturer spec sheet.800:1 = 66.84 dB
specTir.NIIRS = c0 +c1*log10(specTir.GSDh/.0254) +c2*log10(0.9) +c3*1/specTir.SNR + c4*1.1;

%% Monocular Skin Detection Camera (Peskosky, 2010)
monoSd = struct;
monoSd.hSensor =0.0160; %m (Goodrich KTS1.7)
monoSd.vSensor =0.0128; %m
monoSd.hRes = 640; %horiz. resolution pxls
monoSd.vRes = 512; %vert. resolution pxls
monoSd.fLength = 0.150;  %lens focal length (m)


%  For single lens system to find FOV
monoSd.hFOVdeg = atand((monoSd.hSensor/2)./monoSd.fLength).*2;  % horizontal FOV (deg)
monoSd.vFOVdeg = atand((monoSd.vSensor/2)./monoSd.fLength).*2;  % vertical FOV (deg)
if isKnown_wDist == 0
    %pixel size (to solve for working distance)
    monoSd.hSizePxl = 0.05; %Horizonal Size of pixel on target(m)
    monoSd.vSizePxl = 0.05; %Vertical Size of pixel on target(m)
    monoSd.wDist = monoSd.hSizePxl./tand(monoSd.hFOVdeg/monoSd.hRes); % working distance (m)
else
    monoSd.wDist = 6; %m
    monoSd.hSizePxl = tand(monoSd.hFOVdeg/monoSd.hRes).*monoSd.wDist;
    monoSd.vSizePxl = tand(monoSd.vFOVdeg/monoSd.vRes).*monoSd.wDist;
end


monoSd.hFOV = tand(monoSd.hFOVdeg./2).*monoSd.wDist*2; %(m)
monoSd.vFOV = tand(monoSd.vFOVdeg./2).*monoSd.wDist*2; %(m)
```

```
monoSd.pArea = monoSd.hFOV.*monoSd.vFOV; %pixel area (m^2)
monoSd.tPxls = monoSd.hRes.*monoSd.vRes; %total pixels
monoSd.pDens = monoSd.tPxls./monoSd.pArea; %pixel density (pxl/m^2)
monoSd.GSDh = 2*tand(monoSd.hFOVdeg/(2*monoSd.hRes))*monoSd.wDist; % meters
monoSd.GSDv = 2*tand(monoSd.vFOVdeg/(2*monoSd.vRes))/cosd(90-sensorDeg)*monoSd.wDist; % meters
```
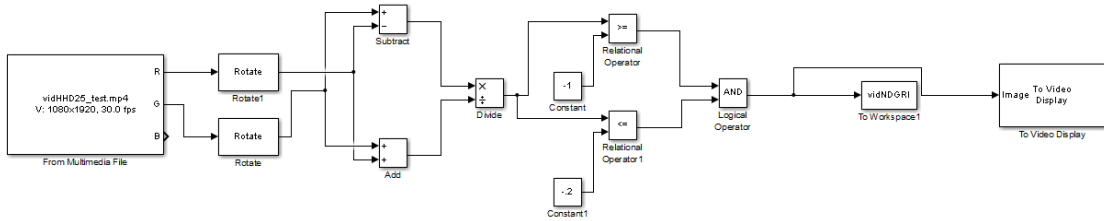
6.2.2 NDGRIvideoViewer.slx

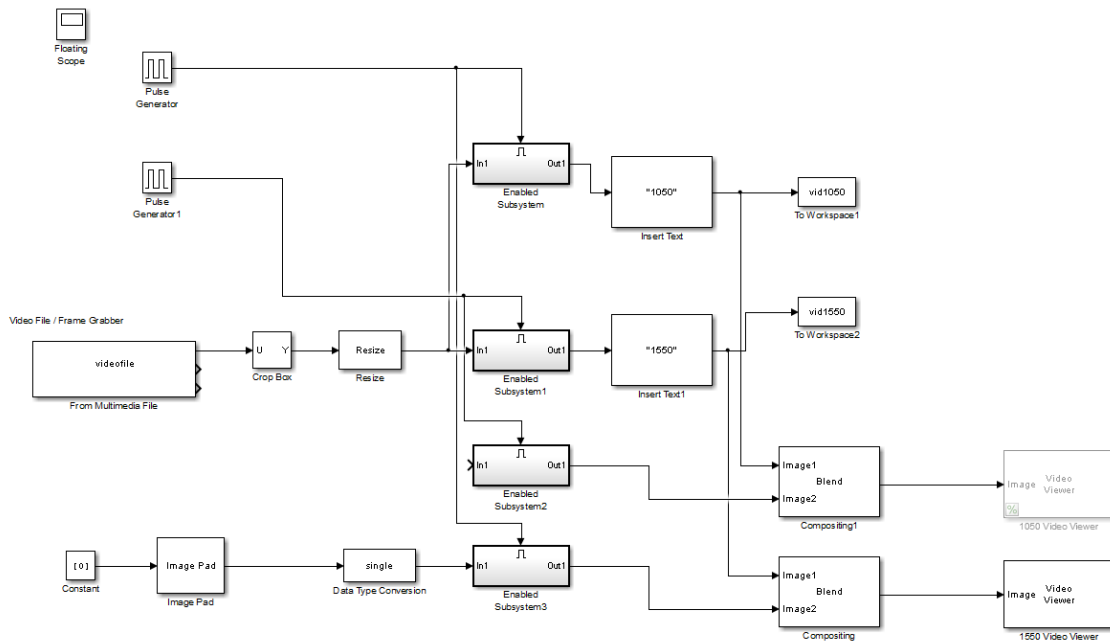Figure 62: Block Diagram for Simulink NDGRI video viewer

6.2.3 NDSIVideoViewer.slx

Figure 63: Block Diagram for Simulink NDSI video viewer

6.3 Appendix C: Waypoint Visualization Code

6.3.1 tlog2flat.m

```matlab
function fltData = tlog2flat(inputTlogtxt,homeLat,homeLong, outputFileName)
%function tlog2flat(inputTlogtxt,outputFileName)
%
% Convert dataflash data to 6DOF Flat Earth model
%
% INPUT:
%           inputTlogtxt: tlog text file that is generated in APM tlog
%                           extractor. See Tlog
%                           data extractor. Format for config file:
%                               mavlink_gps_raw_int_t time_usec
%                               mavlink_global_position_int_t lat
%                               mavlink_global_position_int_t lon
%                               mavlink_global_position_int_t alt
%                               mavlink_attitude_t roll
%                               mavlink_attitude_t pitch
%                               mavlink_attitude_t yaw
%           homeLat:  home latitude near airfield
%           homeLong:  home latitude near airfield
%            %Himsel Field
%             %homeLat = 39.343233;  % degrees
%             %homeLong = -86.029917; % degrees
%            %SUAS Airfield
%             %39.34422; % degrees
%             %-86.00939; % degrees

%           outputFileName (optional): filename string you wish to save data as
%
%
% OUTPUT: flat earth coordinate system 6DOF model
%               n x 7 double array
%               [time, X,Y,Z, roll,pitch,yaw,timeComputer]
%
% Author:  Stephen Sweetnich  AFIT 2013

%% Create flight data structure
%file =inputTlogtxt;  %.csv file From Tlog Data Extractor
% homeLat = 39.343233;  % degrees
% homeLong = -86.029917; % degrees
file = 'I:\SUASFlightTest\19Nov13_FlightTest\tlogs\Extracted_2013-11-19 11-40-58_Flat3.csv';
%file = 'flt2data21Oct13_2.csv';  %.csv file From Tlog Data Extractor
fid = fopen(file);
rawData = textscan(fid, '%s %s %f %f %f %f %f %f %f' , 'delimiter',',','headerlines',1');
fclose('all');

% GPS home reference (Update for every flight if home airfield changes)
if nargin == 1
    % Specify starting locaiton of GPS
    for i = 1:length(rawData{1,3})
        if rawData{1,3}(i) ~=0  &&  rawData{1,4}(i) ~=0
            homeLat = rawData{1,4}(i);
            homeLong = rawData{1,5}(i);
            break
        end
    end
end


time = rawData{1,3}./1000000;  %time
lat = rawData{1,4}./10000000;% degrees
long = rawData{1,5}./10000000;  % degrees
alt = rawData{1,6}./1000;

% Intitialize time at GPS syncronization start
x = 0; i = 1;
while x ~= 1
    if time(i) ~= 0 && lat(i)~=0 && long(i)~=0 && alt(i) ~=0
        x = 1;
    else
        i = i+1;
    end
end
```

```
timeComputer = rawData{1,2}(i:end-100); % time of computer
href = 180; %meters MSL for atterbury field
roll = rad2deg(rawData{1,7}(i:end-100)); % deg
pitch = rad2deg(rawData{1,8}(i:end-100)); % deg
yaw = rad2deg(rawData{1,9}(i:end-100)); % deg
time2 = linspace(0,time(end)-time(i),length(yaw))';


%ecefCoordXYZ =  lla2ecef([lat(i:eol),long(i:eol),alt(i:eol)]);
flatCoordXYZ =  lla2flat([lat(i:end-100),long(i:end-100),-alt(i:end-100)],...
    [homeLat,homeLong],0,href);

% fltData = struct;
% fltData.time = time2;
% fltData.X = ecefCoordXYZ(:,1);
% fltData.Y = ecefCoordXYZ(:,2);
% fltData.Z = ecefCoordXYZ(:,3);
% fltData.phi = roll;
% fltData.theta = pitch;
% fltData.psi = yaw;

fltData = {time2,flatCoordXYZ(:,1),flatCoordXYZ(:,2),flatCoordXYZ(:,3),...
            roll ,pitch, yaw,timeComputer(i:end-100)};
if nargin == 4
    save(outputFileName,'fltData');
    % save('flt2Data21Oct13_flat.mat','fltData');
End
```

6.3.2 df2flat_plusIMU.m

```
function fltData = df2flat_plusIMU(inputDataFlashMat,homeLat, homeLong, outputFileName)
%function df2flat(inputDataFlashMat,outputFileName)
%
% Convert dataflash data to 6DOF Flat Earth model and adds high rate IMU data
%
% INPUT:
%           inputDataFlashMat: Dataflash .mat file that is generated in APM
%           outputFileName(optional) : filename string you wish to save data as
%           homeLat:  home latitude near airfield
%           homeLong:  home latitude near airfield
%            % Himsel Field
%             %homeLat = 39.343233;  % degrees
%             %homeLong = -86.029917; % degrees
%            % SUAS Airfield
%             %homeLat = 39.34422; % degrees
%             %homeLong = -86.00939; % degrees
%
% OUTPUT: flat earth coordinate system 6DOF model
%             n x 7 double array
%             [time, X,Y,Z, roll,pitch,yaw, GyrX,GyrY,GyrZ,AccX,AccY,AccZ]
%
% Author:  Stephen Sweetnich  AFIT 2013
%

% load flight data structure
S = load (inputDataFlashMat); %'2013-10-21 16-26 6.log.mat'
%S = load( 'I:\SUASFlightTest\21Oct13_FlightData\dataflashLogs\2013-10-21_16-29_7.log.mat');
%% Specify logging rates from Autopilot

% (User Selects proper logging rates)
gpsOffset = S.GPS(1,1);
gpsRate = 5;  %Hz  For APM MediaTek GPS
gpsLines = S.GPS(end,1);

attRate = 10; %50; %Hz  For APM 2.6 DataFlash
attLines = S.ATT(end,1);

imuRate = 50; %10; %Hz  For APM 2.6 DataFlash
imuLines = S.IMU(end,1);

%% Select parameter with highest rate
% Interpolations are made between the highest rate data
[highestRate, param] = max([attRate,imuRate]);
    if param ==1;
        totLines =S.ATT(end,1);
    else
```

```matlab
        totLines =S.IMU(end,1);
    end

%% Initialize data structure assembly
% Preallocate data structure
t = zeros(totLines,1);
dt = zeros(totLines,1);
lat = zeros(totLines,1);
long = zeros(totLines,1);
alt = zeros(totLines,1);
roll = zeros(totLines,1);
pitch = zeros(totLines,1);
yaw = zeros(totLines,1);
gyrX = zeros(totLines,1);
gyrY = zeros(totLines,1);
gyrZ = zeros(totLines,1);
accX = zeros(totLines,1);
accY = zeros(totLines,1);
accZ = zeros(totLines,1);

% Run a loop on structure and fill in values for rawData
x=0;i=1;
for i =1:totLines
    if i < size(S.GPS,1)
        m1 = S.GPS(i,1)-1;
        t(m1) = S.GPS(i,3)/1000;
        lat(m1) = S.GPS(i,6);
        long(m1) = S.GPS(i,7);
        alt(m1) = S.GPS(i,8);
    end

    if i < size(S.ATT,1)
        m2 = S.ATT(i,1);
        roll(m2)= S.ATT(i,2);
        pitch(m2) = S.ATT(i,3);
        yaw(m2) = S.ATT(i,4);
    end

    if i < size(S.IMU,1)
        m3 = S.IMU(i,1);
        gyrX(m3) = S.IMU(i,2);
        gyrY(m3) = S.IMU(i,3);
        gyrZ(m3) = S.IMU(i,4);
        accX(m3) = S.IMU(i,5);
        accY(m3) = S.IMU(i,6);
        accZ(m3) = S.IMU(i,7);
    end

    if t(i)~= 0
        t(i-1)=t(i);
        lat(i-1)=lat(i);
        long(i-1)= long(i);
        alt(i-1)=alt(i);

    end

end

% Populate raw data structure with all non zero values if possible
x=0;k=1;c=1;
while x ~=1
    if (t(k)~=0 || lat(k)~=0 || long(k)~=0 || alt(k)~=0 || ...
            roll(k)~=0 || pitch(k)~=0 || yaw(k) ~=0 || ...
            gyrX(k) ~=0||gyrY(k) ~=0 || gyrZ(k) ~=0)
        rawData(c,1) = t(k);
        rawData(c,2) = lat(k);
        rawData(c,3) = long(k);
        rawData(c,4) = alt(k);
        rawData(c,5) = roll(k);
        rawData(c,6) = pitch(k);
        rawData(c,7) = yaw(k);
        rawData(c,8) = gyrX(k);
        rawData(c,9) = gyrY(k);
        rawData(c,10) = gyrZ(k);
        rawData(c,11) = accX(k);
        rawData(c,12) = accY(k);
        rawData(c,13) = accZ(k);
        c=c+1;
    end
```

```matlab
        if k == length(t)
            x=1;
        end
        k=k+1;
    end

%% Linearly interpolate between GPS readings

% If GPS time is same as next reading, make it zero
for l = 2:length(rawData)
    if rawData(l,1)==rawData(l-1,1)
        rawData(l,1) = 0;
        rawData(l,2) = 0;
        rawData(l,3) = 0;
        rawData(l,4) = 0;
    end
end

id1=1; id2=2;
for i=1:length(rawData)
    if [rawData(i,1:4)] ~= [0 0 0 0]
        id2 =i;
        delta = id2-id1;
        for j=1:(delta-1)
            for k=1:4
            % Interpolation for time
            rawData(id2-j,k)= (((delta-j)/delta)*(rawData(id2,k)-rawData(id1,k)))+rawData(id1,k);
%               % Interpolation for lat
%               rawData(id2-j,2)= (((delta-j)/delta)*(rawData(id2,2)-rawData(id1,2)))+rawData(id1,2);
%               % Interpolation for long
%               rawData(id2-j,3)= (((delta-j)/delta)*(rawData(id2,3)-rawData(id1,3)))+rawData(id1,3);
%               % Interpolation for alt
%               rawData(id2-j,4)= (((delta-j)/delta)*(rawData(id2,4)-rawData(id1,4)))+rawData(id1,4);
            end
        end
        id1=id2;
    else
        id2=i;
    end
end
%% Linearly interpolate between ATT
cols =[5:7];
id1=1; id2=2;
for i=1:length(rawData)
    if [rawData(i,cols)] ~= zeros(1,length(cols))
        id2 =i;
        delta = id2-id1;
        for j=1:(delta-1)
            for k= 1:length(cols)
            % Interpolation for time
            rawData(id2-j,cols(k))= (((delta-j)/delta)*(rawData(id2,cols(k))-
rawData(id1,cols(k))))+rawData(id1,cols(k));
            end
        end
        id1=id2;
    else
        id2=i;
    end
end
%% Linearly interpolate between IMU readings
cols =[8:13];
id1=1; id2=2;
for i=1:length(rawData)
    if [rawData(i,cols)] ~= zeros(1,length(cols))
        id2 =i;
        delta = id2-id1;
        for j=1:(delta-1)
            for k= 1:length(cols)
            % Interpolation for time
            rawData(id2-j,cols(k))= (((delta-j)/delta)*(rawData(id2,cols(k))-
rawData(id1,cols(k))))+rawData(id1,cols(k));
            end
        end
        id1=id2;
    else
        id2=i;
    end
end
```

111

```matlab
%% Clip bad data from beginning when GPS hasn't initiailized

% find when GPS was synchronized and when it was lost
nonz = find(S.GPS(:,6));
gdata = sort(nonz);
clipLine = S.GPS(gdata(1),1);
lastLine = S.GPS(gdata(end),1);
epochTime =S.GPS(gdata(1),3)/1000;


%
% for i=1:length(S.GPS);
%     if S.GPS(i,3)~=0
%          break
%     else
%          i=i+1;
%     end
% end
% epochTime = S.GPS(i,3)/1000;
% clipLine = S.GPS(i,1);

%% build structure in lla system
totLines = size(rawData,1)-clipLine;
% Preallocate data structure
llaData = zeros(totLines,7);

c=clipLine;
for i=1:totLines
    llaData(i,1) = rawData(c,1)-epochTime;  %time(s)
    llaData(i,2) = rawData(c,2); %lat degrees
    llaData(i,3) = rawData(c,3); %long degrees
    llaData(i,4) = rawData(c,4); %alt(m)
    llaData(i,5) = rawData(c,5); %roll rad
    llaData(i,6) = rawData(c,6); %pitch rad
    llaData(i,7) = rawData(c,7); %yaw rad
    llaData(i,8) = rawData(c,8);     %imu GyrX
    llaData(i,9) = rawData(c,9);     %imu GyrY
    llaData(i,10) = rawData(c,10);   %imu GyrZ
    llaData(i,11) = rawData(c,11);   %imu AccX
    llaData(i,12) = rawData(c,12);   %imu AccY
    llaData(i,13) = rawData(c,13);   %imu AccZ
    c=c+1;
end
%% Convert to flat earth model system

% GPS home reference (Update for every flight if home airfield changes)at
if nargin == 1
    % Specify starting locaiton of GPS
    homeLat = llaData(1,2); %(deg) Use GPS data after initialized
    homeLong = llaData(1,3);    %(deg)
end

% Approximate Location of skin dismounts
% d_Lat = homeLat;
% d_Long = homeLong;

%Altitude MSL for atterbury field
href =-180; %-216; %(m)

%ecefCoordXYZ =  lla2ecef(llaData(:,2:4);
flatCoordXYZ =  lla2flat(llaData(:,2:4),...
    [homeLat,homeLong],0,href,'WGS84' );

% fltData = struct;
% fltData.time = time2;
% fltData.X = ecefCoordXYZ(:,1);
% fltData.Y = ecefCoordXYZ(:,2);
% fltData.Z = ecefCoordXYZ(:,3);
% fltData.phi = roll;
% fltData.theta = pitch;
% fltData.psi = yaw;

fltData = [llaData(:,1),flatCoordXYZ(:,1),flatCoordXYZ(:,2),abs(flatCoordXYZ(:,3)),...
            llaData(:,5:13)];
if nargin ==4
  save(outputFileName,'fltData');
end
```

6.4 Appendix D: Sensor Postprocessing Code

6.4.1 GenerateROCs

```
% Generate ROC Curves from ENVI files (specifically for Ground HSI imager)
%
% Utilizes roc() and auroc() by  Fawcett, T., "ROC graphs : Notes and practical
%           considerations for researchers", Technical report, HP
%           Laboratories, MS 1143, 1501 Page Mill Road, Palo Alto
%           CA 94304, USA, April 2004.
%
% Input the ENVI files with gui and generate ROC curves
%
% Author:  Stephen Sweetnich  AFIT 2013
clear all
clc

%% Get Image Data
% ENVI Import Cube and Register images

[datafile, datapath, ~] = uigetfile(['*.*'],'Select a data file');
%hdrfile = [datafile(1:end-4) '.hdr'];
hdrfile = [datafile '.hdr'];
[truth_file, truthpath,~] = uigetfile('*.txt','Select a truth file');
[I, hdr] = enviread([datapath datafile],[datapath hdrfile]);
%nI = permute(I, [2 1 3]);  % Changes Image to [row x lines x bands]
%%
nI = I ;% permute not needed for processed ENVI data
img = imrotate(nI,90, 'nearest');
%clear nI I
sizeDetection = size(img);


%% Use ENVI Detection
% %  Apply Bandmath
% %new imager
% %1080nm: band 139
% %1580nm: band 219
% %660nm: band 58
% %540nm: band 33
% For 4 band file, comment out this:
%        ndsi = (img(:,:,139)-img(:,:,219))./(img(:,:,139)+img(:,:,219)); Calculate NDSI
%        ndgri = (img(:,:,58)-img(:,:,33))./(img(:,:,58)+img(:,:,33)); Calculate NDGRI
%
%For4bandfile
ndsi = (img(:,:,3)-img(:,:,4))./(img(:,:,3)+img(:,:,4));
ndgri = (img(:,:,2)-img(:,:,1))./(img(:,:,2)+img(:,:,1));

ndgriThreshold=0.025;
ndsiROC = [];
for i=1:size(ndsi,1)
    for j=1:size(ndsi,2)
        if ndgri(i,j) > ndgriThreshold
            ndsiROC(i,j) = ndsi(i,j);
        else
            ndsiROC(i,j) = ndsi(i,j)-1;
        end
    end
end

% Normalize the data and plot result
%figure(1)
normalizeNDSI = @(x) (x + 2) .* (1 - 0) ./ (1 + 2) + 0;
detectNorm = normalizeNDSI(ndsiROC);
imshow(detectNorm)
% detectNorm = mapminmax(img(:,:,1),0,1);
%% Import Truth file
% Select Option in ENVI to Output ROI to ASCII
fid = fopen([truthpath truth_file]);
format = '%u %u %u %u';
ROI = textscan(fid, format, 'Headerlines', 8);

truthIM =zeros(sizeDetection([2,1]));
for i=1:ROI{1,1}(end)
    truthIM(ROI{1,3}(i),ROI{1,2}(i))=1;
end
```

```
truthIM = imrotate(truthIM,90);
%figure(2); axis image
%imshow(truthIM);


%% Reshape data
sizeIM= size(detectNorm);
target = reshape(truthIM,1,sizeIM(1)*sizeIM(2));
output = reshape(detectNorm,1,sizeIM(1)*sizeIM(2));

%% Generate ROC Curve
figure(3);
hold on
[tp, fp] = roc2(target', output');
auROC = auroc(tp,fp);
plot(fp,tp,'b');

%%
legend(labels)
xlabel('False Positive Rate','FontSize', 16);
ylabel('True Positive Rate','FontSize', 16);
% title('SpecTIR Receiver Operating Charachteristic (ROC)');
% text(0.5,0.5,['Area Under Curve = ' num2str(auROC)]);
%hold off
```

6.5 Appendix E: Relevant TRB/SRB Documentation

6.5.1 Test Objective 1 – Verification of Autopilot Gain Settings and

Configuration

TEST SCENARIO 1	
Description	Determine appropriate gain settings for autonomous operation.
Stakeholders	Stephen R. Sweetnich, AFIT /ENV
Success Criteria	Test Matrix | Test Point	Description	Altitude AGL (±30ft)	Radius	No Patterns
---	---	---	---	---
1.1	Gain Test	164 ft	N/A	N/A	 NOTE: Approximate gain settings will be entered before gain tuning. Gain settings for throttle will be speed controlled at approximately 30 mph (26 kts)
Evaluation Criteria	**Satisfactory if:** Working gain settings are achieved for normal flight.
Data Requirements	Required 1. Approximate gain settings. 2. Telemetry and mission planner software.

Algorithms	Mission Planner Tuning interface
Expected Results	1. Tuned gain settings for APM 2. Verification of configuration hardware and software.
Assets	AFIT Electric Sig Rascal with APM 2.5 and 2.74 FW

Test Methodology	**Test Procedures**
	1. BEFORE TAKEOFF:
	    a. Setup ground control station and operating area IAW AFIT Document 5028.
	    b. Complete all required preflight checklists for UAS.
	    c. Check that weather is within limits and determine launch/recovery locations and headings.
	    d. Open airspace with range control.
	
	2. LAUNCH:
	    a. Ensure that all present personnel are aware of launch.
	    b. Position aircraft for ground launch.
	    c. Safety pilot executes takeoff.
	    d. Safety pilot announces that aircraft is airborne.
	    e. Climb to pre-briefed transition altitude.
	    f. Transition to pre-briefed test-point entry position.
	
	3. EXECUTE TEST POINTS:
	    a. Ensure GS is recording telemetry file for entire flight.
	    b. Initiate flight with stabilize mode.
	    c. Ensure gain settings are appropriate
	    d. Write test waypoints, enter autopilot mode and ensure gain stability when crossing from 'stabilize' to 'auto'.
	    e. Once patterns finished, execute recovery
	
	4. RECOVERY:
	    a. Navigate aircraft to pre-briefed recovery transition location.
	    b. Transition aircraft to safety pilot control or observation.
	    c. Ensure landing area is clear of personnel and equipment.
	    d. Begin descent and entry into landing pattern.
	    e. Safety pilot announces landing to all present personnel.
	    f. Execute recovery.
	
	5. AFTER RECOVERY:
	    a. Stop telemetry capture on laptop or ensure that data log is saved.
	    b. Close airspace with range control.

	c. Disconnect aircraft battery power prior to moving aircraft by hand.
	d. Power off RC transmitter as required.
	e. Power off video capture equipment as required.
	f. Power off ground control station as required.

6.5.2 Test Objective 2- Capture Multispectral Video Data

TEST SCENARIO 2	
Description	Collect high resolution linear and rotational acceleration data from autopilot onboard Electric Sig Rascal.
Stakeholders	Stephen R. Sweetnich, AFIT /ENV
Success Criteria	Test Matrix (see table below)
Evaluation Criteria	**Satisfactory if:** Imagery data is collected for both sensors. Data quality is adequate for video processing.
Data	Required

Test Matrix

Test Point	Description	Sensor Angle	Filter Rate	Altitude AGL (±10ft)	No Patterns
2.1	Racetrack 1	30°	High	186 ft	3
2.2	Racetrack 2	30°	High	140 ft	3
2.3	Racetrack 3	30°	High	100 ft	3
2.4	Racetrack 4	30°	Low	186 ft	3
2.5	Racetrack 5	30°	Low	140 ft	3
2.6	Racetrack 6	30°	Low	100 ft	3
2.7	Racetrack 7	45°	Low	186 ft	3
2.8	Racetrack 8	45°	Low	140 ft	3
2.9	Racetrack 9	45°	Low	100 ft	3
2.10	Racetrack 10	45°	High	186 ft	3
2.11	Racetrack 11	45°	High	140 ft	3
2.12	Racetrack 12	45°	High	100 ft	3

Note: Throttle setting from gain tuning (slow as possible) will be used and maintained. Throttle will be speed controlled at approximately 30 mph (26 kts)

Requirements	1. Tuned gain settings for settings for ArduPlane 2.74 settings. See Objective 1. 2. Telemetry and mission planner software. 3. Video systems are able to collect footage.
Algorithms	1. Multispectral imagery via Goodrich SWIR and mini DVR 2. VIS EO imagery via HackHD 3. Software to actuate multiple rotating disks via filter exchange unit
Expected Results	High resolution (50Hz) accelerometer and gyro data is collected with APM's on-board 16MB datalogging memory and GS via Mission Planner.
Assets	1. AFIT Electric Sig Rascal with APM 2.5 and 2.74 FW

Test Methodology	**Test Procedures**
	1. BEFORE TAKEOFF:
	  a. Setup ground control station and operating area IAW AFIT Document 5028.
	  b. Preload UAS waypoint profile with designated flight paths.
	  c. Ensure APM telemetry data link with Mission Planner and GCS logging is enabled.
	  d. Complete all required preflight checklists for UAS.
	  e. Check that weather is within limits and determine launch/recovery locations and headings.
	  f. Open airspace with range control.
	
	2. LAUNCH:
	  a. Ensure that all present personnel are aware of launch.
	  b. Position aircraft for ground launch.
	  c. Safety pilot executes takeoff.
	  d. Safety pilot announces that aircraft is airborne.
	  e. Climb to pre-briefed transition altitude.
	  f. Transition to pre-briefed test-point entry position.
	
	3. EXECUTE TEST POINTS:
	  a. Ensure GS is recording telemetry file for entire flight.
	  b. Initiate flight with stabilize mode.
	  c. Ensure gain settings are appropriate (Objective 1) before switching to auto mode.
	  d. Fly appropriate racetrack at each desired condition in the test matrix (test points 2.1-2.12).
	  e. Write waypoints, enter autopilot mode
	  f. Once patterns finished, execute recovery

	4. RECOVERY:
	a. Navigate aircraft to pre-briefed recovery transition location.
	b. Transition aircraft to safety pilot control or observation.
	c. Ensure landing area is clear of personnel and equipment.
	d. Begin descent and entry into landing pattern.
	e. Safety pilot announces landing to all present personnel.
	f. Execute recovery.
	5. AFTER RECOVERY:
	a. Stop telemetry capture on laptop or ensure that data log is saved.
	b. Close airspace with range control.
	c. Disconnect aircraft battery power prior to moving aircraft by hand.
	d. Power off RC transmitter as required.
	e. Power off video capture equipment as required.
	f. Power off ground control station as required.

6.5.3 *Test Objective 3- Measure High Resolution INS Data*

TEST SCENARIO 3	
Description	Collect high resolution linear and rotational acceleration data from autopilot onboard Electric Sig Rascal.
Stakeholders	Stephen R. Sweetnich, AFIT /ENV
Success Criteria	Test Matrix | Test Point	Description	Altitude AGL (±10 ft)	Radius/Standoff	No Patterns
---	---	---	---	---
3.1	Racetrack 1	186 ft	82 ft	3
3.2	Racetrack 2	140 ft	82 ft	3
3.3	Racetrack 3	100 ft	82 ft	3	 Note: Throttle setting from gain tuning will be used and maintained. Throttle will be speed controlled at approximately 30 mph (26 kts)
Evaluation Criteria	<u>**Satisfactory if:**</u> INS data at is collected from one source, for all test patterns.
Data Requirements	Required 1. Tuned gain settings for settings for ArduPlane 2.74 settings. See

	Objective 1. 2. Telemetry and mission planner software. 3. High collection rate for onboard Autopilot

Algorithms	1. Data Recorded from Ardupilot:
	    a. Accelerometer X, Y,Z axes (mg)
	    b. Gyroscope Pitch, Roll, Yaw rates.(rad/s)
	    c. Speed (m/s)

Expected Results	High resolution (50Hz) accelerometer and gyro data is collected with APM's on-board 16MB datalogging memory and GS via Mission Planner. Also, a backup INS will log information.
Assets	AFIT Electric Sig Rascal with APM 2.5 and 2.74 FW

Test Methodology	**Test Procedures**
	1. BEFORE TAKEOFF:
	    a. Setup ground control station and operating area IAW AFIT Document 5028.
	    b. Preload UAS waypoint profile with designated flight paths.
	    c. Ensure APM telemetry data link with Mission Planner and GCS logging is enabled.
	    d. Complete all required preflight checklists for UAS.
	    e. Check that weather is within limits and determine launch/recovery locations and headings.
	    f. Open airspace with range control.
	
	2. LAUNCH:
	    a. Ensure that all present personnel are aware of launch.
	    b. Position aircraft for ground launch.
	    c. Safety pilot executes takeoff.
	    d. Safety pilot announces that aircraft is airborne.
	    e. Climb to pre-briefed transition altitude.
	    f. Transition to pre-briefed test-point entry position.
	
	3. EXECUTE TEST POINTS:
	    a. Ensure GS is recording telemetry file for entire flight.
	    b. Initiate flight with stabilize mode.
	    c. Ensure gain settings are appropriate before switching to auto mode.
	    d. Execute racetracks for test points 3.1-3.3.
	    e. Once patterns finished, execute recovery
	
	4. RECOVERY:
	    a. Navigate aircraft to pre-briefed recovery transition location.

| | b. Transition aircraft to safety pilot control or observation.
c. Ensure landing area is clear of personnel and equipment.
d. Begin descent and entry into landing pattern.
e. Safety pilot announces landing to all present personnel.
f. Execute recovery.

5. AFTER RECOVERY:
    a. Stop telemetry capture on laptop or ensure that data log is saved.
    b. Close airspace with range control.
    c. Disconnect aircraft battery power prior to moving aircraft by hand.
    d. Power off RC transmitter as required.
    e. Power off OSD video capture equipment as required.
    f. Power off ground control station as required. |

7. References

Aeryon Labs Inc. (2013). Aeryon Scout Suas Supports Critical Florida Wildfire Research. Retrieved 30 June, 2013, from http://www.aeryon.com/news/latest-news/pressreleases/541-uaf-scout-research.html#sthash.PlRsviGy.dpuf

ASD Inc. (2012). *FieldSpec 4 User Manual* [ASD Document 600979] (B ed.) ASD Inc.

Beard, R. W., & McLain, T. W. (2012). *Small Unmanned Aircraft:Theory and Practice* (1st ed.). Princeton and Oxford: Princeton University Press.

Beisley, A. P. (2012). *Spectral Detection Of Human Skin In VIS-SWIR Hyperspectral Imagery Without Radiometric Calibration.* (Masters Thesis, Air Force Institute of Technology, WPAFB). . (AFIT/GE/ENG/12-03).

Bertin, J. J. (2002). *Aerodynamics for engineers* (Fourth Edition ed.). Upper Saddle River, New Jersey: Prentice Hall.

Blanchard, B. S., & Fabrycky, W. J. (2010). *Systems Engineering And Analysis* (5th ed.). USA: Prentice Hall. doi:ISBN-10:0132208989

Bouguet, J. (2013). *Camera calibration toolbox for Matlab*. California Institute of Technology

Brand, J., & Mason, J. S. (2000). A Comparative Assessment Of Three Approaches To Pixel Level Human Skindetection. *Intl. Conf. on Pattern Recognition, 1*, 1056-1059. doi:10.1109/ICPR.2000.905653

Chan, A. (2014). *An Assessment of Normalized Difference Skin Index Robustness in Aquatic Environments.* (Masters Thesis, Air Force Institute of Technology, WPAFB). (AFIT-ENG-14-M-24).

Cho, P., & Snavely, N. (2013). 3D Exploitation of 2D Ground-level & Aerial Imagery. Paper presented at the *2011 IEEE Applied Imagery Pattern Recognition Workshop,* 1-8. doi:ISBN: 978-1-4673-0215-9

Civera, J., Davidson, A., & María Martínez Montiel, J. (2012). Points at Infinity: Mosaics using the Extended Kalman Filter. *Structure from motion using the extended kalman filter* (pp. 13-32). Berlin Heidelberg: Springer-Verlag. doi:ISBN-10: 3642248330

Comninos, P. (2011). *Mathematical and computer programming techniques for computer graphics*. U.S: Springer. doi:ISBN-13: 978-1-8233-902-9

Department of Air Force. (2012). *Small Unmanned Aerial Systems Training. AFI 11-502*. Washington DC: Department of Defense: April 26, 2012.

Donahue, J. (1991). *Introductory Review of Target Discrimination Criteria.* (No. AD-254 954). Hanscom Air Force Base , Mass: Philips Laboratory, Dynamics Research Corporation.

Edmund Optics. (2013). The Correct Material For Infrared (IR) Applications. Retrieved December, 13, 2013, from http://www.edmundoptics.com/technical-resources-center/optics/the-correct-material-for-infrared-applications/

Eichenholz, J. M., & Dougherty, J. (2009). Ultracompact Fully Integrated Megapixel Multispectral Imager. *SPIE 7218: Integrated Optics: Devices, Materials, and Technologies XIII,* San Jose, CA. (721814) doi:10.1117/12.809527

Excelis Inc. (2013). *ENVI* (5.0th ed.)

FAA. (2007). *Aircraft Weight And Balance Handbook: FAA-H-8083-1A*. Washington: U.S. Government Printing.

FlightGear. (2013). *FlightGear Flight Simulator* (2.12.1 ed.)

Giacomo, C. (2012). *Modeling, simulation, and flight testing for automatic flight control of the condor hybrid-electric remote piloted aircraft.* (Masters Thesis, Air Force Institute of Technology). . (AFIT/GSE/ENV/12-M04).

Grahn, H. F., Geladi, P., & Burger, J. E. (2007). Multivariate Images, Hyperspectral Imaging: Background And Equipment. In H. F. G. Grahn P. (Ed.), *Techniques And Applications Of Hyperspectral Image Analysis* (1st ed., pp. 1-16). West Sussex, England: John Wiley and Sons. doi:ISBN: 978-0-470-01086-0

Gundlach, J. (2012). *Designing Unmanned Aircraft Systems: A Comprehensive Approach* American Institute of Aeronautics and Astronautics. doi:ISBN: 978-1-60086-843-6

Hartley, R., & Zisserman, A. (2003). *Multiple View Geometry In Computer Vision* (2nd ed.). New York, NY, USA: Cambridge University Press.

Hsu, S. M., & Burke, H. K. (2003). Multisensor Fusion with Hyperspectral Imaging Data: Detection And Classification. *Lincoln Laboratory Journal, 14*(1), 145-159.

Jodeh, N. M. (2006). *Development Of Autonomous Unmanned Aerial Vehicle Research Platform: Modeling Simulating, And Flight Testing.* (Masters Thesis, Air Force Institute of Technology, WPAFB). . (AFIT/GAE/ENY/06-M18).

Kerkes J. P., & Hsu, S. M. (2004). Spectral Quality Metrics For Terrain Classification. *Imaging Spectrometry X, 5546*, 382-389. doi:10.1117/12.560025

Kessler, O., White, F. (2009). Data Fusion Perspective and Its Role in Information Processing. In M. Liggins (Ed.), *Handbook Of Multisensor Data Fusion: Theory And Practice* (2nd ed., pp. 15-44) CRC Press.

Koch, B. M. (2011). *A Multispectral Bidirectional Reflectance Distribution Function Study Of Human Skin For Improved Dismount Detection.* (Masters Thesis, Air Force Institute of Technology, WPAFB). . (AFIT/GE/ENG/11-22).

Liggins, M., Hall, D., & Llinas, J. (2008). In M.E.L., D.L.H. (Eds.), *Handbook of Multisensor Data Fusion: Theory And Practice, Second Edition*. Boca Raton, FL: CRC Press.

Lluis-Gomez, A., & Edirisnghe, E. A. (2012). Chromatic Aberration Correction In Raw Domain For Image Quality Enhancement In Image Sensor Processors. *IEEE, 12*, 241-244. doi:978-1-4673-2952-1

Lowe, D. G. (2004). Distinctive Image Features From Scale-Invariant Keypoints. *International Journal of Computer Vision, 60*(2), 91-110.

Mansurov, N. (2011). Photography Life: What Is Chromatic Aberration. Retrieved 20 December, 2013, from http://photographylife.com/what-is-chromatic-aberration

Mariottini, G. L., & Prattichizzo, D. (2005, December). The Epipolar Geometry Toolbox: Multiple View Geometry and Visual Servoing For MATLAB. *IEEE Robotics and Automation Magazine, 3, no12*

McCauley, M. (2013). *Accelstepper Library For Arduino*

Melexis. (2006). *Datasheet, US5881- Unipolar Hall Switch – Low Sensitivity* (7th ed.) Microelectronic Integrated Systems. doi:Doc Id: 3901005881

Merino, L., Fernando, C., Martinez-de Dios, J. R., Ferruz, J., & Ollero, A. (2006). A Cooperative Percetion System for Multiple Uavs: Application To Automatic Detection Of Forest Fires. *Journal of Field Robotics, 23*(3-4), 165-184.

Morales, J. L. (2012). *Computer Aided Multi-Data Fusion Dismount Modeling.* (Masters Thesis, Air Force Insitute of Technology). doi:March 2012. (AFIT/GE/ENG/12-29).

Muller, A. C., & Narayanan, S. (2009). Cognitively-Engineered Multisensor Image Fusion for Military Applications. *Information Fusion, 10*(2), 137-149. doi:10.1016/j.inffus.2008.08.008

Narvekar, N. D., & Karam, L. J. (2011). A No Reference Perceptual Image Sharpness Metric Based on a Cumulative Probability Of Blur Detection. *IEE Transactions on Image Processing, 20*(9), 2678-2683. doi:978-1-4244-4370-3/09

NASA. (2011). Landsat 7: Science Data User Handbook. Retrieved 10 December, 2013, from http://landsathandbook.gsfc.nasa.gov/data_prod/prog_sect11_3.html

Nebiker, S., Annen, A., Scherrer, M., & Oesch, D. (2008). A Light-Weight Multispectral Sensor for Micro UAV- Opportunities for Very High Resolution Airborne Remote Sensing. *The International Archives of the Photogrammetry, Remote Sensing and Spatial Information Sciences., 37*(B1), 1193-1200.

Nunez, A. S. (2009). *A Physical Model of Human Skin and Its Application for Search and Rescue.* (Doctoral Dissertation, Air Force Institute of Technology, WPAFB). . (AFIT/DEO/ENG/09-14).

Omnivision. (2009). *OV9810 9 Megapixel 1080p HD Video Image Sensor-Product Brief* (1.1st ed.). Santa Clara, CA:

Peskosky, K. (2010). *Design of a Monocular Multi-Spectral Skin Detection, Melanin Estimation, and False-Alarm Suppression System.* (Masters Thesis, Air Force Institute of Technology, WPAFB). . (AFIT/GE/ENG/10-24).

Premerlani, W., & Bizard, P. (2009). *Direction cosine matrix IMU:Theory.* Unpublished manuscript.

Rao, R., & Arora, M. K. (2004). Image Processing Overview. In K. Pramod, & M. K. Arora (Eds.), *Advanced Image Processing Techniques for Remotely Sensed Hyperspectral Data* (pp. 51-82) Springer. doi:ISBN: 978-3-662-05605-9

Ronan, P. G. (2013). (2nd ed.). Wiki Commons:

Sambora, M. D. (2008). *Statistical Methods for Image Registration and Denoising.* (Doctoral Dissertation, Air Force Institute of Technology, WPAFB). doi:ADA485153. (AFIT/DCE/ENG/08-14).

Sato, K. (2006). Image processing alogrithms. In J. Nakamura (Ed.), *Image sensor and signal processing for digital still cameras* (pp. 223-253). Boca Raton, FL: CRC Press. doi:ISBN-13:978-0-8493-3545-7

Shaw, G. A., & Burke, H. K. (2003). Spectral Imaging for Remote Sensing. *Lincoln Laboratory Journal, 14*(1), 3-28.

SpecIM. (2013). Airborne Imager Datasheets. Retrieved Jan/06, 2014, from http://www.specim.fi/index.php/products/airborne/

SpecTIR. (2012). *Prospectir Instrument Calibration and Data Processing Overview.* Reno, NV: SpecTIR.

Steinberg, A. N., & Bowman, C. L. (2010). Revisions to the JDL Fusion Model. In M. Liggin, & D. Hall (Eds.), *Handbook of multisensor data fusion: Theory and practice* (2nd ed., pp. 45-67) CRC Press. doi:ISBN-13: 978-1-4200-5308-1

Supermagnete. (2013). FAQ - Frequently Asked Questions: Block Magnet. Retrieved 12/7, 2013, from http://www.supermagnete.de/eng/faq/How-do-you-calculate-the-magnetic-flux-density

Thorlabs. (2010). *BSC101: Benchtop Stepper Motor Controller, User Guide. HA0133T* (Rev 10 ed.). Newtown, NJ: Thorlabs Inc.

Thurman, S. L., & Fienup, J. R. (2010). Application of the general image-quality equation to aberrated imagery. *Applied Optics, 49*(11), 2132-2142. doi:Doc. ID 120078

U.S. Geological Survey. (2011). *United States Geological Survey Unmanned Aircraft Systems Roadmap 2010 - 2025* . (No. Version 1.0 rev. A). Denver, CO: Opustek.

Welborn, J. W. (2013). Calibration and Extension of a Discrete Event Operations Simulation Modeling Multiple Un-Manned Aerial Vehicles Controlled by a Single Operator. (Masters Thesis, Air Force Institute of Technology, WPAFB). . (AFIT-ENV-13-M-34).

Xydeas, C.,S., & Petrovic, V. (2000). Objective Image Fusion Performance Measure. *Electronics Letters, 36*(4), 308-9.

<table>
<tr><td colspan="2">REPORT DOCUMENTATION PAGE</td><td><i>Form Approved</i>
<i>OMB No. 074-0188</i></td></tr>
</table>

REPORT DOCUMENTATION PAGE		*Form Approved* *OMB No. 074-0188*

The public reporting burden for this collection of information is estimated to average 1 hour per response, including the time for reviewing instructions, searching existing data sources, gathering and maintaining the data needed, and completing and reviewing the collection of information. Send comments regarding this burden estimate or any other aspect of the collection of information, including suggestions for reducing this burden to Department of Defense, Washington Headquarters Services, Directorate for Information Operations and Reports (0704-0188), 1215 Jefferson Davis Highway, Suite 1204, Arlington, VA 22202-4302. Respondents should be aware that notwithstanding any other provision of law, no person shall be subject to any penalty for failing to comply with a collection of information if it does not display a currently valid OMB control number.
PLEASE DO NOT RETURN YOUR FORM TO THE ABOVE ADDRESS.

1. REPORT DATE (DD-MM-YYYY) 27-03-2012	**2. REPORT TYPE** Master's Thesis	**3. DATES COVERED** (From – To) Sept 2012 – March 2014

4. TITLE AND SUBTITLE Integration, Testing, And Analysis Of Multispectral Imager On Small Unmanned Aerial System For Skin Detection	**5a. CONTRACT NUMBER**
	5b. GRANT NUMBER
	5c. PROGRAM ELEMENT NUMBER
6. AUTHOR(S) Sweetnich, Stephen R.	**5d. PROJECT NUMBER**
	5e. TASK NUMBER
	5f. WORK UNIT NUMBER

7. PERFORMING ORGANIZATION NAMES(S) AND ADDRESS(ES) Air Force Institute of Technology Graduate School of Engineering and Management (AFIT/EN) 2950 Hobson Way, Building 640 WPAFB OH 45433-8865	**8. PERFORMING ORGANIZATION REPORT NUMBER** AFIT-ENV-14-M-70

9. SPONSORING/MONITORING AGENCY NAME(S) AND ADDRESS(ES) Electrical and Computer Engineering Dept (ENG) Air Force Institute of Technology Graduate School of Engineering and Management (AFIT/EN) 2950 Hobson Way, Building 640 Clark, Jeffrey D Lt Col USAF AFIT/ENG jeffrey.clark@afit.edu	**10. SPONSOR/MONITOR'S ACRONYM(S)** AFIT/ENG
	11. SPONSOR/MONITOR'S REPORT NUMBER(S)

12. DISTRIBUTION/AVAILABILITY STATEMENT
DISTRIBUTION STATEMENT A: APPROVED FOR PUBLIC RELEASE; DISTRIBUTION UNLIMITED.

13. SUPPLEMENTARY NOTES
This material is declared a work of the U.S. Government and is not subject to copyright protection in the United States.

14. ABSTRACT
Small Unmanned Aerial Systems (SUAS) have been utilized by the military, geological researchers, and first responders, to provide information about the environment in real time. Hyperspectral Imagery (HSI) provides high resolution data in the spatial and spectral dimension; all objects, including skin have unique spectral signatures. However, little research has been done to integrate HSI into SUAS due to their cost and form factor. Multispectral Imagery (MSI) has proven capable of dismount detection with several distinct wavelengths. This research proposes a spectral imaging system that can detect dismounts on SUAS. Also, factors that pertain to accurate dismount detection with an SUAS are explored. Dismount skin detection from an aerial platform also has an inherent difficulty compared to ground-based platforms. Computer vision registration, stereo camera calibration, and geolocation from autopilot telemetry are utilized to design a dismount detection platform with the Systems Engineering methodology. An average 5.112% difference in ROC AUC values that compared a line scan spectral imager to the prototype area scan imager was recorded. Results indicated that an SUAS-based Spectral Imagers are capable tools in dismount detection protocols. Deficiencies associated with the test expedient prototype are discussed and recommendations for further improvements are provided.

15. SUBJECT TERMS
   small unmanned aerial systems, uav, hyperspectral, multispectral, skin detection, image quality

16. SECURITY CLASSIFICATION OF:			**17. LIMITATION OF ABSTRACT**	**18. NUMBER OF PAGES**	**19a. NAME OF RESPONSIBLE PERSON** Dr. David R. Jacques, AFIT/ENV
a. REPORT U	**b. ABSTRACT** U	**c. THIS PAGE** U	UU	140	**19b. TELEPHONE NUMBER** (Include area code) (937) 255-3355, ext 3329, david.jacques@afit.edu